

CHEMICAL EFFECTS IN X-RAY EMISSION SPECTRA  
OF TRANSITION METAL COMPOUNDS

by

Barbara Paci Mazzilli

A thesis submitted to the University of London  
for the Degree of Doctor of Philosophy

Department of Chemistry  
Queen Mary College



May 1982

COMISSÃO NACIONAL DE ENERGIA NUCLEAR/SP - IPEN

To my husband Carlos Eduardo  
and my beloved parents

## ABSTRACT

The present thesis is mainly concerned with the X-ray emission spectra of vanadium, titanium and chromium compounds. The high and the low-energy satellite lines associated with the  $K\beta_{1,3}$  emission band are investigated. Variations in the energy, shape and intensity of such non-diagram lines with the oxidation state of the X-ray emitting atom are presented and discussed.

An especial attention is also focussed in the determination of the  $K\beta/K\alpha$  intensity ratio. Although  $K\beta$  and  $K\alpha$  lines are associated with transitions between inner core electrons, the influence of the chemical form of the X-ray emitting atom and the type of ligand present in the molecule upon the final ratio is investigated.

The techniques X-ray emission and X-ray photoelectron spectroscopies are combined to give a complete picture of the molecular orbitals formed by the chemical association of atoms in the compound. The most common structures which use d valence orbitals for forming molecular orbitals are tetrahedral and octahedral. Both configurations are discussed in some detail, and the spectra concerning each individual compound are examined separately.

## ACKNOWLEDGEMENTS

The author would like to thank her supervisor, Dr. D.S.Urch, for the encouragement and guidance received during the course of the research. She is particularly grateful to him for his careful review of the thesis manuscript.

She feels also indebted to the whole post-graduate community of the Chemistry Department at Queen Mary College, especially to Mr. P.M.Montague, for his valuable help in the various stages of the experimental work.

Finally, thanks are also due to the following Brazilian sponsors, which made feasible this undertaking :

- IPEN (Instituto de Pesquisas Energéticas e Nucleares, São Paulo);
- CNEN (Comissão Nacional de Energia Nuclear, Rio de Janeiro).

## TABLE OF CONTENTS

	Page
CHAPTER I - INTRODUCTION	9
I.1 Purposes of the Present Research	9
I.2 Historical Survey	10
I.2.1 Discovery of X-rays and Early Works	10
I.2.2 Development of Quantum Theory	12
I.2.3 Effects of Chemical Combination in X-ray Spectra	15
I.3 Theoretical Aspects of X-ray Emission Spectroscopy	16
I.3.1 Basic Theory	16
I.3.2 Selection Rules and Diagram Lines	19
I.4 Theoretical Aspects of X-ray Photoelectron Spectroscopy	23
I.4.1 Introduction	23
I.4.2 Valence and Core-electron Levels in Solids and Gases	24
I.4.2.1 Spin-orbit Coupling in Open Shell Systems	27
I.4.2.2 Electron Shake-up and Shake-off Processes	29
I.5 Auger Transitions	32
CHAPTER II - EXPERIMENTAL ASPECTS	34
II.1 Practical Aspects of X-ray Stimulated Emission Spectroscopy	34
II.1.1 Instrumentation	34
II.1.1.1 Sample Preparation	40
II.1.1.2 Collimators	40
II.1.1.3 Crystal Choice	41
II.1.1.4 Detectors	42

	Page
II.1.1.4.1 Gas-flow Proportional Detector	43
II.1.1.4.2 Scintillation Detector	46
II.1.1.5 Pulse Height Analysis	48
II.1.2 Experimental Procedure	49
II.2 Practical Aspects of X-ray Photoelectron Spectroscopy	51
II.3 Spectrometer Broadening. Determination of the True Line Profile	57
II.3.1 Introduction	57
II.3.2 Spectrometer Broadening Effects	59
II.3.2.1 $m_h$ , $m_v$ and $m_r$	60
II.3.3 Application of the Iterative Deconvolution Method	67
II.3.3.1 Data Smoothing by a Simplified Least-squares Procedure	71
II.3.3.2 Limitations of the Iterative Method	75
II.3.3.3 Determination of the Machine Broadening Function $m(\theta' - \theta)$	77
 CHAPTER III - THE $K\beta$ SPECTRUM OF FIRST-ROW TRANSITION METAL COMPOUNDS	 85
III.1 Introduction	85
III.2 The $K\beta_{1,3}$ Peak	88
III.2.1 Shifts in the $K\beta_{1,3}$ Main Peak Energies	88
III.2.1.1 Chromium Compounds	90
III.2.1.2 Vanadium and Titanium Compounds	95
III.2.2 Origin and Intensity of the Low-energy Satellite Peak $K\beta'$	99
III.2.2.1 Emission Line Intensities	107

	Page
III.2.3 Shifts in the $K\beta_{1,3} + K\beta'$ Emission Spectrum Energies	111
III.3 High-energy Satellite Lines : the $K\beta_{2,5}$ Region	113
III.3.1 Introduction and Experimental Results	113
III.3.2 Changes in the $K\beta_{2,5}$ and $K\beta''$ Relative Intensities	119
III.3.3 Energy Separation between $K\beta_{2,5}$ and $K\beta''$	120
III.3.4 $K\beta_{2,5}$ Energy Shifts	123
 CHAPTER IV - CHEMICAL EFFECTS IN $K\beta/K\alpha$ X-RAY EMISSION INTENSITIES	 125
IV.1 Introduction	125
IV.2 Theoretical Calculations of X-ray Emission Rates in the Filling of Vacancies in the K Shell	130
IV.3 Experimental Data on the Relative Intensities of X-ray Lines	130
IV.4 Experimental Results and Discussion	137
 CHAPTER V - MOLECULAR ORBITAL INTERPRETATION OF X-RAY EMISSION SPECTRA INVOLVING VALENCE BAND ELECTRONS	 147
V.1 Introduction	147
V.2 Molecular Orbital Theory Applied to the Interpretation of Soft X-ray Spectra	148
V.2.1 Alignment of the X-ray Emission and X-ray Photoelectron Spectra	151
V.3 Bonding in Chromium Compounds	153
V.3.1 The Chromate Ion	153
V.3.1.1 Experimental Results	159

	Page
V.3.2 The Dichromate Ion and the Chromium (VI) Oxide	172
V.3.3 The Chromium (III) Oxide	177
V.3.3.1 Experimental Results	180
V.4 Bonding in Titanium and Vanadium Compounds	186
V.4.1 Titanium Carbide	186
V.4.2 Titanium Oxides ( $TiO_2$ and $Ti_2O_3$ )	189
V.4.3 Metatitanates and Orthotitanates	197
V.4.4 Titanium Fluoride	201
V.4.5 Vanadium Oxyanions	204
V.4.6 Vanadium Fluoride	209
V.5 Influence of the Auger Transition in the Soft X-ray Spectra. Suggestions for Further Work	211
 APPENDIX - A FORTRAN PROGRAM FOR ITERATIVE DECONVOLUTION	 215
 BIBLIOGRAPHY	 218



CHAPTER IINTRODUCTION1.1 Purposes of the Present Research

The main purpose of the present research is to study the "chemical effects" in the X-ray emission spectra of some transition elements in different compounds. By "chemical effect" we mean the influence exerted by the valence band electrons on the X-ray emission spectrum of the molecule under consideration. These "chemical effects" can be observed not only in the spectral lines directly involved with valence electrons, but also in spectral lines which originate in inner-shell electron transitions.

The elements investigated were first-row transition metals, where the d orbital is partially filled, e.g. titanium, vanadium and chromium. In nature these elements are found in compounds with widely varied oxidation states. Consequently, they should provide excellent examples for studying the so called "chemical effects" observed in emission spectra.

It is well known that a formal change in valence of a transition metal gives rise to variations in the radial functions of its atomic orbitals. We shall investigate if these variations result in intensity differences in the emission lines  $K\alpha$  and  $K\beta$ . For this purpose we shall study the  $K\beta/K\alpha$  intensity ratio in terms of the valence state of the emitting atom. Changes in  $K\alpha$  and  $K\beta$  peak energies and shapes will also be analysed.

## I.2 Historical Survey

### I.2.1 Discovery of X-rays and Early Works

It was in the course of a systematic attempt to see if any radiation could be produced which would traverse matter opaque to ordinary light that Roentgen discovered X-rays in 1895. The X-rays were so named by him due to their unknown nature. Besides producing fluorescence in certain salts, these rays were found to affect a photographic plate and to ionize gases, so that three methods, namely the visual, the photographic and the electrical, could be employed in their examination. Roentgen (1898) classified his tubes as "hard" and "soft", terminology applied to X-rays today. The hard tubes had a lower gas pressure than the soft. The potential difference required to generate X-rays in the hard tube was higher and these X-rays were stronger in penetrating power.

It was soon recognized that the properties of X-rays could be explained if the X-rays were assumed to be electromagnetic waves of wavelength much smaller than that of light. Many attempts were therefore made to investigate the diffraction of X-rays by passing them through a narrow slit (Haga & Wind, 1899; Sommerfeld, 1900; Walter & Pohl, 1909). Sommerfeld (1912) calculated the effective wavelength of hard X-rays, finding  $4 \times 10^{-9}$  cm; the wavelength of soft X-rays was seen to be measurably greater.

The X-ray diffraction technique began with the classic experiment of Friedrich et al (1912), in which the remarkable fact that crystals act as suitable gratings for diffracting X-rays was discovered. From this discovery has

grown, on the one hand, a surprisingly exact knowledge of the structure of many crystals and, on the other hand, a means of studying X-ray spectra which was comparable in precision with other methods of optical spectral analysis.

The first measurements, which indicated a relationship between X-ray emission and the atomic number of the emitting atom, were performed by Barkla (1911), who demonstrated that different "hardnesses" of radiation were emitted, depending upon excitation and target characteristics. It was in fact Barkla who proposed the line series nomenclature K, L, M, etc, still in use today. But the researcher to whom much credit must go for the confirmation of the relationship between wavelength and atomic number is Moseley (1914). He showed that the characteristic wavelength  $\lambda$  for each element in the periodic table is related to the atomic number  $Z$  by :

$$\frac{1}{\lambda} = K(Z - \sigma)^2 \quad , \quad (I.1)$$

where  $K$  is a constant depending upon the spectral series and  $\sigma$  is the shielding constant.

Bragg (1912) suggested a simple interpretation of the diffraction as arising from "reflection" of the incident X-ray beam from the planes within the crystal. He verified this interpretation by reflecting X-rays from the cleavage planes of mica sheets. Bragg's equation for X-ray diffraction is :

$$n\lambda = 2d \sin \theta \quad , \quad (I.2)$$

where  $n$  is an integer,  $\theta$  is the angle of incidence of the X-ray beam with respect to the crystal plane, and  $d$  is the distance between adjacent members of the set of diffracting planes. Within Bragg's equation lies the basis for the two major branches of X-ray analysis, namely X-ray diffraction (the study of crystal structures using radiation of known wavelength) and X-ray spectroscopy (the analysis of X-ray wavelength using a crystal of known dimensions).

### 1.2.2 Development of Quantum Theory

During the period referred to above, quantum theory was also conceived. Planck (1900) was able to announce the mathematical form of the law which governs the energy distribution. He discarded the precept that energy was to be assumed as strictly continuous and suggested that an oscillator could acquire energy only in discrete units called quanta. Planck introduced the postulate that the magnitude of the quantum of energy  $E$  is not fixed, but depends on the frequency  $\nu$  of the oscillator :

$$E = h\nu \quad , \quad (I.3)$$

where  $h$ , Planck's constant, has the dimension of energy times time.

Einstein (1905) extended Planck's concept of quantized radiation. Einstein brought back the concept of a corpuscular unit of radiation, or photon, as it is now called, in his effort to account for the photoelectric effect. According to him, the maximum kinetic energy of the

photoelectrons observed when light falls on a metal plate (photoelectric effect) is not dependent on the intensity of the light as it would be expected from classic electromagnetic theory, but only on the frequency. Einstein's equation

$$h\nu - B = \frac{mv^2}{2} \quad (I.4)$$

is an expression of the energy conservation for the energy conversion of one photon ( $h\nu$ ) into the kinetic energy, ( $mv^2/2$ ) of one photoelectron. The B constant represents the work required to remove the electron from the metal.

In order to understand the meaning of the remarkable regularities observed in X-ray spectra, Bohr's theory (1913) of the origin of spectral lines must be considered at this point. Its essential feature is the assumption that the atom may exist in any of a series of discrete states and that no radiation is emitted while it is in a certain state. When the atom changes from one state to another of less energy, however, the lost energy is radiated in a single unit, or quantum. If  $W_i$  is the energy of the atom in the initial state, and  $W_f$  in its final state, Bohr assumes that the frequency of the emitted radiation is given by the relation :

$$h\nu = W_i - W_f \quad (I.5)$$

The similarity between this expression and Einstein's photoelectric equation (I.4) is at once evident. The normal state of the atom is the state of least possible energy. In

this condition the atom cannot radiate, but may absorb radiation with a resulting change to an excited state of higher energy.

De Broglie (1924) was able to show that the dynamics of any particle might be expressed in terms of the propagation of a group of waves. That is, the particle might be replaced by a mathematically equivalent train of waves, as far as their motion is concerned. The motion of a particle in a straight line is represented by a plane wave. The wavelength is determined by the momentum of the particle. Thus, just as the momentum of a photon is :

$$\frac{h\nu}{c} = \frac{h}{\lambda} \quad , \quad (I.6)$$

so the wavelength of a moving electron is given by :

$$\lambda = \frac{h}{mv} \quad . \quad (I.7)$$

A fundamental belief of classical mechanics was that it is possible to measure simultaneously the position and the momentum of any body. However, in wave mechanics, based on the de Broglie equation, this concept was replaced by the famous uncertainty principle . This states that if the wavelength or frequency of an electron wave is to have a definite value, the wave must have an infinite extent. The uncertainty principle was first stated by Heisenberg in 1926 (Kauzmann, 1957) and can be expressed in terms of energy and time, as follows :

this condition the atom cannot radiate, but may absorb radiation with a resulting change to an excited state of higher energy.

De Broglie (1924) was able to show that the dynamics of any particle might be expressed in terms of the propagation of a group of waves. That is, the particle might be replaced by a mathematically equivalent train of waves, as far as their motion is concerned. The motion of a particle in a straight line is represented by a plane wave. The wavelength is determined by the momentum of the particle. Thus, just as the momentum of a photon is :

$$\frac{h\nu}{c} = \frac{h}{\lambda} \quad , \quad (I.6)$$

so the wavelength of a moving electron is given by :

$$\lambda = \frac{h}{mv} \quad . \quad (I.7)$$

A fundamental belief of classical mechanics was that it is possible to measure simultaneously the position and the momentum of any body. However, in wave mechanics, based on the de Broglie equation, this concept was replaced by the famous uncertainty principle . This states that if the wavelength or frequency of an electron wave is to have a definite value, the wave must have an infinite extent. The uncertainty principle was first stated by Heisenberg in 1926 (Kauzmann, 1957) and can be expressed in terms of energy and time, as follows :

$$\Delta E \Delta t \geq \frac{h}{2\pi} = \hbar \quad . \quad (I.8)$$

Schrodinger and Heisenberg independently discovered the basic principles for a new kind of mechanics, which provided mathematical techniques competent to deal with the wave-particle duality of energy and matter (Dirac, 1964).

### I.2.3 Effects of Chemical Combination in X-ray Spectra

The equipment used in the first experiments of X-ray emission spectroscopy did not allow the analysis of elements which were not in the solid state, under normal temperature and pressure conditions. Hence, when the element appeared in the liquid or in the gaseous phases, its analysis was done by means of one of its chemical compounds in the solid state. It was not believed, at that stage, that the ligands might have some influence in the spectral lines obtained.

The first evidence that the chemical state of the element under consideration did influence the X-ray absorption spectrum was obtained by Bergengren (1920). Lundquist (1930), on the other hand, was the first to observe analogous effects in X-ray emission spectra, when he investigated a series of sulphur  $K\beta$  spectral lines. Deodhar (1931) discovered new spectral lines, which were emitted just by some compounds of an element and not by all of them. He thus proved the existence of new energy levels in an atom, when it is linked to one or more different atoms. Skinner (1940) verified that the effect of the chemical combination was clearer when transitions originated in the valence band were investigated, that is, when soft X-rays



were analysed. As these lines are generally of low intensity, the samples were excited by electron bombardment. Such a way to excite the sample presented a series of inconveniences, the principal of these being the possible deterioration of the sample. Technological advances were essential for the development of X-ray spectroscopy as a powerful means for the explanation of the electronic structure of metals and related compounds.

White et al (1967) surveyed the data up to 1967 referring to the dependence between the binding energy of an electron and the chemical state of the emitting atom.

### I.3 Theoretical Aspects of X-ray Emission Spectroscopy

#### I.3.1 Basic Theory

When radiation of short wavelength interacts with matter, it can cause electrons to be ejected (from the occupied orbitals). The high-energy electromagnetic radiation normally consists of  $\gamma$ -rays or X-rays.

X-rays are electromagnetic radiation in the wavelength range  $500 \text{ \AA}$  to  $1 \text{ \AA}$ . An X-ray tube is operated by accelerating electrons to high energy and then allowing them to strike a metallic target. Inside the target, the interaction between the incident electrons and the atoms can occur in two distinct ways. Firstly, the electrons may be strongly affected by the fields of the atomic nuclei, so that they are then deflected, giving rise to the continuous radiation (or bremsstrahlung radiation). Secondly, the electrons can cause the ejection of a bound electron,

leaving a hole in the target atom. Then an electron of an outer shell can fall into this vacancy and a quantum of radiation will be emitted. As a consequence of these two processes, the X-ray spectrum of the target material will be formed by the characteristic of the target atom superimposed on the continuous emission.

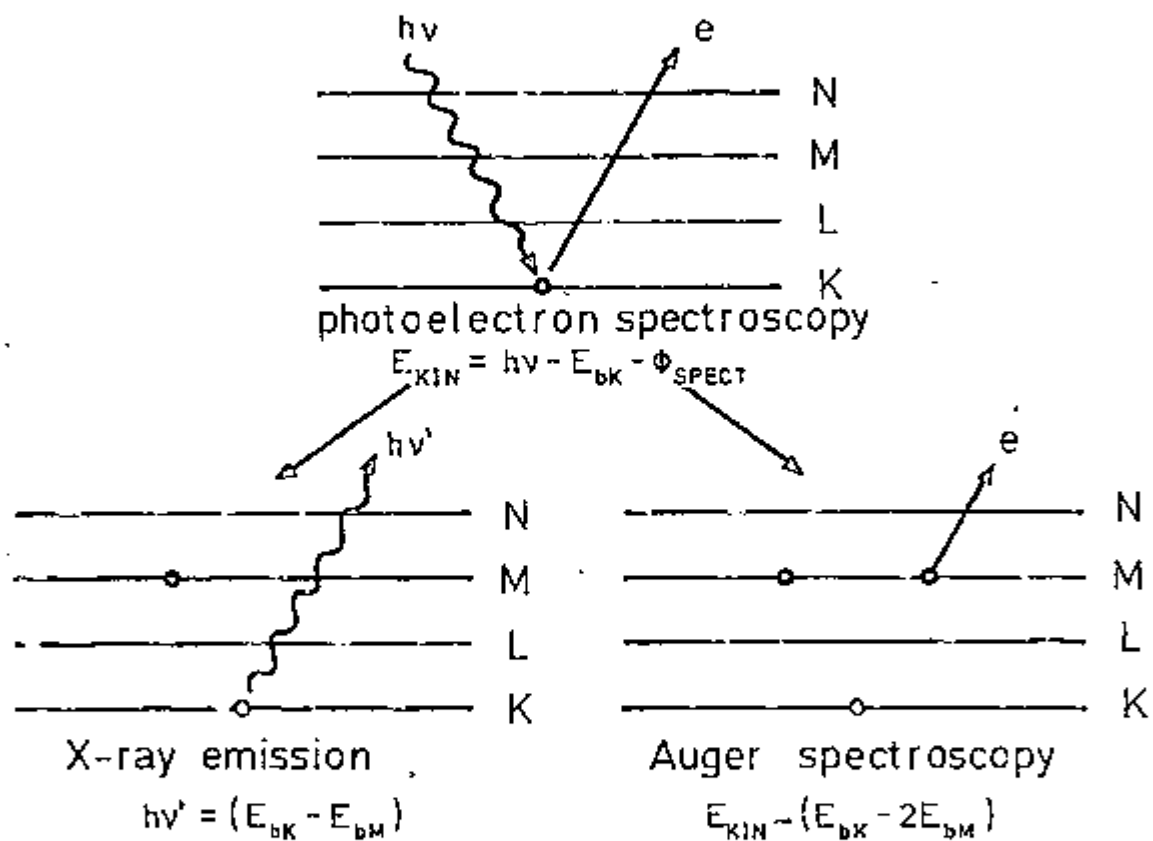


Figure I.1

#### Basic excitation and de-excitation processes

The process of displacement of one electron from its original state is called excitation. Figure I.1 illustrates the ejection of an electron from the K level by an incident photon of energy  $h\nu$ . The kinetic energy of the ejected electron will be equal to  $h\nu - E_{bK} - \phi_{spect}$ , where  $E_{bK}$  is the binding energy of the electron in the K shell and  $\phi_{spect}$  is

the spectrometer work function. The atom is then said to be in the excited state  $K^+$ . The study of these ejected photoelectrons, whose quantity and energy are characteristic of the individual molecular orbital from which they originate, is called photoelectron spectroscopy. This topic will be discussed in more detail in section I.4. The excited ion can relax through various processes, two of which are predominant. Figure I.1 illustrates the basic processes of X-ray emission and Auger spectroscopy.

According to the X-ray emission process, an outer shell electron fills in the existent vacancy, with consequent X-ray emission. Here, the electronic relaxation process is always accompanied by radiation emission whose energy is equal to the difference between the binding energies of the shells involved, which is  $(E_{bK} - E_{bM})$  in the example given.

The second process is quite similar to the first one in its initial stage, although the radiation produced by an electronic transition from an outer shell is not emitted, but can be regarded as being used for a new ionization within the atom. Such a process, illustrated in Figure I.1, is known as Auger process. In this case, the electron will have an energy approximately equal to the relaxation energy,  $E_{bK} - E_{bM}$  (in the given example), less the energy required for the ejection of this electron, i.e. the binding energy of the ejected electron in the presence of a hole in the M level. The Auger process leads to the formation of two or more vacancies in the outer shells. This double vacancy could eventually be responsible for the formation of satellite lines.

### I.3.2 Selection Rules and Diagram Lines

The nomenclature most commonly used to describe the various X-ray lines depends upon the primary vacancy. Thus, K spectra result from the relaxation of an atom with a vacancy in an orbital with principal quantum number 1, L spectra refers to principal quantum number 2, and so on.

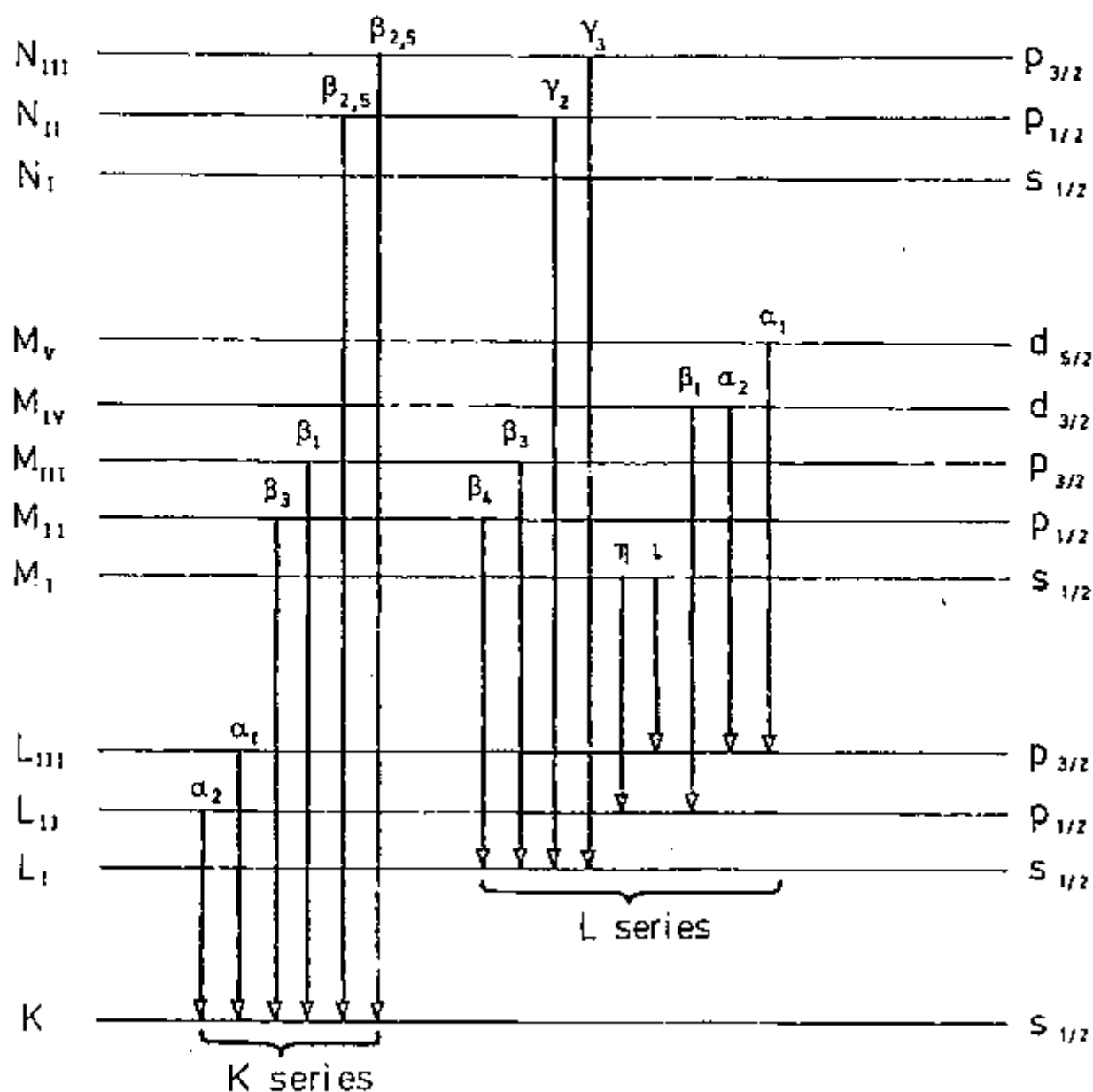


Figure I.2

Principal X-ray emission processes for the lighter elements

An inner vacancy can of course be filled in by transitions from a variety of less tightly bound orbitals. These are denoted by Greek letters further differentiated by Arabic numerals. Thus, a  $2p \rightarrow 1s$  transition could give rise to two possible X-rays of similar energy, depending upon the final electronic state of the ion  $P_{1/2}$  or  $P_{3/2}$ . These two X-rays are  $K\alpha_1$  and  $K\alpha_2$ . When the two peaks are not resolved, the subscripts are written together. The symbols used for the principal X-ray emission lines are summarized in Figure I.2.

Another description of the ions in use is based on the orbital notation. The principal quantum number ( $n$ ) and the orbital angular momentum ( $l$ ) of the ejected electron are used to describe the electronic transition, together with the spin-orbit coupling which splits the energy of each ionic state. The transition  $K\alpha_{1,2}$ , for instance, will be described in this notation by  $1s \rightarrow 2p_{3/2}$  and  $1s \rightarrow 2p_{1/2}$ .

The intensity of a given spectral line is determined by the transition probability, that is, the probability that the system will change from an initial state to another one.

In several problems, particularly those dealing with emission and absorption of radiation, it is necessary to estimate the effects produced by a perturbation which is a function of the time. The rate of photoemission is described in terms of a perturbing Hamiltonian operator  $H'$ , such that  $T$ , the transition probability matrix, is given by (Eyring et al, 1967) :

$$T = \int \psi_i^* H' \psi_i dt \quad , \quad (I.9)$$

where  $\Psi_f$  is the wave function of the final state;  $\Psi_i$  is the wave function of the initial state and  $H'$  is defined by :

$$H = H_0 + H' \quad , \quad (I.10)$$

where  $H_0$  is the Hamiltonian for the system in absence of perturbation and  $H$  is the Hamiltonian for the perturbed system.

The wave functions for an atom can all be classified as being even or odd . An even wave function is defined as one such that  $\Psi(x,y,z)$  is equal to  $\Psi(-x,-y,-z)$ , that is, the wave function is unchanged on changing the signs of all the positional coordinates of the electrons. An odd wave function is defined as one such that  $\Psi(x,y,z)$  is equal to  $-\Psi(-x,-y,-z)$ .

It is verified that the only transitions accompanied by the emission or absorption of dipole radiation which can occur are those between an even and an odd state (an even state being one represented by an even wave function). Consequently, the integral of equation (I.9) will vanish in case both  $\Psi_f$  and  $\Psi_i$  are either even or odd, but it is not required to vanish in the case that one is even and the other odd.

The above discussion leads to the very important selection rule that transitions with emission or absorption of dipole radiation are only allowed between even and odd states. The one-electron wave functions are even for  $l = 0, 2, 4, \text{etc}$  (s, d, g, etc orbitals) and odd for  $l = 1, 3, 5, \text{etc}$  (p, f, h, etc orbitals). The electric-

dipole selection rules can then be expressed as :

$$\Delta n \geq 1 \quad ; \quad (I.11)$$

$$\Delta l = \pm 1 \quad ; \quad (I.12)$$

$$\Delta j = \pm 1, 0 \quad ; \quad (I.13)$$

$$\Delta s = 0 \quad . \quad (I.14)$$

This means, for instance, that a vacancy in a p orbital can only be filled by transitions from s and d orbitals.

The observed characteristic X-ray emission lines which obey these selection rules are called diagram lines. All the others are named satellites. Satellite lines are therefore defined as peaks whose origin cannot be explained as a straightforward consequence of the various energy levels of the neutral atom or molecule. These satellite lines can have higher or lower energies than the main peak but they are rarely very intense. Some satellite lines result from quadrupole transitions in accordance with the selection rules :

$$\Delta l = 0 \text{ or } \pm 2 \quad ; \quad (I.15)$$

$$\Delta j = 0, \pm 1 \text{ or } \pm 2 \quad . \quad (I.16)$$

It can be demonstrated that the dipole transitions are by far the strongest. In fact, they are  $10^2$  times more intense than the next strongest lines, due to the quadrupole transitions.

The single ionized states formed before and after the emission of a photon have a transient existence. The

probability of an electronic transition is given by the Einstein equation, which shows a dependence upon frequency. A relaxation process which involves the emission of a highly energetic quantum will proceed more rapidly than the emission of a less energetic quantum. Typical lifetimes are of the order of  $10^{-17} - 10^{-14}$  seconds (Sevier, 1972). The ion which results after X-ray emission will also have a characteristic lifetime, but this will be relatively longer, since lower energy processes are involved in its decay. The consideration of lifetimes is of importance because of the relationship between the uncertainty in the energy of the emitted X-ray (natural line width) and the lifetime of the shortest excited state. The short lifetime  $\Delta t$  of an excited state limits the time available to determine the energy of this state. Therefore, there is an uncertainty in the energy described by the Heisenberg uncertainty principle :

$$\Delta E \Delta t = \hbar \sim 6.6 \times 10^{-16} \text{ eV sec} \quad , \quad (\text{I.17})$$

where  $\Delta E$  is the natural energy width of the level and  $\Delta t$  is the lifetime of the state. Such values are important as they give an indication of the resolution which can be experimentally achieved.

#### 1.4 Theoretical Aspects of X-ray Photoelectron Spectroscopy

##### 1.4.1 Introduction

The quantity measured in photoelectron spectroscopy is the kinetic energy required for the removal of electrons from different atomic and molecular orbitals. The



fundamental equation for the photoelectric process is based on the energy conservation principle :

$$h\nu = E_b + E_{kin} + \Phi_{spect} \quad (I.18)$$

According to the source of radiation, which has to be a flux of nearly monoenergetic radiation with mean energy  $h\nu$ , photoelectron spectroscopy can be divided into two main areas : ultraviolet photoelectron spectroscopy (UPS) and X-ray photoelectron spectroscopy (usually known as XPS or ESCA). In the former case the incident radiation is provided by photons from rare gas resonance radiation, e.g. He I 21.2 eV, He II 40.8 eV. This energy is only sufficient to ionize valence band electrons of the molecule, which are involved in the chemical bonding. The latter technique, which normally utilizes Mg and Al X-ray tubes is more appropriate when we intend to study both the valence and the core electrons at the same time. The most intense line emanating from such tubes is the unresolved  $K\alpha_{1,2}$  doublet, resulting from the  $2p_{1/2,3/2} \longrightarrow 1s$  transition in the metallic anode. For Mg and Al these X-rays have 1253.6 eV and 1486.6 eV, respectively.

#### I.4.2 Valence and Core-electron Levels in Solids and Gases

Normally, when the element to be analyzed is an isolated atom (like a monoatomic rare gas), the photoelectron ejection will give rise to peaks which are due to specific states of single-ionized ions :  $1s$  ,  $2s$  , etc. In some cases, the existence of different energy levels in a final ionic species is verified. These levels are due to

electronic interactions within the species itself, like the spin-orbit coupling.

Spin-orbit splitting is a process that arises from a coupling of the spin and orbital angular momenta. For orbitals with  $\ell > 0$ , there are a number  $(2\ell + 1)$  of equivalent ways in which the orbitals may be oriented in space. In the absence of an electric or magnetic field, these orientations are degenerate. Ionization, however, will cause the formation of a hole in an inner shell, giving rise to a splitting of the degenerate levels. Thus, for an especial case of one hole in an otherwise closed shell, a new quantum number ( $j$ ) can be defined :

$$j = \ell \pm \frac{1}{2} \quad . \quad (I.19)$$

No spin-orbit splitting occurs for s subshells, for which  $j = \pm 1/2$ , since the energy is proportional to the absolute magnitude of  $j$ . The relative intensities of the photoelectron lines are given by  $2\ell$  and  $2\ell + 2$ .

If we start dealing with molecules instead of monoatomic gases, we realize that the valence electrons are in principle very different from free atoms, whereas the core electrons are almost the same. The valence band electrons will be strongly affected by the ligand atoms due to the formation of molecular orbitals. The photoelectron spectra of core electrons, on the other hand, will merely undergo a displacement in energy, giving rise to the phenomenon known as "chemical shift". That "chemical shifts" were actually due to shifts of core levels, rather than

changes in the reference level, came from experiments on substances containing one type of atom in different positions (Hagström et al, 1964). Three possible effects are responsible for these "chemical shifts": changes in valence, ligand and lattice configuration. The charge of the valence shell is by far the most important of them. In fact, the basic physics of core-level binding energy shifts can be understood in terms of shielding of the core electrons by electrons in the valence shell. When the charge in the valence shell changes, this shielding will also change. We can consider a model of a free ion as being core electrons inside a spherical charge shell of valence electrons with radius  $R$ . The potential inside the sphere is :

$$V_Q = \frac{Q}{R} \quad , \quad (I.20)$$

where :  $Q$  = electric charge;

$R$  = atomic radius;

$V_Q$  = potential energy of a core electron, due to the valence shell.

The binding energy shift can thus be written :

$$\Delta(\text{B.E.}) \sim -\Delta V_Q \sim -\frac{\Delta Q}{R} \quad , \quad (I.21)$$

where  $\Delta(\text{B.E.})$  = binding energy shift.

If the charge  $Q$  has been removed, all core-electron binding energies will be increased by this amount. The binding energies will decrease by  $Q/R$ , if the charge  $Q$  has been

added.

There are other effects which are also observed in XPS spectra of chemical compounds, namely :

- spin-orbit coupling in open shell systems;
- electron shake-up and shake-off processes;
- multiple excitation due to configuration interaction.

#### 1.4.2.1 Spin-orbit Coupling in Open Shell Systems

There are many compounds with unpaired electrons which present a component of spin or orbital angular momentum, even before the ionization. That is the case, for instance, of the transition metal compounds, which possess the d orbital not completely filled, and of the rare earths and actinides with their unfilled f orbitals. In these cases, the problem of multiplet splitting will be far more complex, as the coupling between the electrons of the valence band with unpaired spins and the hole arising from the ionization will lead to the formation of more than one final state.

The first photoelectron spectra obtained for transition metal compounds were taken by Fadley et al (1969, 1970), who measured splittings of core-electron binding energy for Mn and Fe compounds. To understand the origin of these splittings we have to consider the  $Mn^{2+}$  ion configuration  $[(core) 3s^2 3p^6 3d^5]$  whose ground state is  ${}^6S$ . If we remove one electron from the 3s shell, the ion will be left with an additional unpaired electron, which leads to the formation of two possible final states :  $[(core) 3s^1(\uparrow) 3p^6 3d^5]$  and  $[(core) 3s^1(\downarrow) 3p^6 3d^5]$ . In one of these two final states,  ${}^7S$ , the 3s electron can be considered as having its spin

parallel to those of the five 3d electrons, whereas in the other one,  $^5S$ , the 3s and 3d electrons will present antiparallel spins. Because the exchange interaction acts only between electrons with parallel spins, the  $^7S$  energy will be lowered relative to the  $^5S$  energy (Slater, 1960). Experimental results indicated a core-electron binding-energy splitting of  $\sim 6.5$  eV for the 3s level of Mn in  $MnF_2$  and MnO (Fadley et al, 1969, 1970).

Freeman et al (1970) have extended this study by performing theoretical calculations of the multiplet structure of the core-electron binding-energy splittings. They obtained 11.3 eV for the isolated  $Mn^{2+}$  ion and 6.8 eV for the  $MnF_6^{4-}$  cluster. This calculation, as well as those for  $NiF_6^{4-}$  (Ellis et al, 1968; Moskowitz et al, 1973) led to higher splittings than the experimentally observed values. This can be partially explained because in a molecular bond the unpaired electrons in the valence shell will be influenced by the covalent bonding effects, decreasing the overlap between the core and valence electrons. The large reduction in value for the 3s-3d exchange splitting in going from free ion to a complex can also be explained by the decrease of the exchange integral between the 3s and 3d orbitals, caused by an increase in the 3d shell radius, due to the cluster formation (Carver et al, 1972).

So far, we have been discussing the multiplet splittings which occur in the 3s-shell. If we now consider the 3p region of the spectrum, we realize that the resulting splitting is not so simple as that observed in the 3s region (Briggs et al, 1974; Nefedov, 1966; Tsutsumi et al, 1968).

The effects will be more complicated because of the possibility of coupling both spin and orbital angular momenta in the core-ionized state. The orbital angular momentum of the 3p electron permits several L-S couplings within the  $3p^5-3d^5$  configuration, giving rise to four possible final multiplet states. Free-ion calculations of 3p splittings for  $Mn^{2+}$  yield results in qualitative agreement with the experimental data for  $MnF_2$  (Fadley et al, 1969).

#### I.4.2.2 Electron Shake-up and Shake-off Processes

The other phenomenon leading to a multiplicity of final electronic states is concerned with multielectron excitation. Conclusions about the origin and relative intensities of these multielectron spectra can be based on the "sudden approximation". The fundamental assumption is that the primary photoabsorption process (which excites a core electron from an inner shell into a continuum photoelectron state) occurs so rapidly that the valence electrons do not have time to adjust to the change in the potential. The initial state and the electrons which will be left after the ionization can therefore be described by the same wavefunction, according to Koopmans's theorem (1933). This theorem states that the ionization potential of an electron is equal to the negative energy of the orbital from whence it comes :

$$I(\Psi_i) = - E(\Psi_i) \quad . \quad (I.22)$$

Koopmans's theorem can be applied in both X-ray photoelectron and X-ray emission spectroscopy experiments.

One of the limitations of the approximation is that it neglects the relaxation energy and treats the electronic orbitals as though they were unchanged or "frozen" during the ionization.

Several authors (Aarons et al, 1973; Coulthard, 1967; Hedin et al, 1969; etc) observed that the determination of the ionization energies of inner core electrons is more accurate if the relaxation energy involved in the process is taken into account. No improvement was found, on the other hand, for the outer core electrons. Generally speaking, the conclusions achieved by these authors show that the relaxation energy becomes more evident as the electrons are more tightly bound.

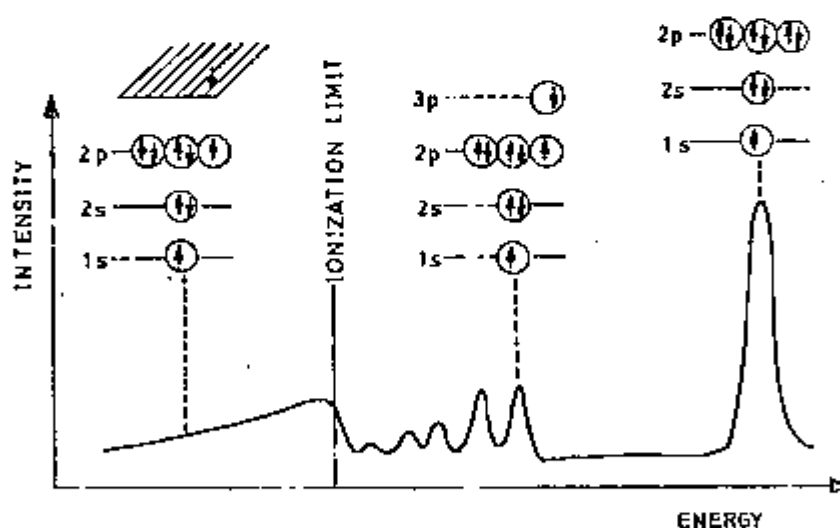


Figure I.3

Shake-up and shake-off structure in photoelectron spectrum of core shell of neon (from Carlson, 1975)

As a result of the ejection of a core electron, the Coulombic potential felt by the outer electrons will be altered. This "sudden" change may cause the excitation of a valence electron to a higher previously unoccupied orbital

(electron shake-up) or to the continuum (electron shake-off). Both processes can be regarded as taking place simultaneously with the photoelectron ejection. Figure 1.3 gives an illustration of a satellite structure arising in photoelectron spectra of core shell of neon. In this figure, the shape of the shake-off spectrum has been exaggerated for viewing purposes.

Studies of electron shake-up and electron shake-off following photoionization have been reported to appear in XPS of a large number of substances, from simple atoms (Carlson, 1967; Krause et al, 1968, 1972) to more complex molecules, as rare earth and uranium compounds (Jørgensen et al, 1972; Wertheim et al, 1972).

The energy balance for a two-electron transition in which double ionization occurs (shake-off event) can be understood in the same way as for the shake-up excitation. The energy of the final state will be reduced by :

$$E_1 + E_2 = h\nu - E_K - E_{np(K)} = \text{constant} \quad , \quad (\text{I.23})$$

where  $(E_1 + E_2)$  is the sum of the kinetic energies of the ejected electrons;  $h\nu$  is the photon energy;  $E_K$  is the binding energy of a K electron and  $E_{np(K)}$  is the ionization energy of a np electron in an atom with a hole in the K shell.

Usually, shake-up and shake-off satellites appear on the higher binding-energy side of the main peak. In first-row transition-metal compounds, these satellite peaks normally appear less than 10 eV away from the main peak.



Frost et al (1972) and Brisk et al (1975) obtained satellite peaks for  $\text{Cu}^{2+}$  and  $\text{Mn}^{2+}$  ions, respectively, whose intensity was almost the same as the corresponding main peak.

According to what we have been discussing, the characteristic electron energy-loss spectra of many compounds can be attributed to excitation of the electrons belonging to the valence band. In some cases, however, the Coulomb interaction between these electrons can result in a collective oscillation at a high frequency. When a charged particle excites such collective oscillations, the energy transfer will be related to all the electrons that are cooperatively moving, causing a collective loss of energy. The process is known as electronic plasmon oscillation and is extensively discussed by Pines (1956) and Best (1962).

### 1.5 Auger Transition

Meitner (1922) and Robinson (1923) found that atoms ionized in inner shells emit monoenergetic electrons, with energies which do not depend upon the manner in which the atoms are ionized. Later, in a classic series of experiments, Auger (1925, 1926) produced direct proof that atoms ionized in inner shells emit electrons whose transitions are not accompanied by emission of radiation. These electrons were later named "Auger electrons". Auger found that the production of these electrons was not dependent on the energy of the incident X-rays ( $h\nu$ ), in contrast with photoelectrons, whose energy was dependent upon  $h\nu$ . He also verified that the rate of production of

"Auger electrons" increased with the atomic number ( $Z$ ) of the target atom, despite the fact that the process did not always accompany the ejection of photoelectrons. We can consider, for instance, the transition in which the initial state has a hole in the K shell, and this vacancy is filled by an  $L_{II}$  electron with expulsion of an  $M_{III}$  electron. The notation used to describe an Auger process is obtained by the naming of the orbitals or shells in which vacancies occur, both in the initial and the final states. In the example given, the emitted electron is referred to as a  $KL_{II}M_{III}$  Auger electron. Energetically, this is equivalent to the production of an X-ray ( $2p \rightarrow 1s$  transition) which will in a second stage be responsible for the ejection of an electron from the  $M_{III}$  shell. The way an Auger transition occurs, however, it is rather a two-electron Coulombic readjustment to the initial hole. In this way, it is possible to explain several transitions which actually take place, although they are not always allowed in the dipole approximation.

The Auger transition has three important consequences in X-ray spectra :

- the Auger transition competes with the X-ray emission process in the de-excitation of an atom and therefore influences the width of the X-ray emission lines;
- the Auger transition changes the position of a vacancy from one shell to another, and therefore influences the intensity of the X-ray emission lines;
- the Auger transition can be one of the causes for the origin of the satellite lines in X-ray spectra, as it leaves the atom in a state of double ionization.

CHAPTER IIEXPERIMENTAL ASPECTS

All spectra presented in this research work were recorded using a Philips PW1410 flat single crystal X-ray emission spectrometer and a Vacuum Generator ESCA 3 photoelectron spectrometer. This chapter deals with the description of individual components of such equipment, as well as of the experimental procedure used for obtaining the spectra. Some aspects concerning the finite resolving power of the spectrometer and how to improve it are discussed, as well.

II.1 Practical Aspects of X-ray Stimulated Emission SpectroscopyII.1.1 Instrumentation

The instrumentation required to carry out X-ray spectroscopy measurements can be divided into three principal sections, namely stimulation, dispersion and detection of the characteristic X-rays. The primary source unit, responsible for the stimulation of the sample, can in principle be any high-energy particle e.g. electron, proton, ion or a high-energy photon, such as an X or  $\gamma$ -ray. Nowadays the majority of commercial X-ray spectrometers are fitted with primary X-ray source consisting of a sealed X-ray tube. The dispersion is normally achieved using a wavelength dispersive system, which is based on the

diffracting property of a large single crystal to disperse the polychromatic beam of excited radiation. Finally, we have the X-ray detector, whose function is to convert the energies of the X-ray photons into voltage pulses which can be counted, giving a measurement of the X-ray flux.

The layout of a conventional X-ray fluorescence spectrometer can be seen in Figure II.1. Air can be tolerated between the various parts of the spectrometer if hard X-rays ( $\lambda < 0.2 \text{ nm}$ ) are being studied, but for softer X-rays ( $0.2 \text{ nm} < \lambda$ ) vacuum is essential within the spectrometer. This vacuum is obtained by means of a single rotary pump and must be better than  $10^{-1}$  torr if X-rays softer than 2 keV are to be analysed.

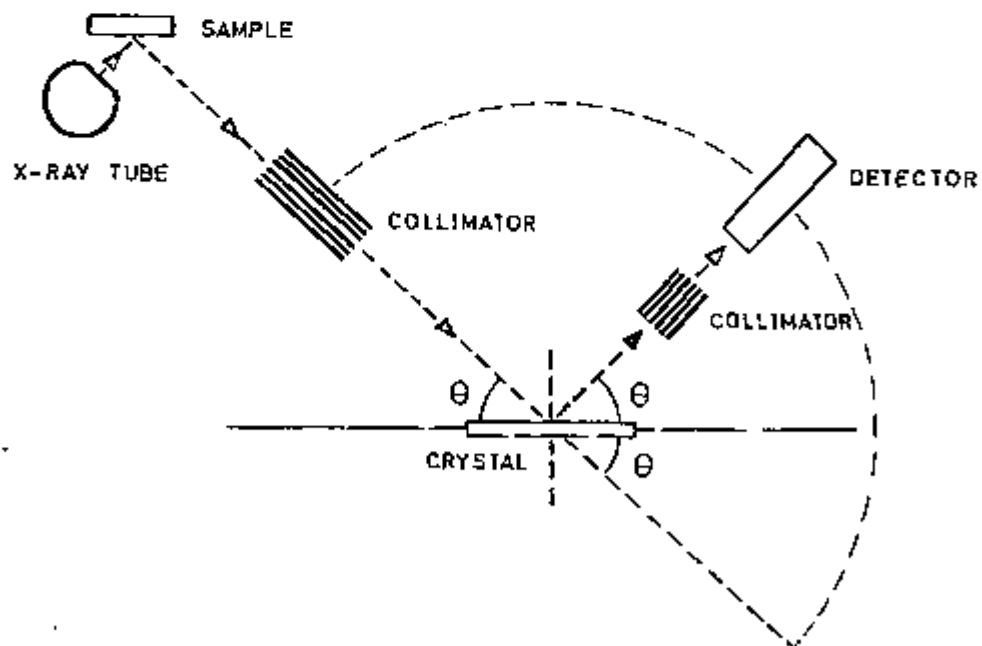


Figure II.1

Layout of a conventional X-ray fluorescence spectrometer

(a) X-ray tube

The exciting radiation is provided by the bremsstrahlung and characteristic X-ray lines of a chromium or copper sealed X-ray tube of maximum power 2.7 kW. In the X-ray tube a beam of electrons is accelerated on to a target made of a metal, and this target will emit its own X-rays and also a considerable amount of white radiation. This radiation leaves the tube via a thin beryllium window. These tubes are evacuated to  $10^{-5}$  torr. The power is supplied by a PW1130 d.c. X-ray generator which has the advantage that the current (maximum of 80 mA) and the voltage (maximum of 60 kV) can be independently varied. The efficiency by which a particular element can be stimulated to emit its own characteristic radiation varies with the irradiating frequency, so that a variety of X-ray tubes are necessary in order to ensure the optimum conditions for the detection of any particular element that may be present in the sample.

Difficulties may sometimes arise due to the similarity between emission frequencies of the X-ray tube and of the sample, when it is necessary to use a different excitation source. In chromium containing samples, for instance, undesirable interference was observed from the emission spectrum of the chromium metal from the X-ray tube. A copper X-ray tube was used instead to overcome this problem.

The sealed X-ray tube, however, is not suitable if we desire to study the soft X-ray lines (energy less than 1000eV), because of the absorption properties of the beryllium window. Figure II.2, which shows window transmission as a function of wavelength for different

thicknesses of X-ray tube windows, clearly illustrates this problem. From the curves shown, it is clear that it is quite difficult to obtain any excitation at all for long wavelength radiation.

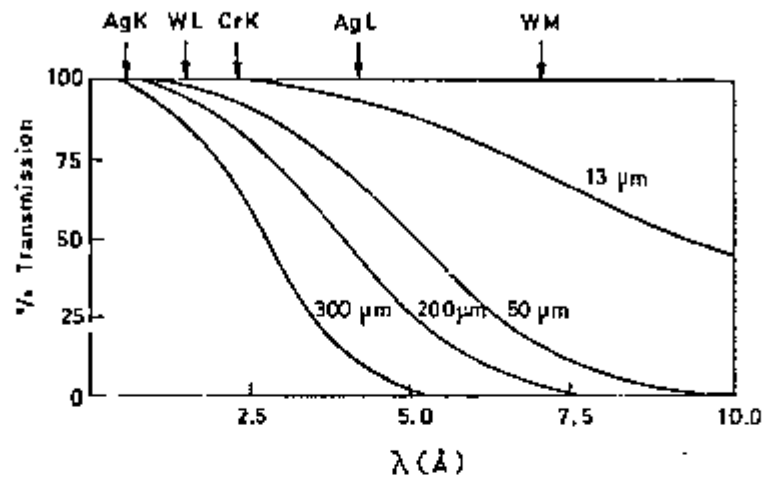


Figure II.2

Transmission characteristics of beryllium X-ray tube windows from Jenkins (1974)

In these cases, the traditional tube is replaced by a windowless CGR Elent 10 soft X-ray tube. The Elent 10 apparatus comprises a cold cathode windowless tube, an electrical supply unit and an internal-pressure stabilization device. The anode is composed of solid tungsten continuously water cooled. The cathode is composed of pure aluminium, the discharge being produced within a fused silica insulating tube provided with a hole through which the radiation passes. The back of the tube comprises the high voltage connection and the air inlet for pressure stabilization. The discharge takes place at a gas pressure of  $4 \times 10^{-2}$  torr and it is controlled by the air entrance at the back of the tube. This air leak is governed by an

especial valve system linked to the tube current, so that any change in the discharge causes a variation in the current which feeds back to alter the valve setting and restore the current to its original level. In this manner, the X-ray output should be greatly stabilized. Nevertheless, in practice, we did not manage to obtain a current as stable as we had wished. The generator supplies the discharge tube with a stabilized voltage. The normal operating voltage and current lie in the range of 4-7 kV and 3-6 mA, although the generator can work at a maximum power of 180 W.

#### (b) Spectrometer

The sample is placed as near as possible to the X-ray tube, so that to receive the maximum intensity. The radiation emitted by the sample is collimated before and after its dispersion by the analysing crystal. The primary collimator can be used in either a coarse or a fine mode, depending on the emission intensity of the desired spectrum. As we shall see later, a fine collimation implies in a better resolution on the final spectrum. The X-rays are then diffracted according to Bragg's equation :

$$n\lambda = 2d \sin \theta \quad , \quad (II.1)$$

where :  $n$  = order of diffraction (integer);

$\lambda$  = radiation wavelength;

$d$  = distance between two diffracting planes in the crystal;

$\theta$  = angle of incidence (see Figure II.1).

For the detection of the X-rays, the spectrometer is equipped with a gas-flow proportional counter and a thallium activated (1%) sodium iodide scintillation counter. The detectors rotate around the crystal axis at a rate that is twice the rotation of the crystal. In this way, a variation of  $d\theta$  in the angle of incidence of the X-ray is accompanied by a movement of  $2d\theta$  by the detectors so as to follow the reflected radiation. When we want to use the scintillation counter, it is not necessary, although it is possible, to remove the gas-flow proportional counter and its collimator. The efficiency of the scintillation counter, however, is severely reduced due to the absorption of X-rays in the front window (one micron) and in the back window (six microns) of the flow counter. The equipment geometry is such that the scintillation counter cannot be used for  $2\theta$  angles larger than  $120^\circ$ .

The gas-flow proportional counter is placed inside the vacuum chamber, so that it can be used to detect soft X-rays. On the other hand, the scintillation counter is outside the vacuum chamber and this restricts its use to X-rays with energies larger than 4.5 keV.

The pulses emitted from the detectors are amplified, subjected to pulse height analysis and displayed as an intensity measurement on a rate meter. When a spectrum is being scanned automatically, the rate meter reading can be used to operate a chart recorder, which then gives a permanent record of the spectrum. The spectrometer is also equipped with the facility to record automatically a spectrum by remaining stationary at a specific angle for a



fixed time, recording the count rate on a teleprinter and then moving on, by a small increment. This process ("step-scanning") continues until a complete emission band has been scanned.

#### II.1.1.1 Sample Preparation

The compounds to be analysed were finely powdered and then compressed into a disk shape, using terephthalic acid as a binding agent, for presentation to the spectrometer. The disks, with diameter of 3.6 cm and thickness between 2 and 5 mm, were prepared in a ring press. In some cases, however, as in the analysis of the oxygen K spectrum, the samples were pressed with polyethylene powder or into a copper mesh, to avoid interference of the oxygen present in the terephthalic acid. Most of the compounds studied in the present work were obtained from chemical supply companies. Some, as the chromium complexes, were prepared in the laboratory using straightforward techniques.

#### II.1.1.2 Collimators

The angular divergence of a collimator is given by :

$$\Delta\theta = 2 \text{ arc tan}(w/l) \quad , \quad (\text{II.2})$$

where  $w$  is the collimator blade separation and  $l$  is the collimator blade length.

The primary collimator, placed between the sample and the analysing crystal, has blade separation of 550  $\mu\text{m}$  (for the coarse collimation) and 150  $\mu\text{m}$  (for the fine

collimation). As its length is 12.2 cm we deduce that the angular divergence is  $0.52^\circ$  and  $0.14^\circ$ , respectively. The small collimator placed between the analysing crystal and the entrance to the proportional counter has a rather large angular divergence ( $w = 550 \mu\text{m}$  and  $l = 3 \text{ cm}$ ). Its main purpose is to reduce scattered background radiation, since few diverging X-rays are eliminated by this secondary collimation. However, the collimator placed in front of the scintillation counter has an angular divergence of  $0.17^\circ$  ( $w = 150 \mu\text{m}$  and  $l = 10 \text{ cm}$ ), which appreciably enhances the resolution. The increased path length of the X-rays in this case is another factor which contributes to a major reduction of the divergent beams.

### II.1.1.3 Crystal Choice

The selection and choice of analysing crystals depend on two basic properties : its angular dispersion and its reflecting power. The angular dispersion (D) may be defined as the variation of the incident angle in terms of the wavelength of the incident radiation :

$$D = \frac{d\theta}{d\lambda} = \frac{n}{2d \cos \theta} \quad (\text{II.3})$$

Hence, D tends to increase as the incident angle gets closer to  $90^\circ$ . In practice, the choice will fall, whenever possible, on the crystal which gives a larger value of  $\theta$ , for a certain wavelength. It is also apparent that, for different crystals, the dispersing power increases with the decreasing of  $2d$  spacing, and that the higher the order of

reflection ( $n$ ), the better the dispersion.

In practice, the maximum possible value of  $\theta$  is  $75^\circ$ , thus the maximum value which  $\sin \theta$  can take is around 0.95. Therefore, according to Bragg's law, a crystal of very large  $2d$  spacing would cover a wide range of wavelengths. Unfortunately, however, the angular dispersion of such a crystal for a shorter wavelength would be completely unacceptable because of its large  $2d$  spacing. A compromise has obviously to be achieved and, for this reason, a range of analysing crystals is nearly always employed to cover adequately the whole wavelength range.

The choice must of course lie on the basis of optimizing the resolving power ( $E/dE$ ), without a drastic loss of sensitivity. The resolving power can be derived by combining Bragg's equation (II.1) and equation (II.3) :

$$\frac{E}{dE} = - \frac{\lambda}{d\lambda} = - \frac{\tan \theta}{d\theta} \quad , \quad (\text{II.4})$$

where  $E$  (eV) =  $12398.1/\lambda$  ( $\text{\AA}$ ).

Therefore, although the dispersion of a given crystal improves with the increasing of  $n$ , in practice the best sensitivity is obtained by using a crystal of larger  $2d$  spacing and comparable dispersion at lower orders.

The angular dispersion of the crystal is not, however, the only factor affecting the shape of a line profile. Just as important are the divergences allowed by the primary and secondary collimators, as well as the orientation of the first layers of the analysing crystal. These factors will be

discussed in more detail in the section concerning the resolving power of the spectrometer.

#### II.1.1.4 Detectors

The purpose of the X-ray detector is basically that of converting the energy of the X-ray photons into pulses which can be counted, thus determining the X-ray flow. Two types of detectors are commonly employed : the gas-flow proportional counter and the scintillation counter. Both detecting methods are based on the X-ray interaction with the matter the detector is made of, and its consequent ionization or excitation.

##### II.1.1.4.1 Gas-flow Proportional Detector

When an X-ray interacts with an inert gas, outer shell electrons are usually ejected, giving rise to a positively charged ion, e.g. for argon :



The number of ion pairs produced by the incident X-ray beam is proportional to the radiation energy  $E_0$ , and is given by :

$$n = \frac{E_0}{\epsilon} \quad , \quad (\text{II.6})$$

where  $\epsilon$  is the energy necessary for the formation of an ion pair.

The gas-flow proportional detector basically consists of a 3 cm diameter metal box and a thin tungsten wire

(0.05 mm in diameter) along the middle of the box, which is the anode. A mixture of 90% of argon and 10% of methane, at a little above atmospheric pressure flows through the counter. The counter wall is fitted with a thin window (thickness of one micron) through which the incident X-rays may enter the proportional counter. This window is protected against the external spectrometer vacuum by the small secondary collimator. Another thicker window (6  $\mu\text{m}$ ) is placed at the exit to allow the radiation to enter the scintillation counter, if necessary. Both windows are coated with aluminium in order to ensure a uniform electric field inside the detector. Figure II.3 schematically illustrates the gas-flow proportional counter used in the present work.

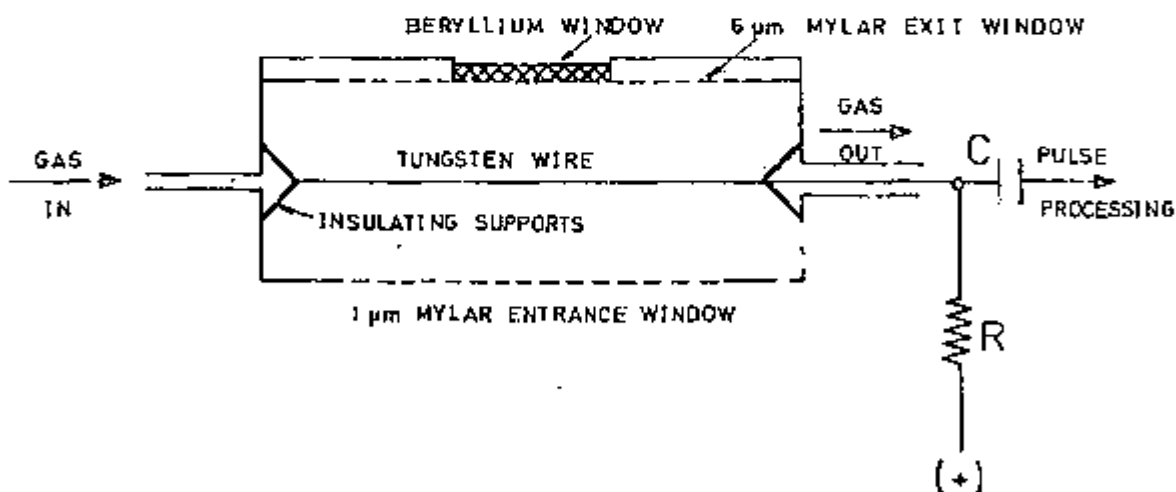


Figure II.3

The gas-flow proportional counter

An X-ray photon entering the detector produces  $n$  ion pairs according to equation (II.6). The difference in potential between the cathode (which is earthed) and the anode wire (which carries an initial positive voltage of

1.4-1.7 kV) prevents the recombination of these ions and compels the electrons towards the anode. The electrons thus generated are accelerated towards the anode, due to the electric field. The electrons may collide with other argon atoms in their trajectory, in which case part of the stored energy may be made available, allowing a new ionization. The initial number of electrons is thus multiplied, as the electrons get closer to the anode, where the field is stronger. This effect is responsible for a huge multiplication of the number of electrons (N) which finally reach the anode (Friedman, 1949). The gain G is given by :

$$G = \frac{N}{n} = \frac{N\epsilon}{E_0} \quad , \quad (II.7)$$

where G is normally of the order of  $10^4$  to  $10^5$ .

One of the common problems associated with gas-flow proportional counters concerns the so called dead time. This effect has its origin in the decrease of the electric field in the vicinity of the anode wire, due to the relatively slow dissipation of the positive ions. The true count rate will therefore be lowered by an amount given by :

$$I_t = \frac{I_m}{1 - I_m t_d} \quad , \quad (II.8)$$

where :  $I_t$  = true count rate;

$I_m$  = measured count rate;

$t_d$  = average dead time value.

Normally,  $t_d$  is of the order of 1-2  $\mu$ s.

Problems also arise when the energy of the X-rays entering the proportional counter is greater than the absorption edge energy of the counter gas. This can give rise to the so called "escape-peak" phenomena. The resulting escape peak will have an energy that corresponds to the difference between the energy of the incident radiation and the energy required to ionize a core electron of the argon atom (when the argon is the ionizable gas, of course). Therefore, the escape peaks will always be present on the low-energy side of the pulse associated with a particular X-ray, with an energy attenuation of about 3000 volts.

#### II.1.1.4.2 Scintillation Detector

The scintillation detector consists of two essential parts : the phosphor and the photomultiplier. The first part is normally composed of a sodium iodide crystal doped with thallium whose function is to transform the energy of the X-ray photon in a light pulse of approximately 3 eV of energy. The energy of the incident X-ray promotes valence band electrons to a higher level. The excited electrons come back to their original position emitting energy at a longer wavelength.

As the sodium iodide crystal is highly hygroscopic, the crystal holder must be hermetically sealed. The beryllium and aluminium window (0.2 mm of thickness) placed between the crystal and the entering radiation prevents wavelengths above  $2 \text{ \AA}$  from being measured. In Figure II.4 a simplified drawing of the scintillation counter is depicted.

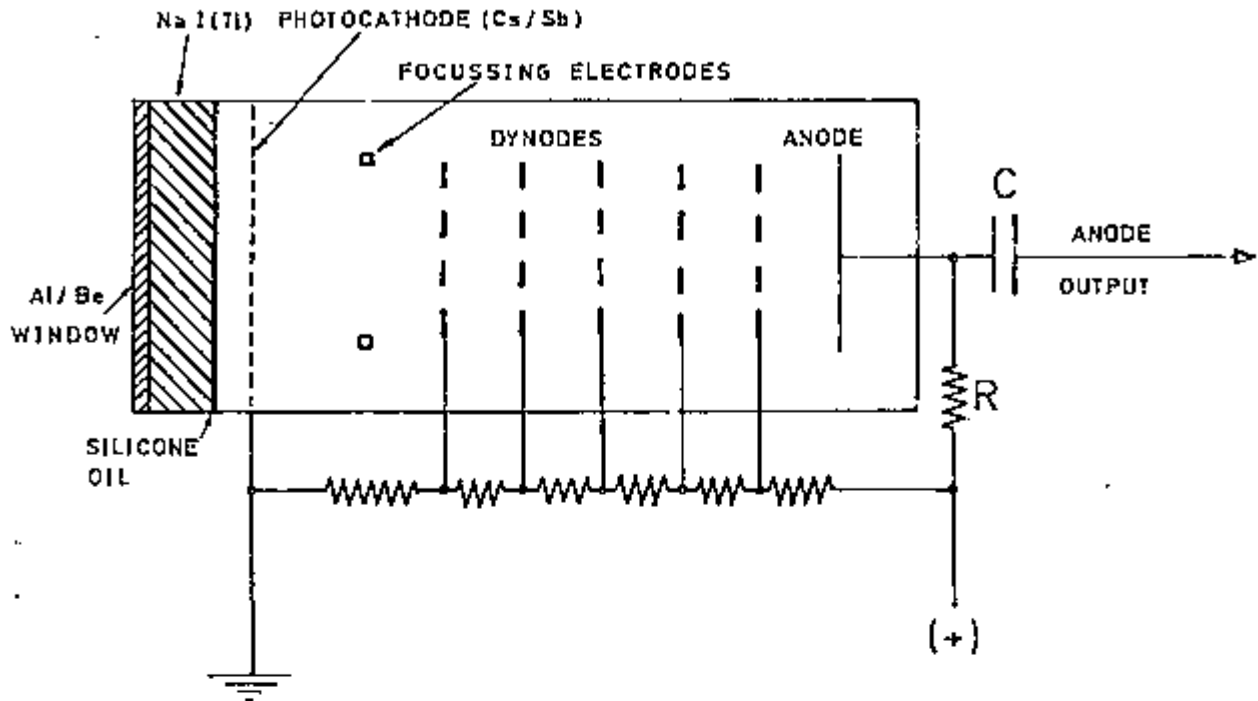


Figure II.4

## The scintillation counter

The X-rays, after having been converted into light, collide with the Sb/Cs photocathode producing electrons. These electrons are then accelerated by a series of dynodes to each of which is applied a successively higher positive potential. The voltage pulses which result are then collected and amplified as in the case for the gas-flow proportional counter.

In principle, the scintillation counter should provide a larger number of ion pairs per incident X-ray photon than the proportional counter, since the necessary energy to generate an ion pair in solids is smaller than in gases. Nevertheless, this advantage is not realized, since losses are bound to occur in the process of converting the free electrons into light pulses and of converting the light quanta into electrons in the photomultiplier. Due to these



two factors combined, the necessary energy to produce an electron is approximately 300 eV. This value is indeed larger than the energy required to produce an ion pair in the gas-flow proportional counter (30 eV). Hence, the resolution of the scintillation counter is far worse than that of the proportional counter.

The scintillation counter is also subjected to escape peak interference, mainly due to the ejection of K or L electrons from the iodine atoms in the phosphor. Of these two absorptions, however, the iodine L edge (~5 keV) does not interfere too much, since its energy is not within the normal range utilized by the detector.

#### II.1.1.5 Pulse Height Analysis

The pulses provided by the detectors relative to a given photon of energy will not be exactly of the same size, but will vary around an average value. The pulse height analyser eliminates pulses which have a voltage above or below a given range, by using a "window" that rejects all the voltage levels which are out of the range pre-established. The "window" dimensions are defined by a threshold on the side of lower voltages and, at the other end, by an arbitrary adjustment. This unit can also be used for attenuating the energy of the background level that arises from scattered primary radiation, and for separating lines of different orders of reflection which present the same angle of diffraction (equal  $\sin \theta$  in Bragg's equation).

### II.1.2 Experimental Procedure

For the  $K\alpha$  and  $K\beta$  lines of all chromium, vanadium and titanium compounds studied here, the exciting radiation was provided by the bremsstrahlung and characteristic lines of a copper X-ray tube, running at 50 mA and 50 kV. For the analysis of the soft lines, the traditional copper sealed X-ray tube was replaced by the CGR Elent 10 X-ray tube, working at a power of 4 kV x 3 mA. In order to obtain soft spectral lines, it was essential to work at starting pressures lower than  $4 \times 10^{-2}$  torr. In all cases, the photons were detected with a conventional gas-flow proportional counter in conjunction with a Harwell 2000 series counting equipment.

For the hard lines, the spectra were recorded in the "step-scanning" mode, that is, the number of counts in a given time was printed for intervals of  $2\theta$  corresponding to  $0.02^\circ$ . This method of recording the data provides a better statistical quality, as it involves counting, at a particular spectrometer setting, for a period of time as long as desired.

Nevertheless, we did not manage to use the "step-scanning" mode for the soft lines, because the X-ray discharge tube produced interference pulses, which stopped the step-scanning unit. Therefore, for the soft spectral lines, the data were recorded by means of a chart recorder, running at a speed of  $0.25^\circ (2\theta)$  per centimetre.

ELEMENT AND LINE	ENERGY (eV)	DISPERSING CRYSTAL	ORDER OF REFLECTION	ANGLE OF INCIDENCE ( $2\theta$ )
CHROMIUM				
K $\alpha$	5411	ADP	4	118.92°
K $\beta$	5946	ADP	4	103.22°
L $\alpha$	573	RbAP	1	111.88°
VANADIUM				
K $\alpha$	4949	ADP	4	140.67°
K $\beta$	5426	ADP	4	118.36°
L $\alpha$	511	RbAP	1	136.36°
TITANIUM				
K $\alpha$	4508	EDDT	3	138.96°
K $\beta$	4931	EDDT	3	117.79°
L $\alpha$	452	Pbmyr	1	40.60°
OXYGEN				
K $\alpha$	525	RbAP	1	129.45°
CARBON				
K $\alpha$	277	Pbmyr	1	69.00°
NITROGEN				
K $\alpha$	392	Pbmyr	1	47.20°
FLUORINE				
K $\alpha$	677	RbAP	1	89.07°

Table II.1

Energy, dispersing crystal, order of reflection and angle of incidence used for the analysis of X-ray lines

(from White & Johnson, 1970)

CRYSTAL DESIGNATION	CRYSTAL NAME	d SPACING (Å)
EDDT (020)	ETHYLENEDIAMINE D-TARTRATE	8.81
ADP (101)	AMMONIUM DIHYDROGEN PHOSPHATE	10.64
RbAP (100)	RUBIDIUM ACID PHTHALATE	26.12
Pbmyr	Pb MYRISTATE	79.00

Table II.2

Analysing crystals used and corresponding d spacing

In order to obtain the best compromise between efficiency and resolution, a number of crystals were tried, as well as different orders of reflections. The best results were obtained with the conditions described in Tables II.1 and II.2.

## II.2 Practical Aspects of X-ray Photoelectron Spectroscopy

The basic components required to perform an XPS experiment consist of a source of X-radiation, which is used to excite photoelectrons from the sample; the electron spectrometer, which measures the kinetic energy of the emitted electrons; and, finally, some form of detection. The anode materials most commonly utilized in XPS X-ray sources are Mg and Al. Both elements give rise to a complex X-ray

spectrum in which the strongest line (the unresolved  $K\alpha_{1,2}$  doublet) results from the transition  $2p_{1/2,3/2} \longrightarrow 1s$ . The other lines present in the spectra are satellite lines whose origin can be understood as due to transitions  $2p \longrightarrow 1s$  in atoms which are doubly or triply ionized. Unless very weak peaks are to be studied, when possible interference from satellite lines associated with other more intense peaks can occur, these satellite peaks do not interfere with the final spectra. In Mg and Al X-ray tubes, the most intense satellites,  $K\alpha_3$  and  $K\alpha_4$ , occur at about 10 eV above the  $K\alpha_{1,2}$  peak and present an intensity of approximately 8% and 4% of  $K\alpha_{1,2}$ , respectively. Photoelectron spectra obtained with non-monochromatized sources of this type thus always exhibit a characteristic double peak at kinetic energies about 10 eV above the strong  $K\alpha_{1,2}$  peak. The other satellite lines can be neglected, as they are normally less than 1% of the main peak in magnitude.

A very thin X-ray transmitting aluminium window separates the sample and the anode. This window prevents the electrons scattered from the anode from interfering in the analysis, and reduces part of the white radiation which is responsible for the high background observed in photoelectron spectra. The instrumental resolving power of such an apparatus will therefore be limited by the natural line width of the  $K\alpha_{1,2}$  line used. The full width at half-maximum intensity (FWHM) is about 0.8 eV for Mg  $K\alpha_{1,2}$  and 0.9 eV for Al  $K\alpha_{1,2}$ .

Basically, X-ray photoelectron spectra can be obtained for samples in different physical states (gaseous, liquid or

solid). The description of the experimental apparatus used in the present work, however, will be concerned with analysis of solid samples. Indeed, all the samples studied were in the form of a finely ground powders. The sample amount which was exposed to excitation normally did not exceed a circular region of diameter 5 mm. These samples were introduced into the spectrometer mounted on a double sided sellotape. Unfortunately, this procedure can have the inconvenience of giving interference peaks in the final spectra, especially if one is interested in carbon and oxygen peaks.

Inelastic scattering effects drastically reduce the emission of photoelectrons, restricting the sample analysis to a mean depth of only 10-80 Å. Therefore, any change of the chemical composition in the first atomic layers due to surface contamination will seriously affect the resulting spectrum. In order to minimize surface contamination, it is important to keep the sample chamber at very low pressures, approximately  $10^{-9}$  torr. This is done by using liquid-nitrogen cooled oil-diffusion pumps. An argon ion gun is also available in the preparation chamber, directly above the target, and can be used to reduce surface contamination present in the sample. This argon ion gun consists of a cold cathode electron gun with ion beam extraction, acceleration and focusing. The device must, however, be used with great care as an exposure of the sample to the beam (20 mA, 2-4 kV) for only a few minutes can cause serious damage (especially reduction) to the chemical composition of the sample surface, interfering in the results.

In Figure II.5 the X-ray photoelectron spectrometer used in the present work is schematically represented.

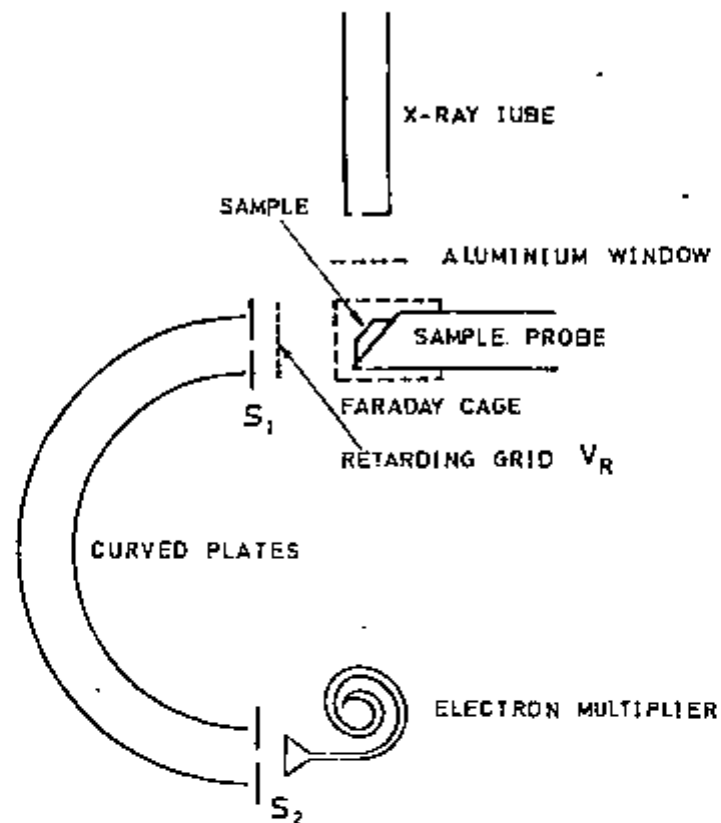


Figure II.5

Schematic representation of the photoelectron spectrometer

The X-ray tube can be operated up to a maximum of 990 W and is capable of supplying a voltage potential from 0 to 15 kV, and a current of 5, 10, 20, 40 and 66 mA.

The sample preparation chamber and the spectrometer chamber are connected by a gate valve. Before introducing the probe into the spectrometer chamber, the sample preparation chamber must be evacuated until the pressure reaches  $10^{-6}$  torr. The gate valve between the two areas can then be opened, and the sample probe is moved into position by its own transfer mechanism.

The characteristic electrons that are emitted from the target material enter the energy analyser through an entrance slit ( $S_1$ ) after being subjected to a retarding potential ( $V_R$ ). The energy analyser consists of two curved plates. The electrons passing between these plates will describe different paths depending upon their energies and the potential difference ( $V$ ) between the analyser plates.  $V$  can be pre-set to give analysing energies of 5, 10, 20, 50 and 100 eV. The resolution of the photoelectron peak is greatly improved if the analysing energy is decreased, but the corresponding intensity is dramatically reduced, as well. For that reason, our experimental work was done using an analysing energy of 50 eV.

Considering that the electrons are retarded to an energy  $-E_R$  by the retarding grid ( $V_R$ ) and that the analyser allows only the photoelectrons of energy  $E \pm \Delta E$  to reach the exit slit ( $S_2$ ), the kinetic energy of these electrons is given by :

$$E_{kin} = E_R + E \pm \Delta E \quad . \quad (II.9)$$

These electrons enter a channel electron multiplier which consists of a smooth curved glass tube coated on the inside with a high resistance material and having a potential difference between its ends. This detector amplifies the current by a factor of  $10^8$  .

The pulses are then fed into a single channel analyser. The resulting spectrum can be scanned over ranges of 1, 5, 10, 25, 100 and 1000 eV in periods of 30, 100, 300, 1000 and 3000 seconds. The spectrum obtained is then displayed by an



X-Y recorder on chart paper, the count rate being registered in the Y-axis as a function of the kinetic energy in the X-axis.

If we are interested in the binding energy of the photoelectron, the accurate value of the source of energy must be known. For an aluminium X-ray tube, the binding energy in a gaseous sample will be given by :

$$E_b^V = 1486.6 - E_{kin} \quad (II.10)$$

where  $E_b^V$  is the binding energy of the electron referred to the vacuum level;  $E_{kin}$  is the kinetic energy.

For solid samples, however, the Fermi level is usually a more convenient reference level. For metals, the Fermi level has the interpretation of being the highest occupied level. The work function of a solid ( $\Phi_s$ ) is defined as the energy separation between the vacuum level and the Fermi level. Thus, an initial kinetic energy ( $E_{kin}^i$ ) at the surface of the specimen becomes  $E_{kin}$  inside the spectrometer, according to the equation :

$$E_{kin} = E_{kin}^i - (\Phi_{spect} - \Phi_s) = 1486.6 - E_b^F - \Phi_{spect} \quad (II.11)$$

where :  $\Phi_s$  = specimen work function;  
 $\Phi_{spect}$  = spectrometer work function;  
 $E_{kin}$  = recorded kinetic energy;  
 $E_b^F$  = binding energy of the electron referred to the Fermi level.

For semiconductors and insulators, however, the problem of locating the Fermi level is not so simple, as it lies somewhere between the filled valence band and the empty conduction band.

### II.3 Spectrometer Broadening. Determination of the True Line Profile

Both X-ray emission and X-ray photoelectron spectra are subjected to experimental broadening effects. In this section, we shall study a technique normally used in an attempt to eliminate or reduce these effects to supply the "true-line" profile.

#### II.3.1 Introduction

According to diffraction theory, the lines associated with a sample of any polycrystalline species in powder should appear extremely sharp. In practice, however, due to the combined effect of a series of instrumental and physical factors, such lines will be considerably broadened.

For the determination of any wavelength ( $\lambda$ ), the X-ray line cannot be considered as a monochromatic wavelength, but rather it must be recognized as having a wavelength profile. The intensity in a small range  $d\lambda$  may be described by the expression :

$$dI = t(\lambda - \lambda_0) d\lambda \quad , \quad (II.12)$$

where  $\lambda_0$  is the wavelength at the peak of the profile and  $t(\lambda - \lambda_0)$  is the intensity distribution.

The true line profile will thus be modified by the spectrometer characteristics. The effect of any X-ray diffraction apparatus in modifying a pure diffraction maximum can be analysed by employing the superposition theorem (Spencer, 1939, 1949). According to this theorem, the profile of the observed maximum  $f(\lambda)$  is the convolution, or fold, of the pure diffraction profile  $t(\lambda)$  and the weight function of the apparatus  $m(\lambda)$ . This statement can be expressed as :

$$f(\lambda') = \int_{-\infty}^{+\infty} t(\lambda) m(\lambda' - \lambda) d\lambda \quad , \quad (\text{II.13})$$

where  $\lambda'$  and  $\lambda$  represent independent values of the spectrometer setting;  $f(\lambda')$  is the corresponding intensity; and  $m(\lambda' - \lambda)$  refers to the total instrumental smearing function. Since the data are collected in terms of angles rather than wavelengths, it is convenient to express equation (II.13) in the form :

$$f(\theta') = \int_{-\infty}^{+\infty} t(\theta) m(\theta' - \theta) d\theta \quad . \quad (\text{II.14})$$

The function  $m$  expresses the sum total of the apparatus effects upon the pure function being measured. In general, the functions  $f$  and  $m$  are known and the problem is how to determine  $t$ ; the determination is called unfolding. This problem has been approached by several authors (Jones & Misell, 1967; Paterson, 1950; Sauder, 1966; etc) in recent years. The two most common methods encountered in the literature for the unfolding determination are based either on the Fourier theory or on the iterative deconvolution

theory.

The Fourier theory expresses the known functions as series of harmonic functions (Porteus, 1962; Stokes, 1948; Wertheim, 1975). The analysis is based on the fact that the Fourier transform of a convolution of two functions is the product of the Fourier transform of the functions.

The iterative deconvolution method is based on repeated convolution of  $f$  with  $m$  to yield  $t$ , in which numerical integrations are performed. This method was proposed for the first time by Burger and van Cittert (1931, 1932a, 1932b) and has been applied by Ergun (1968) to X-ray diffraction profiles. As this latter approach is used in the present work, it will be discussed in some detail in section II.3.3.

Although it was stated that the functions  $f$  and  $m$  are normally known, the exact determination of the machine function is by no means trivial. It is therefore needed to study the various broadening effects separately, indicating how they can be taken into account in the deconvolution procedure, whether analytically or experimentally.

### II.3.2 Spectrometer Broadening Effects

For the PW1410, the geometrical machine function denoted by  $m(\theta' - \theta)$  may be reasonably regarded as consisting of two specific instrumental functions  $m_r$  and  $m_c$ . The total instrumental profile is then given by the convolution product of these two functions :

$$m(\theta' - \theta) = m_r * m_c \quad , \quad (II.15)$$

where  $m_r$  is the crystal rocking curve and  $m_c$  is the total collimator function; the notation  $*$  indicates a convolution product. The value of the total collimator function in its turn may be evaluated as :

$$m_c = m_h * m_v \quad , \quad (II.16)$$

where  $m_h$  is the horizontal divergence function and  $m_v$  is the vertical divergence function.

#### II.3.2.1 $m_h$ , $m_v$ and $m_r$

A description of collimator orientations can be facilitated by defining the rotation axis of the crystal as pointing in the vertical direction. Of course, the choice of the collimator orientations and the associated divergence functions is arbitrary. We have attempted, in this respect, to be coherent with the convention most commonly encountered in the literature. Nevertheless, it must be emphasized that in the particular case of the Philips PW1410 spectrometer the rotational axis of the crystal is in a horizontal plane.

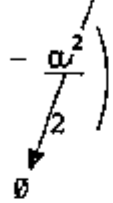
The vertical divergence ( $\alpha$ ) of an incident beam is defined as the angle between the beam and its projection on a plane perpendicular to the instrument axis (i.e., a horizontal plane). Here, it is not necessary to establish a sign convention for the angles, since the  $m_v$  function is symmetric with respect to beams situated above or below the horizontal plane. On the other hand, the horizontal divergence ( $\Phi$ ) of a beam is the angle between the beam and



Since  $\alpha$  is small, we can use  $\phi'$  instead of  $\phi$ . This can be seen as follows :

$$\sin \phi = \sin \phi' \cos \alpha \quad . \quad (II.17)$$

Therefore, for small angles :

$$\phi = \phi' \left( 1 - \frac{\alpha^2}{2} \right) \quad (\text{in radians}), \quad \text{or } \phi \sim \phi' \quad . \quad (II.18)$$


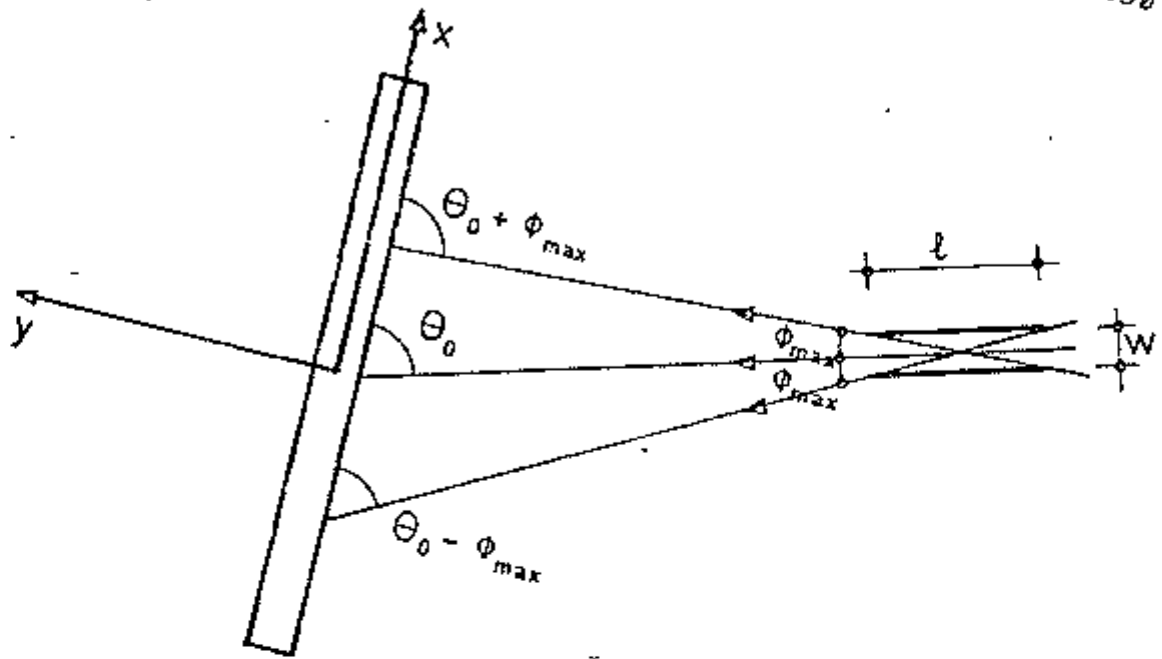
In a similar fashion, we can assume the approximation :

$$\alpha \sim \alpha' \quad . \quad (II.19)$$

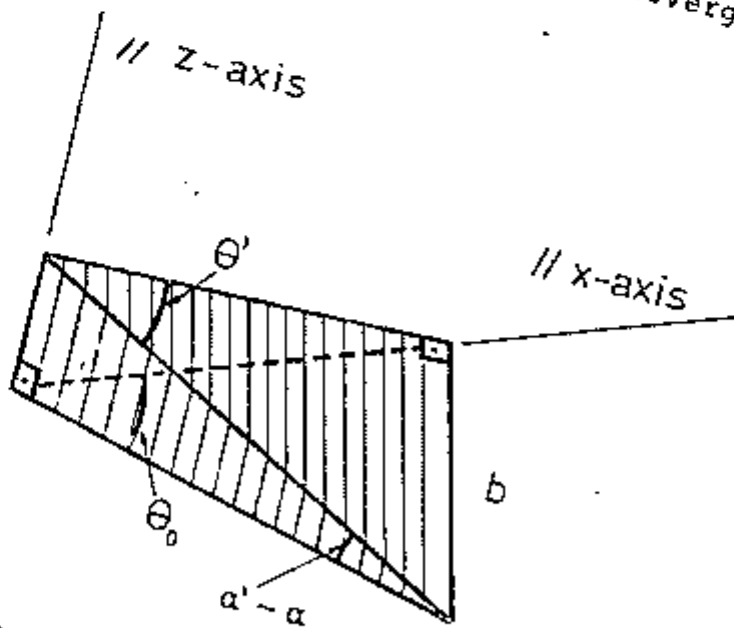
The primary collimator limits the direction of the X-rays in the incident beam to that included in the angle  $2\phi_{\max}$ , which can be seen in Figure II.7.a. X-rays travelling parallel to the plates of the collimator and forming an angle zero with the collimator axis (central ray), will encounter the crystal surface at the Bragg angle,  $\theta$ , and will be reflected into the detector. Yet, due to the crystal rotation, the divergent rays lying between  $\pm\phi_{\max}$  may eventually satisfy Bragg's equation, so that they are also reflected into the detector, together with the central ray. The characteristic curve of the detector will therefore have an approximately triangular shape, with base equal to  $2\phi_{\max}$  (Soller, 1924), where  $\phi_{\max}$  is the maximum horizontal divergence :

$$\phi_{\max} = \text{arc tan } (w/\ell) \quad , \quad (II.20)$$

with :  $w$  = distance between the collimator blades =  $150 \mu\text{m}$ ;  
 $l$  = collimator length =  $12.2 \text{ cm}$ .



(a) Geometry of the horizontal divergence



(b) Geometry of the vertical divergence

Figure II.7



Hence we conclude that the horizontal divergence, which gives rise to the horizontal divergence function ( $m_h$ ), depends neither on the Bragg angle ( $\theta_0$ ) nor on the X-ray wavelength ( $\lambda$ ). This effect will be consequently constant for any region of the spectrum under investigation. For the Philips PW1410 spectrometer with the gas-flow proportional counter in use,  $\Phi_{\max}$  has the value of  $0.07045^\circ$ .

All X-rays parallel to the primary collimator are allowed to pass through it. Let us consider rays forming an angle  $\alpha' - \alpha$  with a plane perpendicular to the crystal axis - see Figure II.7.b. We may easily deduce from this figure that :

$$\cos \alpha = \frac{b}{\sin \theta_0} \frac{\sin \theta'}{b} = \frac{\sin \theta'}{\sin \theta_0} \quad \text{and} \quad (\text{II.21})$$

$$\sin \theta' = \cos \alpha \sin \theta_0 \quad . \quad (\text{II.22})$$

We therefore conclude that the incidence angles of these rays ( $\theta'$ ) are always smaller than the Bragg angle of the central ray ( $\theta_0$ ). Moreover, it can be seen that the vertical divergence, which gives rise to the vertical divergence function ( $m_v$ ), does depend on the Bragg angle  $\theta_0$  and, consequently, on the X-ray wavelength ( $\lambda$ ). The vertical divergence function thus gives rise to high-angle distortion of the peak shape. After rotation of the crystal by a certain angle  $\Delta$ , these rays may be Bragg reflected, that is,  $\theta'$  becomes  $\theta_0$  when the central ray strikes at an angle of  $(\theta_0 + \Delta)$ . The value of  $\Delta$  comes out from the following

expression :

$$\sin \theta_0 = \cos \alpha \sin (\theta_0 + \Delta) \quad , \quad (\text{II.23})$$

The maximum value of the vertical divergence  $\alpha$  is given by :

$$\alpha_{\max} = \arctan (t/s) \quad , \quad (\text{II.24})$$

where :  $t$  = height of the primary collimator blades = 3 cm;

$s$  = total X-ray path between the sample and the  
detector = 25 cm.

For the Philips PW1410 spectrometer with the gas-flow proportional counter in use,  $\alpha_{\max}$  is approximately  $7^\circ$ . It is clear that the vertical divergence function ( $m_v$ ) will only seriously compromise a peak profile at high  $\theta$  angles. The  $m_v$  function will then be altogether asymmetric and it will introduce low energy tails into all peaks (Haycock & Urch, 1978).

As already mentioned, the machine broadening function will be also affected by the crystal rocking curve ( $m_r$ ). The ideal crystal function is defined by considering the spectrometer response for monochromatic radiation having a degree of collimation much finer than the diffraction width of the crystal. A schematic representation of the rocking curve for an ideal crystal can be seen in Figure II.8.

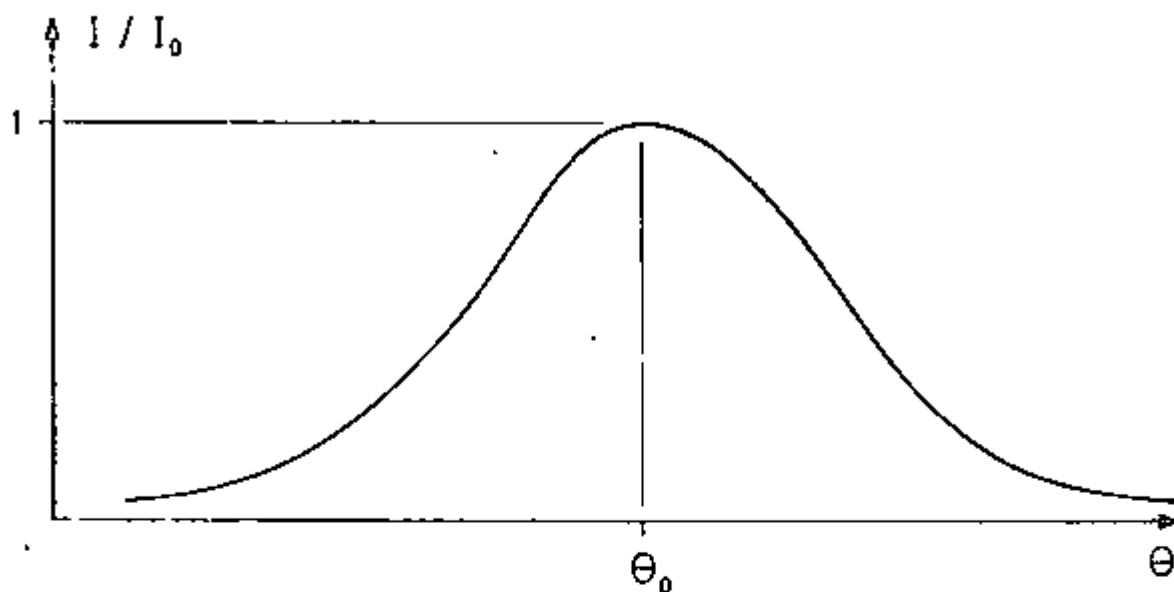


Figure II.8

Single crystal rocking curve  $c_{\lambda}(\theta)$  from Burek (1975).

In practice, the crystals in use are built up by a so called mosaic of very small units. These units are roughly oriented in the direction of the cleavage planes of the crystal, but may be tilted some minutes of arc from that direction. The profile of the function will be broadened, since there is a misorientation of the upper blocks relative to the average surface of the crystal. The total diffracted intensity can therefore be increased at the expense of a broadened diffracted profile. The FWHM of a rocking curve of a mosaic crystal is of the order of some minutes of arc, whereas in the case of an ideal crystal it is not larger than 1-10 seconds of arc. One advantage of using a mosaic crystal is that the resulting rocking curve is a Gaussian due to the random nature of the crystal surface.

To avoid dealing analytically with the vertical divergence function (since its consideration is not trivial at all), we have attempted to attenuate this effect experimentally by introducing another collimator in the X-ray trajectory, between the primary collimator and the analysing crystal. This secondary collimator with dimensions 3 cm x 6 cm x 1.5 cm and spacing 0.05 cm between blades was positioned in such a way that its blades resulted perpendicular to the blades of the primary collimator. For this new experimental array  $\alpha_{\max}$  is sensibly smaller (1.9°), thus increasing the resolving power of the equipment.

### II.3.3 Application of the Iterative Deconvolution Method

The iterative deconvolution method (Burger & van Cittert, 1932a, 1932b) was applied to the experimental spectra in order to eliminate the instrumental broadening function. This method is based on the principle that an experimental X-ray spectrum is the result of the convolution of the true line shape and the instrumental broadening function :

$$f(\theta') = \int t(\theta) m(\theta' - \theta) d\theta = t * m = m * t . \quad (\text{II.25})$$

As a crude starting point, it is assumed that the true profile ( $t_0$ ) is equal to the experimental one ( $f$ ). If this assumption were correct, the fold  $m * t_0 = m * f$  should be equal to  $f$ . Yet, this is not clearly so and the difference between  $f$  and  $m * t_0$  is then added to  $t_0$  to produce a first approximation (or unfold)  $t_1$ , according to the expression :

$$t_1 = t_0 + (f - m * t_0) = f + (f - m * f) \quad . \quad (II.26)$$

The second approximation may be obtained by folding the first approximation ( $t_1$ ) and adding the difference between  $f$  and this second fold to the first approximation :

$$t_2 = t_1 + (f - m * t_1) \quad . \quad (II.27)$$

In general, the approximation of order  $(n + 1)$  is given by :

$$t_{n+1} = t_n + (f - m * t_n) = t_n + r_n \quad , \quad (II.28)$$

where  $r_n$  is the  $n^{\text{th}}$  residual.

The procedure is repeated until a prescribed convergence criterion is satisfied. In practice, however, convergence is seen to be reasonably achieved after a small number of iterations (3 or 4), when the residual is of the same order of the statistical precision of  $f$ .

An essential condition for the method to be successfully applied is that the machine broadening function be normalized :

$$\int_{-a}^b m (\theta' - \theta) d\theta = 1 \quad . \quad (II.29)$$

Moreover, the machine broadening function must have bounded support, that is, it must have rather small uniform values in the region outside the interval  $-a$  and  $+b$ .

An especial problem arises in the successive foldings of  $t$ , due to the reduction of the validity interval for the data, after each cycle. In other words, if we consider that the domain of  $m$  is comprised within the interval  $(a + b)$ , and that  $t$  extends from  $c$  to  $d$ , then the domain of  $t * m$  will be reduced to  $(c + b, d - a)$ . To avoid such a reduction in the domain of  $t$ , it is common practice to set the unfolded function  $t$  equal to the experimental data  $f$  in the intervals  $c$  to  $c + b$  and  $d - a$  to  $d$ . This simplification produces no serious problems, since these intervals normally do not exhibit outstanding features in the profile, like maxima or minima.

A FORTRAN program used to obtain all successive folds, unfolds and residuals is included in the Appendix. This program is an adaptation of that used by Haycock (1978).

Figure II.9 illustrates the sequence of the process of unfolding the machine broadening function from the chromium  $K\beta$  spectrum of chromium (III) oxide.

Since the experimental data are affected by random errors (noise), which cause problems to the deconvolution procedure, a "smoothing" is required beforehand. This is the subject of the next section.

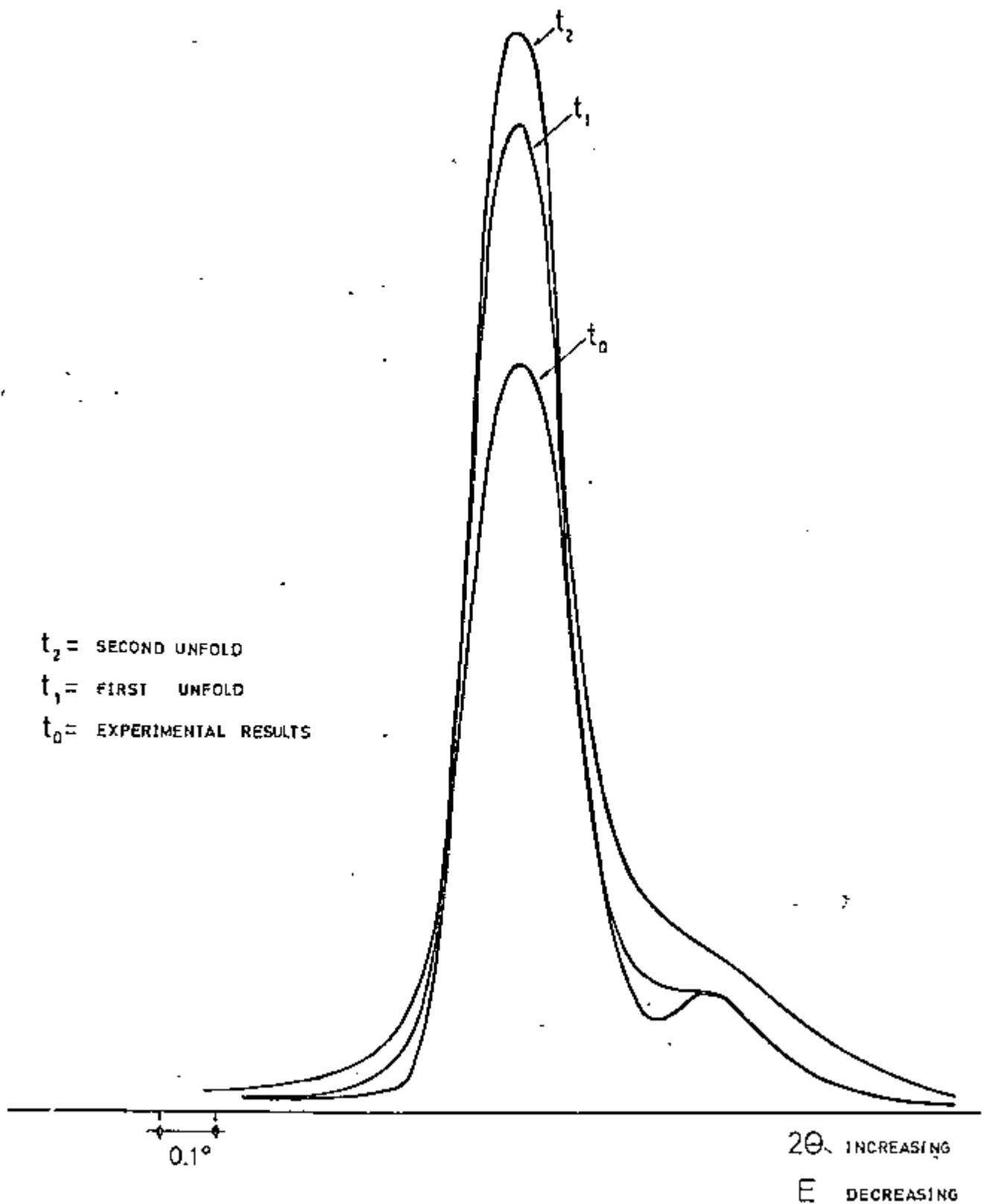


Figure II.9  
 Iterative unfold of  $\text{Cr}_2\text{O}_3$  - Cr  $K\beta_{1,3}$

### II.3.3.1 Data Smoothing by a Simplified Least-squares

#### Procedure

The removal of the noise superimposed to the experimental data, without introducing distortions, is of major importance for the satisfactory application of the iterative method. Indeed, the amplification of high frequency noise appears to limit the number of iterations which can be employed in the deconvolution. After a sufficiently large number of iterations, the calculated correction consists largely of noise components. It becomes then essential to apply a smoothing technique to the experimental results, before submitting them to the iterative deconvolution itself. The data can be considered as a linear sum of signal,  $s(\theta)$ , and noise,  $n(\theta)$  (Willson & Edwards, 1976) :

$$f(\theta) = s(\theta) + n(\theta) \quad . \quad (II.30)$$

According to Ernst (1966), the signal-to-noise ratio ( $s/n$ ) is defined as the ratio of maximum peak height to the root-mean-square value of the noise. Applying pre-smoothing will increase the signal-to-noise ratio.

One of the simplest ways to smooth fluctuating data is by a moving average. In this procedure we take a fixed number of points, add their ordinates together, and divide by the number of points to obtain the average ordinate at the centre abscissa of the group. Next, the point at one end of the group is dropped, the next point at the other end added, and the process is repeated. The above mentioned procedure is based upon the concept of a convolute and of a



convolution function, which can be generalized according to the expression :

$$I_j = \frac{\sum_{i=-m}^{+m} c_i I_{j+i}}{N} \quad , \quad (\text{II.31})$$

where :  $N = \sum_{i=-m}^{+m} c_i$  is the normalizing factor;

$j$  represents the running index of the ordinate values ( $I$ ) in the original data;

$I_j$  is the ordinate data;

$c_i$  is one of the convoluting integers.

In the case of the moving average, equation (II.31) is greatly simplified, since each  $c_i$  is equal to the unity and, therefore,  $N$  will be the number of convoluting integers. Nevertheless, this procedure is not the most favourable when, as in the present situation, the experimental spectra include one or more sharp peaks.

The polynomial function which best fits a plot of experimental points may be written as :

$$f(x) = a_n x^n + a_{n-1} x^{n-1} + \dots + a_1 x + a_0 = \sum_{k=0}^n a_k x^k \quad , \quad (\text{II.32})$$

where the validity interval for  $x$  varies from  $-m$  to  $+m$  and  $x$  is equal to zero in the central point of the set of  $(2m + 1)$  values. Assuming less uncertainty in  $x$  values (abscissa) than in  $y$  values (ordinate), each  $y$  value will deviate from the fitted curve somewhat. In other words, each experimental  $y$  value will differ from the corresponding

$f(x)$  value calculated from expression (II.32). These deviations are called residuals. The method of least squares is based on the assumptions that the residuals will be randomly distributed and that the best representative curve for a set of data is that for which the sum of the squares of the residuals is a minimum over the interval being considered. The coefficients of  $f(x)$ ,  $a_k$ , are to be selected according to this criterion and the value which is obtained by this procedure is then chosen as the best value for the central point  $(x = 0)$  in the interval  $(2m + 1)$  examined.

It is however seen that the values obtained for the coefficients of  $f(x)$  are only valid for the determination of a single central point. We would have to repeat the same procedure several times, always using the same set of  $(2m + 1)$  consecutive values, but dropping one point at one end of the interval and adding one on the other end of the same interval. In each interval the best values for the  $a_k$  coefficients would then be obtained.

Savitzky and Golay (1964), using the same method of least squares, derived a series of integers which provides the best weighting function for all the interval of variation of  $x$ . In Table II.3 we present the set of integers and the corresponding normalizing factors obtained by them for a 5, 7 and 9 point smoothing. The derivation of this set of integers was done for either a cubic or quadratic function, it being found that the integers are exactly the same.

	INTEGERS	NORMALIZING FACTOR
5-POINT SMOOTHING	-3,12,17,12,-3	35
7-POINT SMOOTHING	-2,3,6,7,6,3,-2	21
9-POINT SMOOTHING	-21,14,39,54,59,54,39,14,-21	231

Table II.3

Convoluting integers of  $f(x)$  and normalizing factors for a cubic or quadratic polynomial (from Savitzky et al, 1964)

Willson and Edwards (1976) arrived at the conclusion that the shape of the curves obtained by means of a quadratic polynomial smoothing, for distinct values of  $(2m + 1)$  (9, 13 and 25, respectively) varies only slightly. They concluded that the effect of smoothing on a line shape is, therefore, approximately the same, since the FWHM/SR ratio (SR is the smoothing range in the same units of FWHM) is kept constant. The smoothing range (SR) is thus the parameter which plays the most important rôle in the choice of the better smoothing for a given curve. Obviously, the larger the value of  $(2m + 1)$ , the better will be the attenuation, as far as the FWHM/SR ratio is kept constant. If we take for the value of SR the number of points  $(2m + 1)$ , and for FWHM the number of experimental points across the line's full width at half height, we shall be able to determine the most suitable smoothing function.

In practice, the best results were obtained when we applied a five-point pre-smoothing to the experimental data.

It is intuitive that, for high-intensity peaks with FWHM relatively small (as it is the case of  $K\beta$  and  $K\alpha$ ), a large number for SR will not be convenient, since to consider  $(2m + 1)$  points in the neighbourhood of the peak, values of the tails would be included. This would be responsible for the distortion of the smoothed curve.

### II.3.3.2 Limitations of the Iterative Method

The random noise in the data generally determines the extent to which deconvolution procedure can be employed. Sometimes even the pre-smoothing of the experimental data is of restricted utility, because noise components in the relevant frequency range cannot be completely removed. This is the case, for instance, of the  $K\beta_{2,5}$  and  $L\alpha$  emission lines, where the data are characterized by a very poor signal-to-noise ratio. Indeed, any attempt to apply the deconvolution procedure to these spectra was unsuccessful, as the noise level was found to be excessive from the very first iterations.

Even in cases in which the deconvolution procedure is successfully applied, the amplification of high frequency noise appears to limit the number of iterations which can be employed. According to Wertheim (1975), after several iterations, the calculated correction (residual  $r_{n+1}$ ) consists basically of noise components. Consequently, the last calculated correction could be used to subtract the noise that has been building up with each iteration. The  $n^{\text{th}}$  iteration result ( $t_n$ ) should then be improved as follows :

$$t_n = t_n - n \underbrace{\left[ f - \int_{-\infty}^{\infty} t_n(\theta) m(\theta' - \theta) d\theta \right]}_{r_{n+1}} \quad (II.33)$$

In the above expression we have assumed that the noise added after each of the  $n$  iterations was identical to  $r_{n+1}$ .

Another restriction of the method is related to the maximum number of iterations ( $n$ ) allowed. Since the validity interval after each folding of  $t$  is reduced of  $(a + b)$ , it is clear that a large number of iterations may eventually cause it to vanish. The maximum  $n$  is therefore fixed in such a way that the validity interval for  $t_n$  still includes all the main features of the spectrum (which are assumed to be from  $m_1$  to  $m_2$ ). The number  $n$  must therefore be chosen as the least of the integer results of the following expressions :

$$n = \left[ \frac{m_1 - c}{b} \right] ; \quad (II.34)$$

$$n = \left[ \frac{d - m_2}{a} \right] ; \quad (II.35)$$

where :  $a + b$  = validity domain of the  $m$  function;  
 $c + d$  = validity domain of the  $t(\theta)$  function;  
 $m_1 + m_2$  = interval of  $t(\theta)$  which includes all the main features of the spectrum.

In our experimental work we have concluded that the maximum number of iterations allowable is 3, according to the above mentioned criterion.

### II.3.3.3 Determination of the Machine Broadening Function

$$m(\theta' - \theta)$$

In section II.3.2.1, a detailed account of the experimental functions ( $m_h$ ,  $m_v$  and  $m_r$ ), which are responsible for the broadening of the spectra, was presented. It was then seen that the major errors in spectra registered on conventional spectrometers result from the use of finite spectral slit widths. The slit distortion associated with the vertical divergence was drastically reduced by the use of a secondary collimator introduced in the trajectory of the X-rays, between the primary collimator and the analysing crystal. In these conditions, the distortion associated with the horizontal divergence (which presupposes a triangular slit function independent both of the incidence angle  $\theta_0$  and of the X-ray wavelength  $\lambda$ ) was taken, in a first approximation, as the only factor responsible for the total machine broadening function. The resulting triangular function ( $m_h$ ), after normalization, can be seen in Figure II.10. Ergun (1968) has mentioned that the unfolding of a triangular function (like  $m_h$ ) from an experimental spectrum will always yield a Gaussian curve. Yet, when this triangular function was applied to unfold our experimental spectra, it did not supply satisfactory results. In Figure II.11 we illustrate the unfolding of the triangular function ( $m_h$ ) from the aluminium  $K\alpha_{1,2}$  experimental data. Although the unfolded function has improved (FWHM =  $0.16^\circ$ ), the fine structure present on the side of lower energies did not agree well with the theoretical curve (Figure II.12).

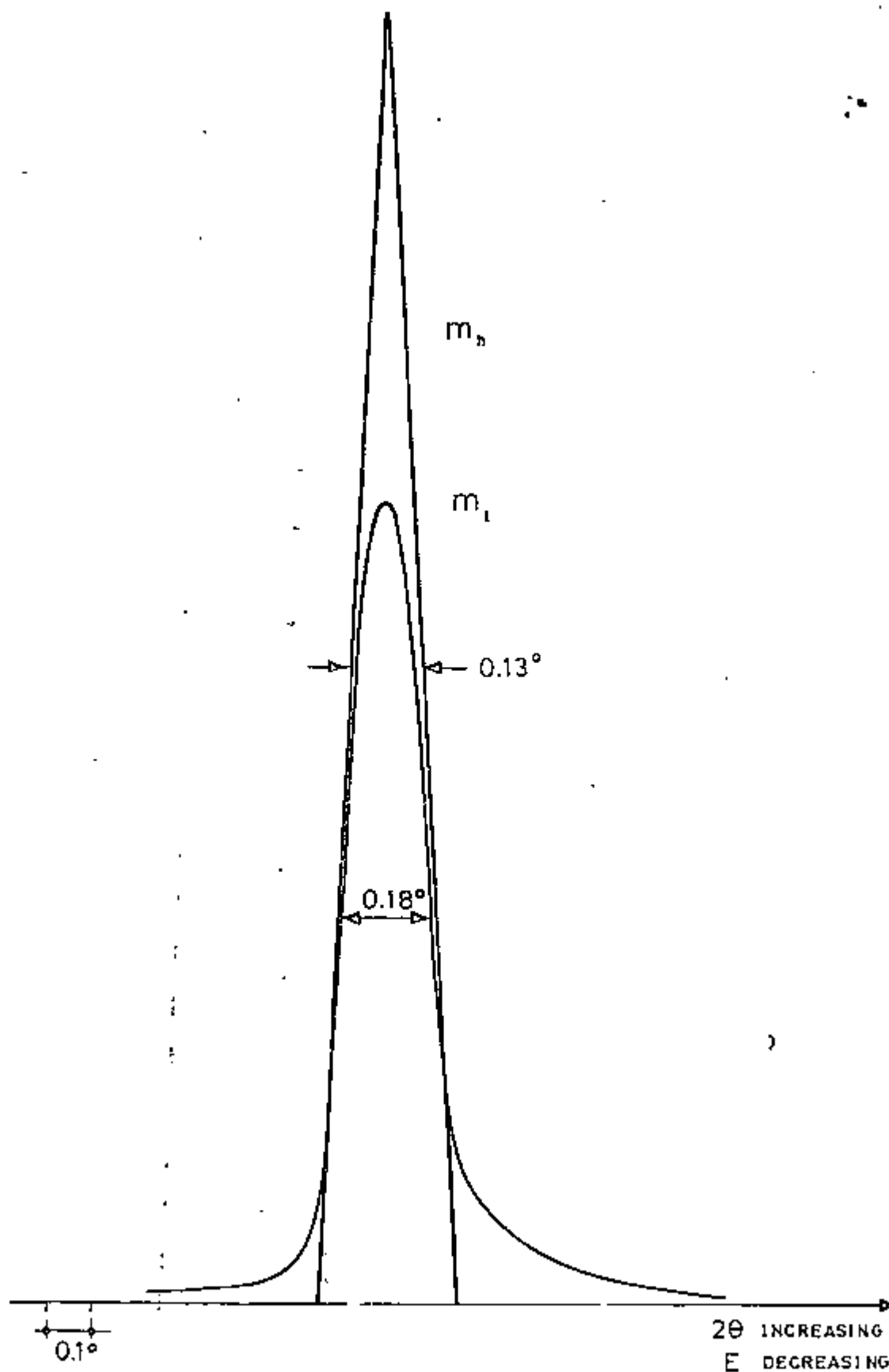


Figure II.10

Normalized triangular machine function ( $m_b$ )Normalized total machine broadening function ( $m_t$ )

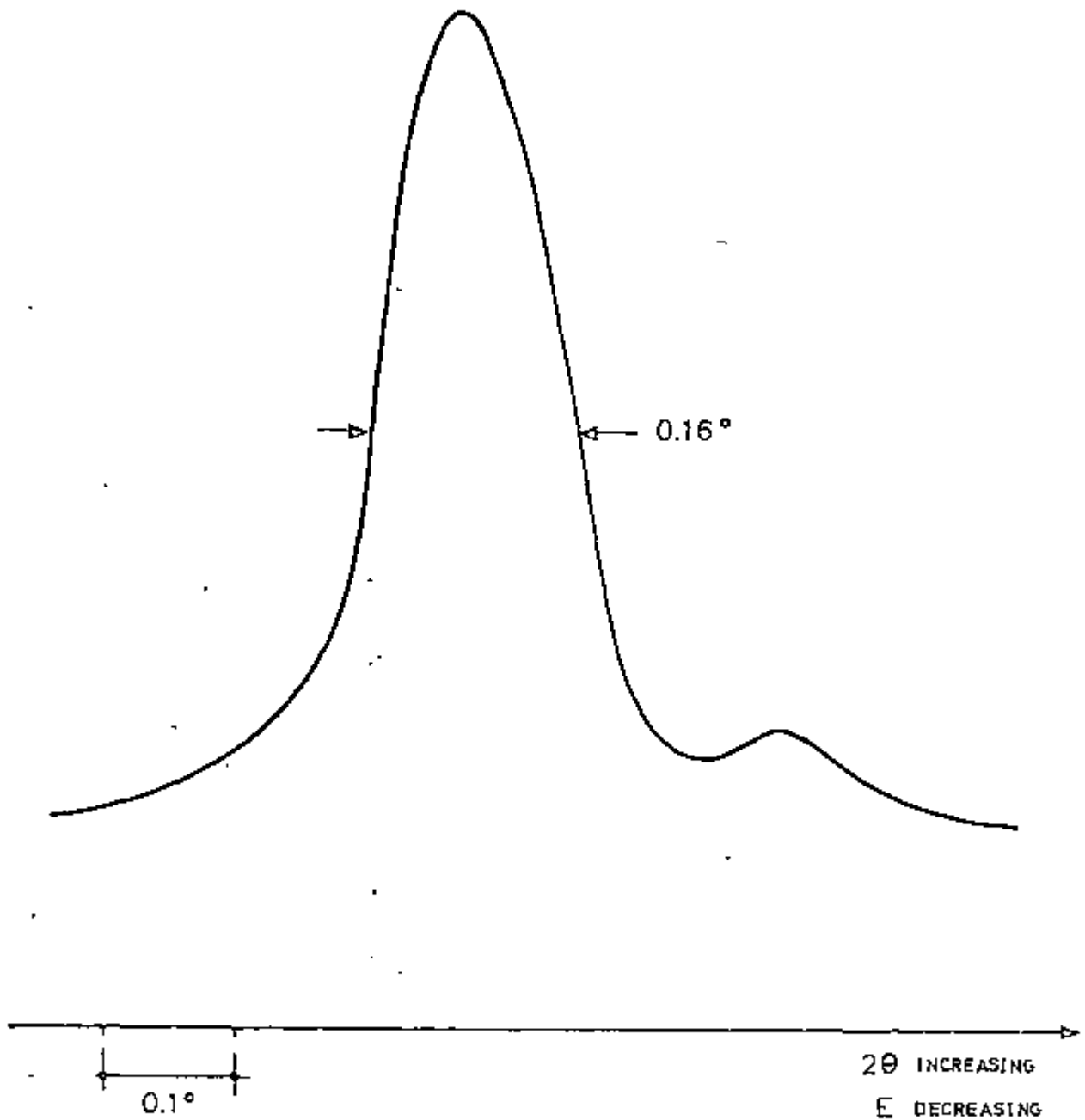


Figure II.11

Fourth unfold of the triangular function ( $m_n$ ) from the aluminium  $K\alpha_{1,2}$  experimental data



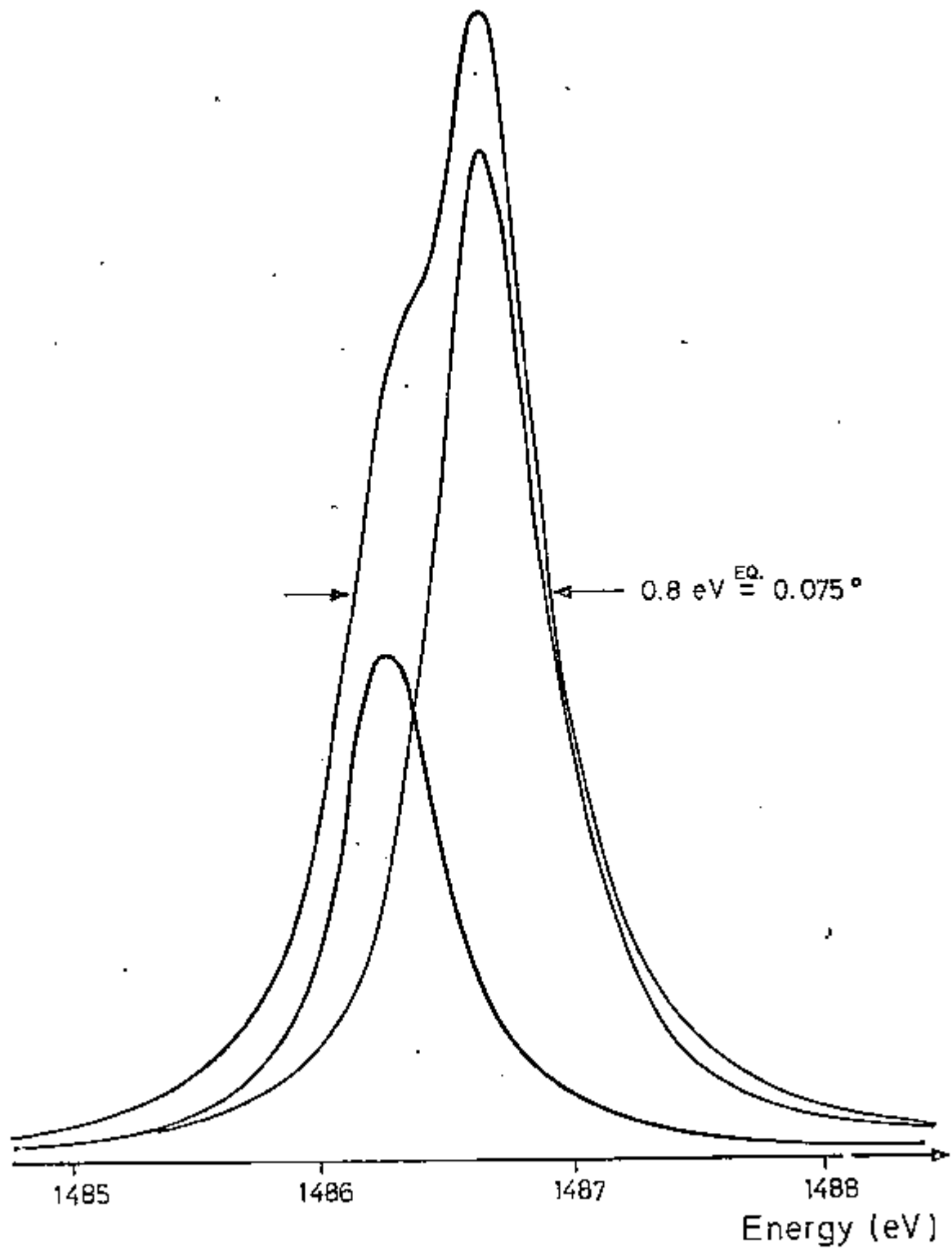


Figure II.12

Aluminium  $K\alpha_{1,2}$  obtained from Beatham et al (1976)

This unexpected fine structure has shown that the  $m_h$  function does not correspond to the true machine broadening function. We have therefore attempted to determine a new and more correct function ( $m_1$ ), capable of embracing all experimental factors responsible for the broadening of any spectrum.

An observed X-ray emission spectrum is indeed the result of the convolution of intrinsic line shapes with all the various experimental broadening functions. The iterative deconvolution method can be used to unfold the experimental spectrum and remove all the unwanted components, as described in the previous section. The spectrum thereby obtained should have enhanced resolution and the line width should be determined only by natural broadening effects associated with the finite life-times of the ionized states.

It was soon realized that the same procedure could be applied for the deconvolution of the theoretical data from the experimental spectrum in order to obtain the total machine broadening function ( $m_1$ ). In other words, the unfolding of the theoretical X-ray emission line from the experimental spectrum of the same element should supply a function which is expected to contain all relevant experimental broadening effects due to the spectrometer in use. This procedure requires the accurate knowledge of the natural line shape of a suitable X-ray line. Beatham and Orchard (1976) have discussed some characteristics of the aluminium K $\alpha$  radiation. These data (Table II.4) were obtained from an optimization by computer simulation studies of a number of experimental results found in the literature

(Dodd et al, 1968; Fischer et al, 1965 and Laüger, 1971).

Using the data of Table II.4 and supposing that each line ( $K\alpha_1$  and  $K\alpha_2$ ) is described by a Lorentzian curve, we have managed to determine the theoretical spectrum of the metallic aluminium  $K\alpha_{1,2}$ .

LINE	POSITION RELATIVE TO THE $\alpha_1$ LINE (eV)	FWHM (eV)	RELATIVE INTENSITY
$\alpha_2$	- 0.416	0.50 ± 0.02	50
$\alpha_1$	0	0.50 ± 0.02	100

Table II.4

Characteristics of the energy distribution of Al  $K\alpha_{1,2}$  radiation (from Beatham et al, 1976)

The expression of the normalized Lorentzian function, with centre at  $x = 0$ , is :

$$y = \frac{1}{a\pi} \left( \frac{a^2}{a^2 + x^2} \right) , \quad (II.36)$$

where :  $a = \frac{\text{FWHM}}{2}$  . (II.37)

The obtained aluminium  $K\alpha_{1,2}$  theoretical curve can be seen in Figure II.12. The total line width of this resulting curve is 0.8 eV.

Of course, the program of the Appendix must be adapted, so that it may serve the purpose of finding  $m_1$ . In the original program, when the problem was the unfolding of f, f

and  $m$  varied in opposite directions (since for a positive increment  $d\theta$  - see equation (II.25) - the independent variable of  $f(\theta)$  increases, whereas that of  $m(\theta' - \theta)$  decreases). Analogously, in the problem of determination of the  $m$  function from  $t$  and  $f$ , the values of  $t$  and  $f$  must be supplied in opposite directions, the result of the unfolding (which is  $m$ ) being obtained in the same direction as  $f$ .

The machine broadening function ( $m_t$ ) determined by this procedure is also illustrated in Figure II.10. We see that it is not perfectly symmetric and, furthermore, presents a more pronounced effect on the lower energy side. The fine structure is probably due to some residual vertical divergence, which was not completely attenuated by the extra collimation (section II.3.2.1).

In Figure II.13 we show, for the sake of a comparison, the result of the unfolding of this new machine broadening function ( $m_t$ ) from the same aluminium  $K\alpha_{1,2}$  experimental data. Indeed, the function  $m_t$  does include other effects like ( $m_s$  and  $m_v$ ) which were not present in  $m_h$ . By simply comparing the FWHM of the two machine functions (Figure II.10), we can demonstrate this fact: the  $m_t$  function (FWHM =  $0.18^\circ$ ) is sensibly wider than  $m_h$  (FWHM =  $0.13^\circ$ ). Moreover, the aluminium spectrum (Figure II.13) determined after the unfolding of  $m_t$  from the experimental data, does not have the undesirable fine structure on the side of lower energies, and it is closer to the true line shape than the spectrum determined by using  $m_h$  (Figure II.11) is.

We therefore conclude that  $m_t$  describes better the broadening effects due to the spectrometer geometry. This

function was indeed used as the machine broadening function  $m(\theta' - \theta)$  in the iterative deconvolution method for all the  $K\alpha$  and  $K\beta$  spectra presented in the next chapters.

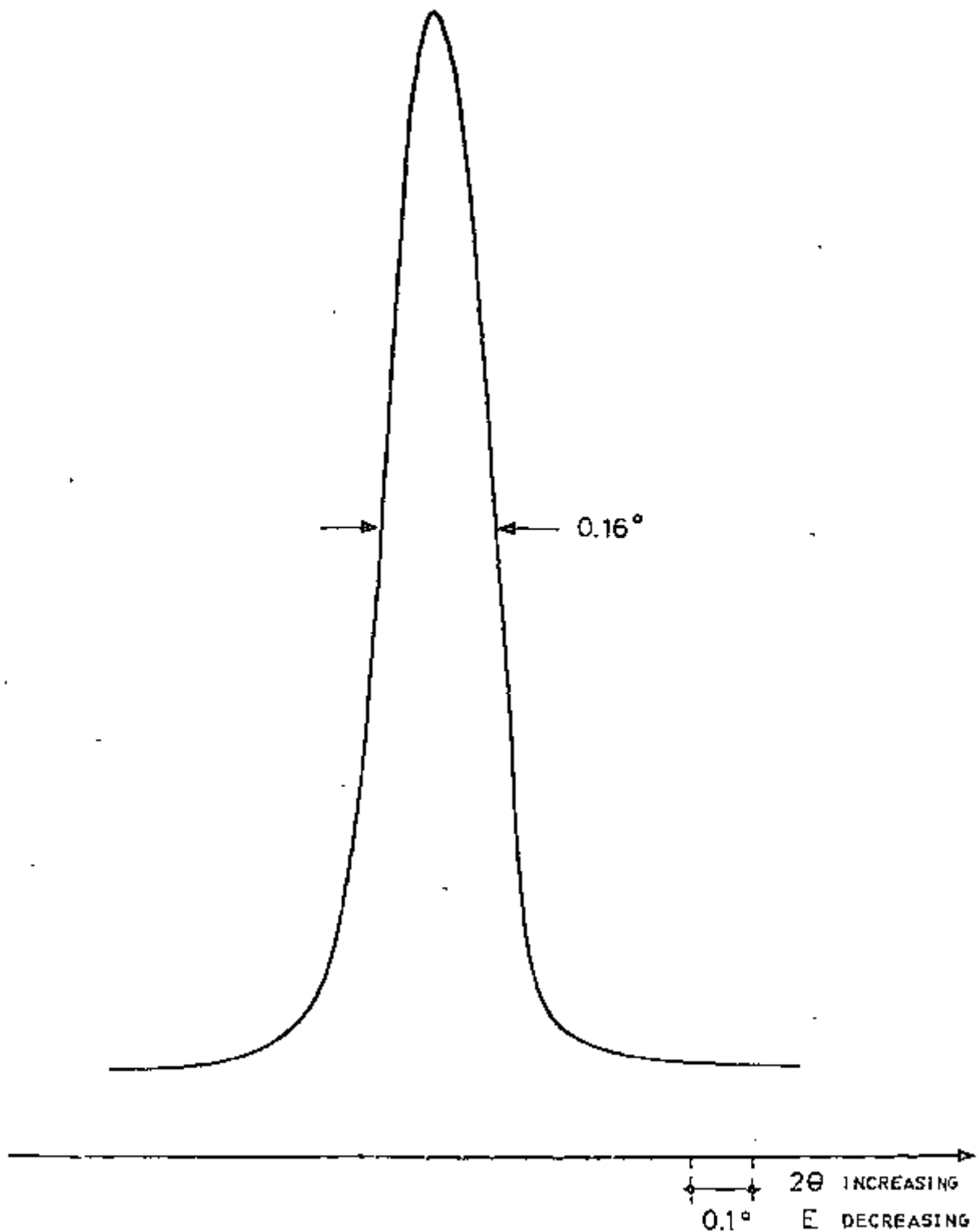


Figure II.13

First unfold of the total machine broadening function ( $m_t$ )  
from the aluminium  $K\alpha_{1,2}$  experimental data

CHAPTER IIITHE  $K\beta$  SPECTRUM OF FIRST-ROW TRANSITION METAL COMPOUNDSIII.1 Introduction

When the various X-ray emission peaks for a transition metal compound are studied, we can observe the influence of "chemical effects". These "chemical effects" are by no means exclusive to X-rays originating from valence-shell to inner-orbital transitions. They can sometimes be seen in the transitions involving inner-shell orbitals, as well.

In this chapter the X-ray emission spectra for the  $K\beta$  line of several titanium, vanadium and chromium compounds will be presented and discussed. Position, intensity and shape of peaks will be studied, so as to obtain a complete analysis of the above mentioned spectra. The intensity is normally measured in relation to other existing peaks, whereas the peak position may be determined in absolute terms.

The  $K\beta_{1,3}$  X-ray diagram arises from the electronic transition  $3p \rightarrow 1s$ . In the final configuration the  $3p^5$  state splits into two energy levels  $3p_{3/2}$  and  $3p_{1/2}$ , due to the spin-orbit coupling. The  $K\beta$  emission spectrum should therefore consist of two lines relative to the transitions  $3p_{3/2} \rightarrow 1s$  ( $K\beta_1$ ) and  $3p_{1/2} \rightarrow 1s$  ( $K\beta_3$ ). In practice, however, it is found that the doublet  $\beta_1$  and  $\beta_3$  is not resolved, and the final result is a single peak known as  $K\beta_{1,3}$ .

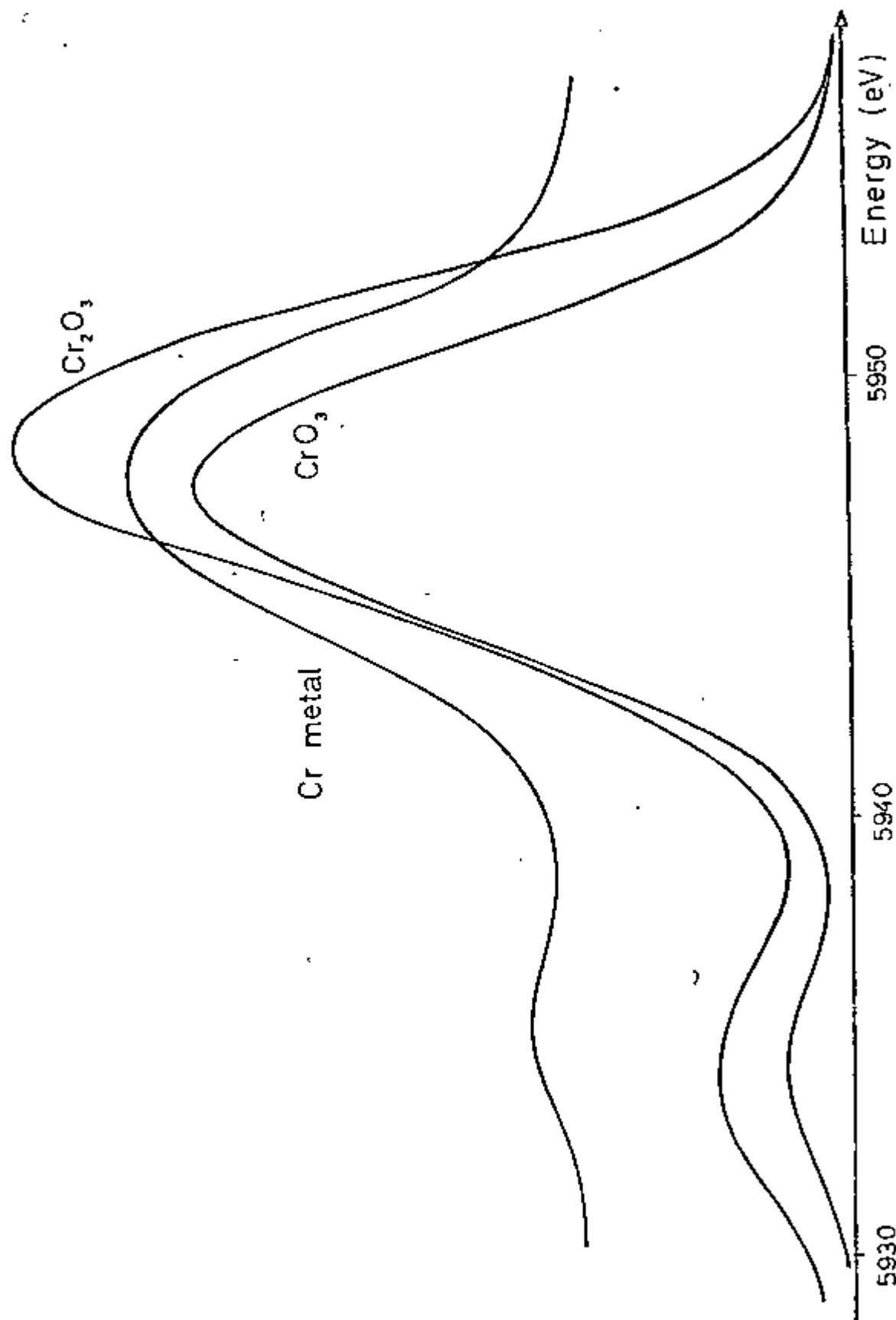
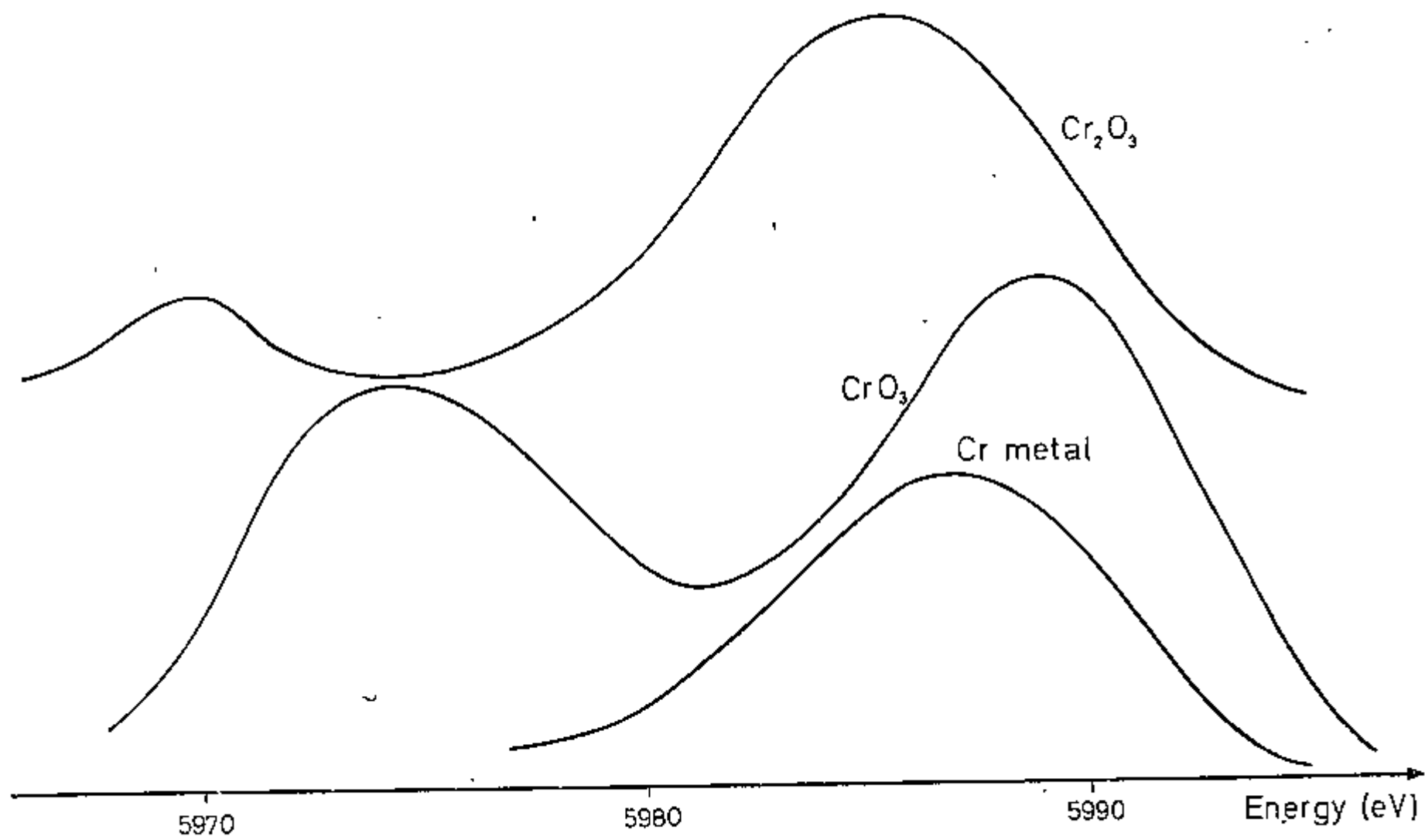


Figure III.1

$K\beta_{1,3}$  emission spectra for different chromium compounds

K $\beta_{2,5}$  emission bands for different chromium compounds

Figure III.2



UNIVERSITY OF TORONTO



In Figure III.1 the  $K\beta_{1,3}$  emission spectrum for the chromium metal is depicted. Similar spectra for compounds in which the chromium appears with oxidation states +3 and +6 may be seen in the same figure. We can observe the presence of a satellite peak on the low-energy side of the main peak, the so called  $K\beta'$ , whose origin will be investigated later in this chapter. In Figure III.2 the  $K\beta_{2,5}$  emission band region for the same set of chromium compounds are shown. On the high-energy side of the  $K\beta_{1,3}$  peak the  $K\beta_{2,5}$  region can also be seen, reflecting the electronic transition  $4p \rightarrow 1s$ , whose origin and characteristics will be investigated in the present chapter, as well.

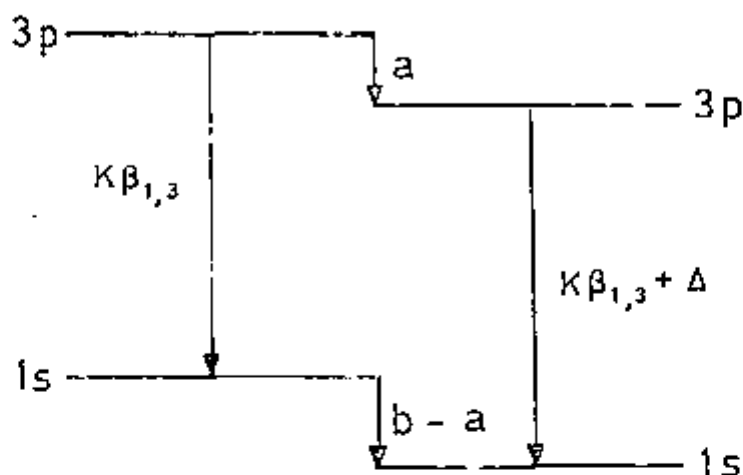
### III.2 The $K\beta_{1,3}$ Peak

#### III.2.1 Shifts in the $K\beta_{1,3}$ Main Peak Energies

X-ray emission spectra are known to be influenced by chemical states of X-ray emitting atoms. The effects of chemical states, however, are very small and difficult to quantify.

Since the characteristic energy of an emission line supplies the difference in energy between two ionized states of the same atom or molecule, experimental peak shifts do not lead to any conclusion concerning the degree or direction of the binding energy shifts of the individual levels. X-ray data must therefore be combined with the result observed by means of photoelectron spectroscopy, which supplies the exact values of the binding energies of the individual levels. If the electrons of the 3p and 1s

levels were both considered as true core electrons, we should expect a shift in the XPS spectra (a and b, respectively, in Figure III.3), due to a charge variation in the valence band, of about the same order of magnitude.



$$\Delta = b - a = \text{shift in the X-ray emission line}$$

Figure III.3

Shift in an X-ray emission line due to variation in the valence band charge

The shift in the corresponding X-ray emission line is the difference between a and b. Since these values are approximately the same (of the order of a few volts), it results that the change in the X-ray emission energy should be of the order of one tenth of the changes in the corresponding inner-orbital ionization energies. The division into core and non-core electrons for some elements, however, is not so obvious, e.g., the 3p and 3s electrons in first-row transition metal compounds. Several authors investigating the chemical shifts in transition metal complexes concluded that the 3p orbital cannot be classified

as a "deep" core level (Johansson et al, 1974; Politzer et al, 1973). Thus, for a first-row transition element, a decrease in the number of 3d electrons, associated with a change in the valence state will affect the binding force of the true core electrons and the "near valence band" core electrons in a different way. The 3p level will therefore be subjected not only to the shift in the binding energy, but also to chemical interactions with the partially filled 3d orbital.

#### III.2.1.1 Chromium Compounds

Although the total  $K\beta$  emission spectrum for the chromium compounds spreads over a range 20 eV wide (see Figure III.1), we shall firstly consider the influence of the oxidation state of the X-ray emitting atom in the energy of the  $K\beta_{1,3}$  main peak. Later in this chapter, after having examined the origin of the  $K\beta'$  low-energy satellite peak, we shall tackle the same problem by considering the shifts which occur in the total  $K\beta_{1,3} + K\beta'$  emission spectrum. The chromium  $K\beta_{1,3}$  peak positions for a number of compounds were recorded relatively to the corresponding metal. The results are summarized in Table III.1. These data reveal that the energy shifts for the  $K\beta_{1,3}$  peak depend upon the chemical state, especially upon the oxidation number of the X-ray emitting atom. Although the range of values within the trivalent and hexavalent states is quite large, the energy separation between different oxidation states is big enough to be used for the classification of the chromium oxidation state in the compounds.

COMPOUND	OXIDTN. NUMBER	*	K $\beta_{1,3}$ SHIFT (eV)	K $\alpha_1$ SHIFT (eV)	BINDING ENERGY (eV)	
					3p	2p $_{3/2}$
CHROMIUM METAL	0	-	0.0	0.0	41.4	573.8
CHROMIUM (III) CHLORIDE	+3	n	+0.9	+0.3	-----	-----
POTASSIUM HEXATHIOCYANATO CHROMIUM (III)	+3	m	+0.7	+0.1	44.8	578.2
TRIETHYLENEDIAMINE CHROMIUM (III) CHLORIDE	+3	m	+0.7	+0.1	42.8	575.8
CHROMIUM (III) SULPHATE	+3	f	+0.6	+0.2	43.9	576.8
HEXAUREACHROMIUM (III) CHLORIDE	+3	l	+0.5	+0.2	44.1	576.9
POTASSIUM TRIOXALATO CHROMIUM (III)	+3	e	+0.4	+0.1	43.9	577.0
ACETYLACETONATO CHROMIUM (III)	+3	e	+0.4	+0.3	43.0	575.8
CHROMIUM (III) OXIDE	+3	e	+0.4	+0.1	42.6	575.4
CHROMIUM (IV) OXIDE	+4	k	+0.4	+0.1	42.9	575.8
CHROMIUM (VI) OXIDE	+6	h	-0.4	-0.2	46.3	578.6
POTASSIUM DICHROMATE	+6	i	-0.7	-0.6	46.9	579.6
SODIUM & POTASSIUM CHROMATES	+6	j	-1.0	-0.5	46.6	578.7

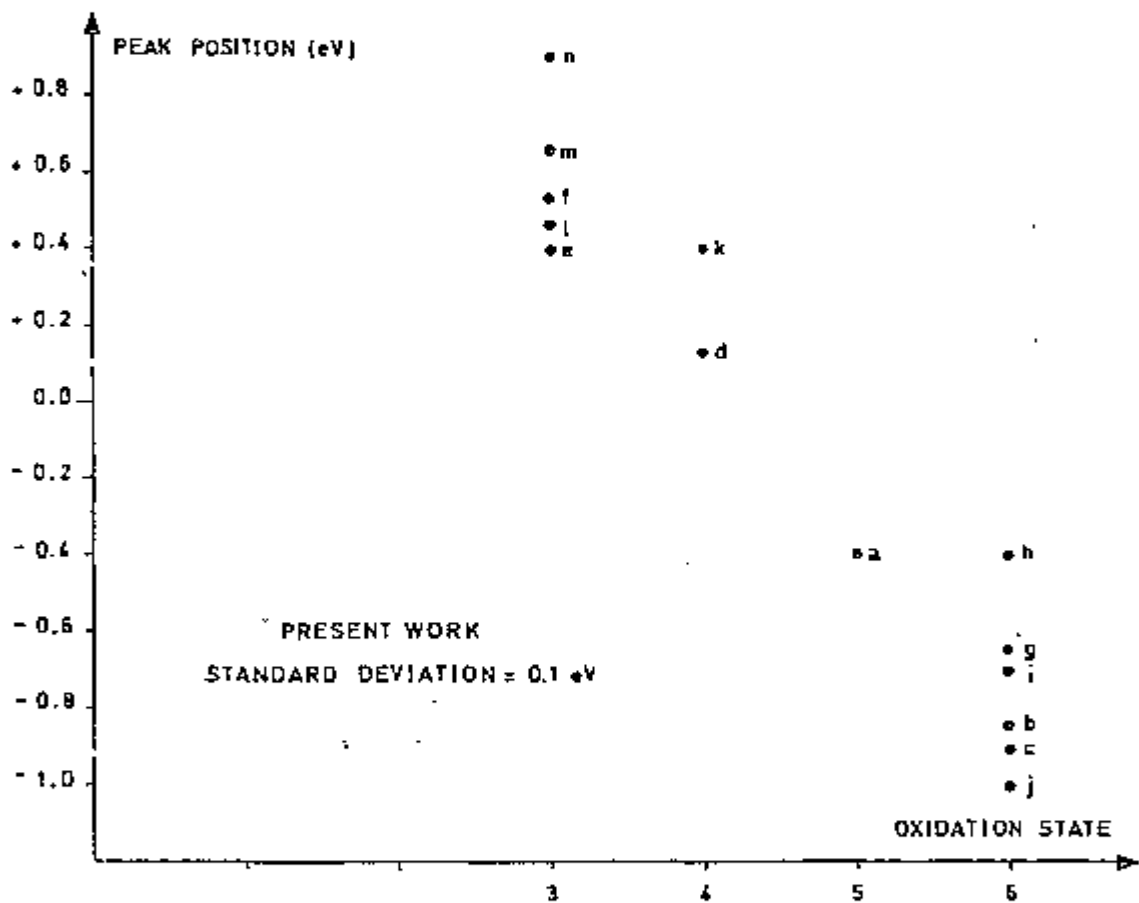
Table III.1

Chromium K $\beta_{1,3}$  and K $\alpha_1$  peak positionsChromium 2p $_{3/2}$  and 3p binding energies derived from XPS

\* Key for Figure III.4

The phenomenon of the dependence between the chromium oxidation state and the  $K\beta_{1,3}$  peak position was indeed used by Gohshi et al (1973) for the determination of the chemical state of chromium and manganese in inorganic pigments, and chromium and tin in glass.

In Figure III.4 the experimental results obtained by Gohshi et al (1973) are compared with those obtained in the present work.



Key for Gohshi's compounds :

a - $Cr_2O_5$	c - $K_2CrO_4$	e - $Cr_2O_3$	f - $CrCl_3$
b - $K_2Cr_2O_7$	d - $CrO_2$	h - $BaCrO_4$	g - $CaCrO_4$

Key for the results of the present work : see Table III.1

Figure III.4

Chromium  $K\beta_{1,3}$  peak position versus oxidation state

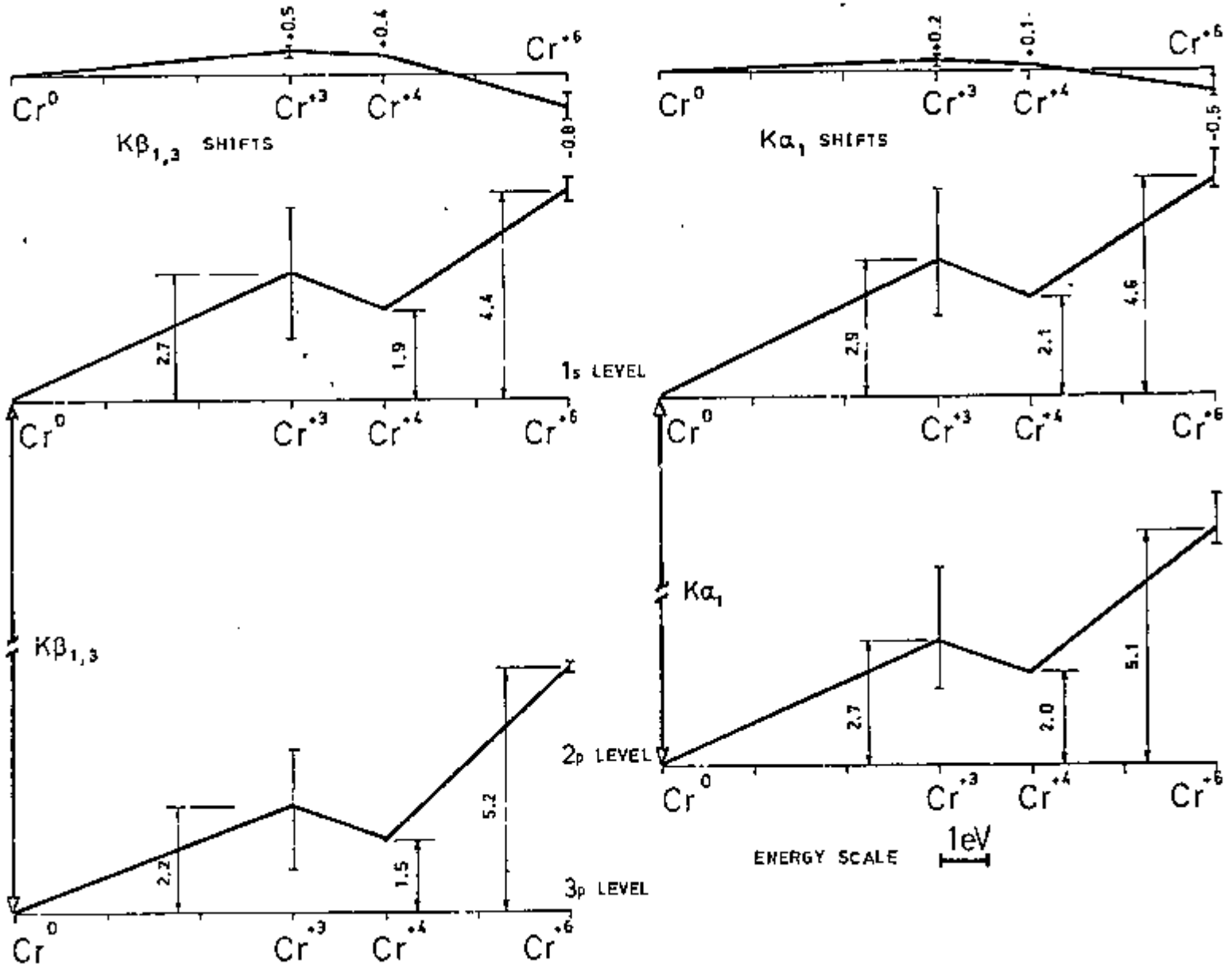
As the  $M_{II}$ ,  $M_{III}$  and K levels containing the 3p and 1s electrons are completely filled, the shifts in the  $K\beta_{1,3}$  allow general conclusions to be drawn as to the influence of the valence of the metal ion or to the change in the covalent character of the chemical bond. In the chromium compounds we notice a  $K\beta_{1,3}$  shift to lower energy values, as one goes from  $Cr_2O_3$  ( $Cr^{3+}$ ) to  $CrO_2$  ( $Cr^{4+}$ ) and to  $CrO_4^{2-}$  ( $Cr^{6+}$ ), that is, as we increase the covalent character of the metal in the compound.

If we want to estimate from the experimental results the degree of shifts of the levels involved in the  $K\beta_{1,3}$  transition (that is, 3p and 1s), we shall have to consider the Cr 3p binding energies, as well. These values, derived from the X-ray photoelectron spectra, were obtained by using the energy of the C 1s peak present in the form of surface contamination in all the studied compounds as a calibration reference. They are shown in Table III.1. The 1s level binding energy can be obtained by direct summation of the  $K\beta_{1,3}$  and 3p binding energies.

It is now possible to estimate from the experimental results the energy shifts of the levels involved in the  $K\beta_{1,3}$  transition, and draw an energy level diagram (see Figure III.5). We conclude that the 3p level is shifting to higher energy values, as one goes from Cr(IV) to Cr(VI) more quickly than the 1s level is, the  $M_{II}$ ,  $M_{III}$  and K levels being shifted towards one another. Still from Figure III.5, it is seen that the energy shifts in the 1s level are more pronounced than the corresponding ones in the 3p level, as one goes from Cr metal to Cr(IV).

Energy level diagram for the Cr  $K\beta_{1,3}$  and  $K\alpha_1$  lines

Figure III.5



In principle, one could expect a monotonic increase in the binding energies, both in the 1s and 3p levels. This general pattern is somewhat perturbed in the region from Cr(III) to Cr(IV), where the  $K\beta'$  satellite line may be influencing more strongly the  $K\beta_{1,3}$  peak energies (see section III.2.3).

The fact that similar shifts were also observed in the  $K\alpha_1$  emission lines (see Table III.1 and Figure III.5) allows us to conclude that not only chemical bonding affects the binding energy of core electrons, but also that different core levels are influenced to different degrees.

A more detailed analysis of Table III.1 suggests that there is also a correlation between the energy of  $K\beta_{1,3}$  and the electronegativity of the ligand. For the trivalent chromium compounds, for instance, we observe a shift towards higher energies when the ligand atom oxygen is substituted by chlorine.

This behaviour can be explained if it is assumed that the Cr(III) - O bond is more ionic than the Cr - Cl bond, and that the effect of the charge on the chromium atom is greater for the 3p than for the 1s level. Thus, for the more ionic compound the 3p level will be more tightly bound and so the 3p - 1s energy difference (and hence the  $K\beta_{1,3}$  energy) will be less than for the more covalent compound, i.e.,  $K\beta_{1,3}$  should be less for Cr(III) - O compounds than for Cr(III) - Cl compounds.



### III.2.1.2 Vanadium and Titanium Compounds

Analogous studies to that of section III.2.1.1 (relative to chromium compounds) have also been performed for vanadium and titanium compounds. The relevant results are summarized in Table III.2 and depicted in Figure III.6.

Here, the general trend shows a negative  $K\beta_{1,3}$  shift, as one goes from the metallic to the more oxidized states. Actually, this can be explained by the fact that the 3p binding energies are increasing more rapidly than those of the 1s level (see Figure III.6). Although the energy variations for the titanium compounds are rather small (practically within the experimental errors), it is observed that the  $K\beta'$  satellite line influence on the peak energies does not seem to be relevant (in section III.2.2.1 a detailed study of the  $K\beta'$  peak is presented). This can be understood from the smaller number of available 3d electrons, in comparison with the chromium and vanadium compounds.

Similar study for the  $K\alpha$  peaks was not pursued, since the energy shifts were in these cases so small that they could not be detected experimentally.

COMPOUND	OXIDTN. NUMBER	$K\beta_{1,3}$ SHIFTS (eV)	3p BINDING ENERGIES (eV)
TITANIUM METAL	0	0.0	34.8
TITANIUM (III) FLUORIDE	+3	-0.3	35.2
TITANIUM (III) OXIDE	+3	-0.4	35.2
TITANIUM (IV) OXIDE	+4	-0.3	35.2
CALCIUM ORTHOTITANATE	+4	-0.4	35.6
BARIUM METATITANATE	+4	-0.9	35.4
METHYLMETATITANATE	+4	-0.2	35.4
TITANIUM CARBIDE	+4	-0.5	36.3
POTASSIUM HEXAFLUOROTITANIUM (IV)	+4	-0.4	34.8
CALCIUM METATITANATE	+4	-0.3	35.5
STRONTIUM METATITANATE	+4	-0.3	35.5
VANADIUM METAL	0	0.0	38.8
ACETYLACETONATOVANADIUM (III)	+3	-0.3	39.0
VANADIUM (III) FLUORIDE	+3	-0.1	40.6
VANADYL SULPHATE	+4	-0.1	40.3
VANADYL ACETYLACETONATE	+4	-0.6	39.8
VANADYL PHTHALOCYANINE	+4	-0.4	39.6
VANADIUM PENTOXIDE	+5	-0.4	41.5
AMMONIUM METAVANADATE	+5	-0.4	41.6

Table III.2

Titanium and vanadium  $K\beta_{1,3}$  peak positions and 3p binding energies

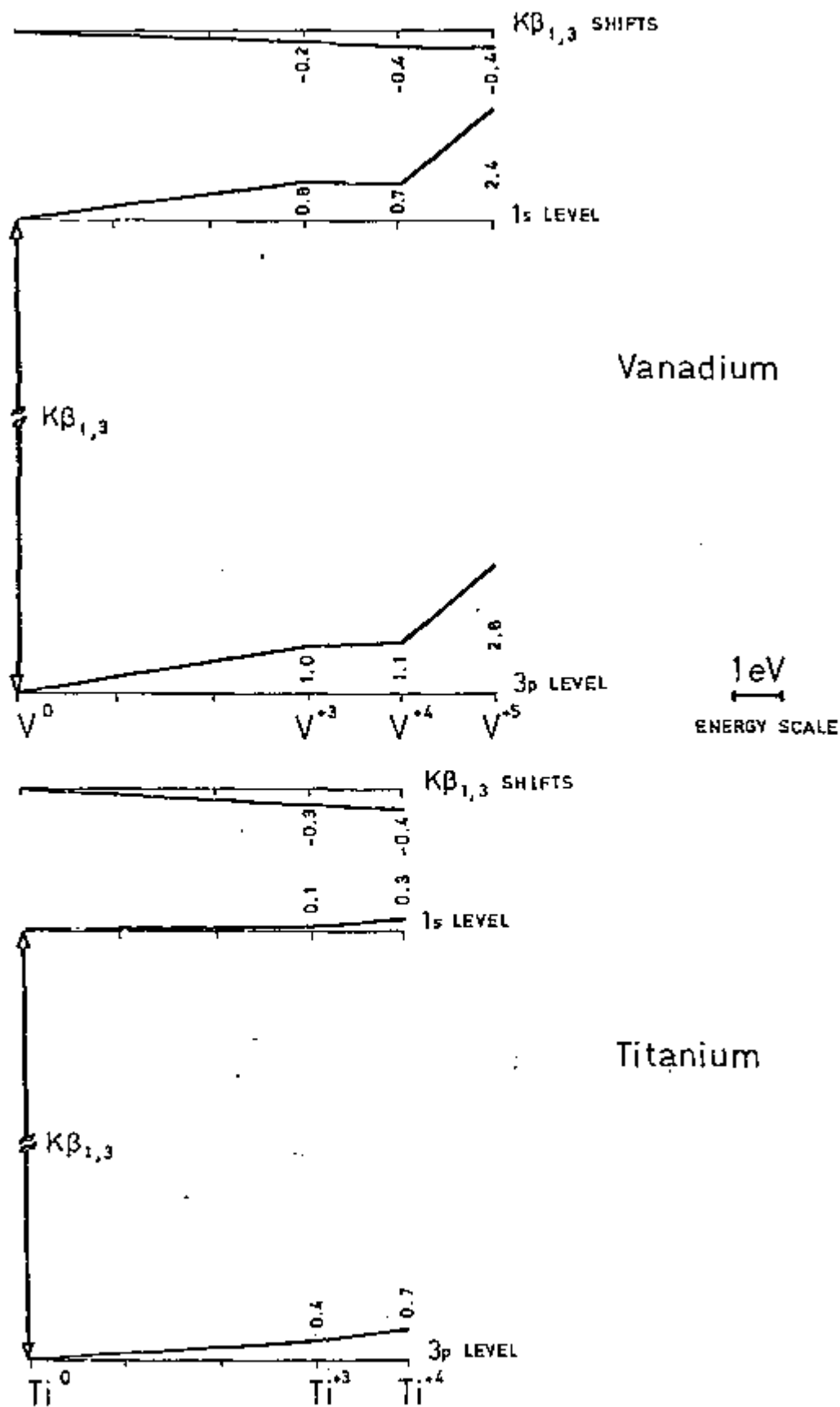


Figure III.6

Energy level diagram for Ti and V  $K\beta_{1,3}$

### III.2.2 Origin and Intensity of the Low-energy Satellite Peak $K\beta'$

In this section we shall be concerned with the origin of long wavelength satellites (named  $K\beta'$ ) which are observed in the X-ray emission spectra of compounds of the first-row transition metals. The  $K\beta'$  structure may appear as either a low-intensity peak or a widening of the main peak on the side of decreasing energies.

In Figure III.7 the  $K\beta_{1,3}$  emission line of a chromium (III) compound, together with the corresponding 3p photoelectron peak, is depicted. It is observed that the main XRES peak does line up with the 3p main XPS peak. The  $K\beta'$  peak also seems to have a correspondingly weak feature in the XPS spectrum, so that both spectra are dominated by final state effects. The main peak is more affected by this satellite line in the XRES than in the XPS mainly due to the difference in resolution achieved by the two techniques. Actually, the 3p photoelectron spectrum presents a FWHM of only 3 eV, whereas the FWHM is about 7.5 eV in the  $K\beta_{1,3}$  main X-ray emission peak.

When the sample is bombarded by a beam of X-rays, electrons in the K inner shell are removed causing a vacancy. This vacancy, according to the dipole atomic selection rule, may eventually be filled with any electron from the levels 2p, 3p, 4p, etc., accompanied by an X-ray emission characteristic of the atom. One can clearly realize that none of these transitions can be solely responsible for the  $K\beta'$  satellite line. Several attempts have been made in order to clarify the origin of such a non-diagram line.

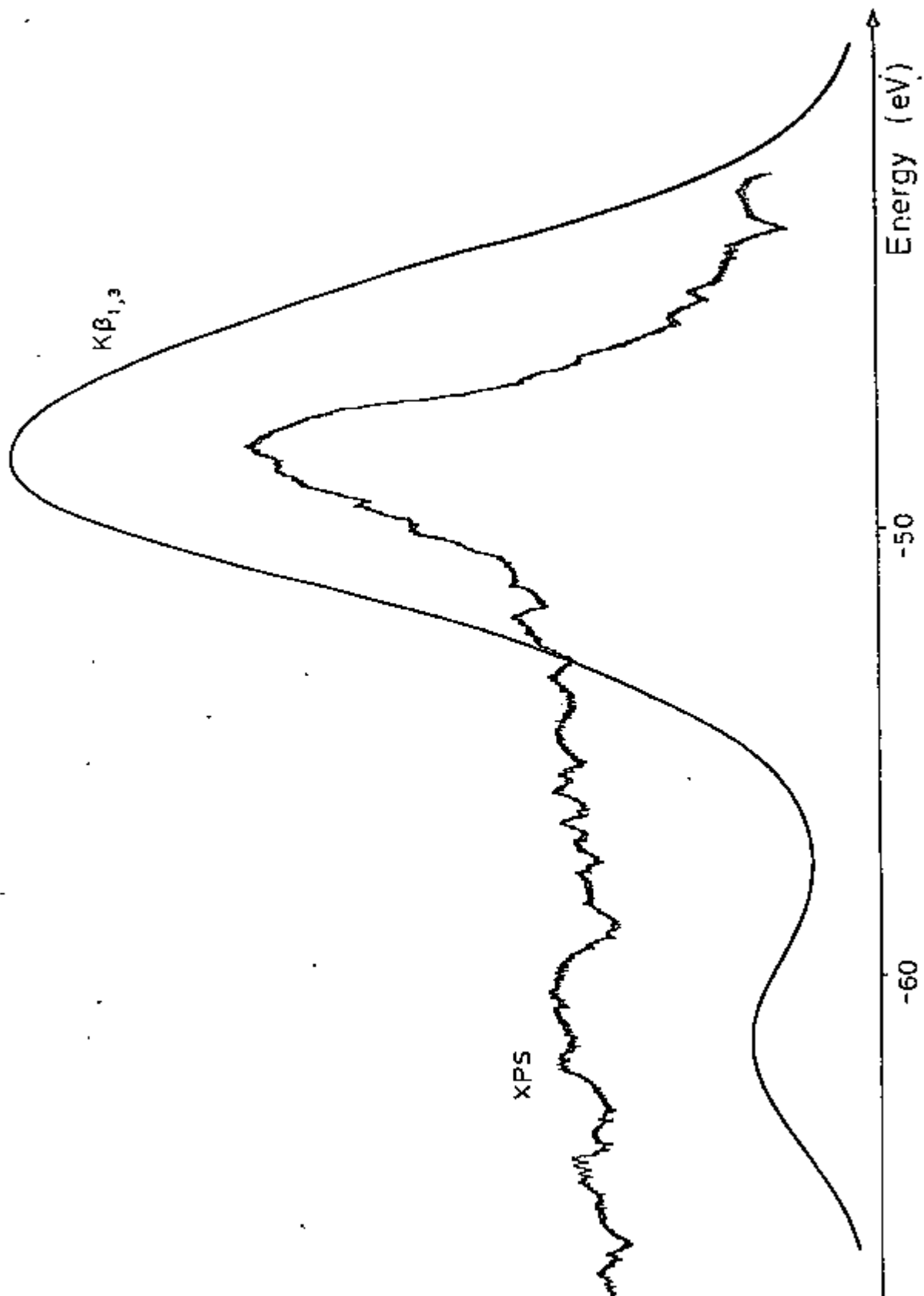


Figure III.7

$\text{K}\beta_{1,3}$  X-ray emission and 3p photoelectron spectra for  $\text{Cr}_2\text{O}_3$

Rooke (1963) and Lukirskii et al (1964) interpreted the  $K\beta'$  peak as an attenuation of the principal line energy, due to successive plasmon excitations. This theory, however, was soon considered inadequate for the explanation of such a satellite line. One of the limitations of the theory was that it did not explain the variations of the  $K\beta'$  intensity with the valence state of the emitting atom or with the type of ligand present in the molecule. The fact that no such a satellite was observed in the  $K\alpha$  line of the studied transition metal compounds also leads to the rejection of the plasmon excitation theory. After all, it would be rather curious that this phenomenon should be confined to particular emission lines of the X-ray emitting atom, or that it should depend upon the type of ligand present in the molecule. A chemical explanation for the origin of such low-energy satellites would therefore be more reasonable than the plasmon theory.

Two main proposals have been made in order to explain the "chemical effects" responsible for the origin of  $K\beta'$ . The first suggests that the peak splitting is associated with exchange coupling between the unpaired electrons in the final  $3p^5$  state and unpaired electrons in the  $3d$  shell (Slater et al, 1973; Tsutsumi et al, 1968). The second one explains the  $K\beta'$  origin as a result of a discrete loss process affecting the  $K\beta_{1,3}$  photon (Koster & Mendel, 1970). These topics will be discussed in more detail in the next section, where the experimental results obtained in this research will also be presented. We shall see that neither model is completely satisfactory, so that they cannot completely clarify the physical process involving the

formation of  $K\beta'$ .

### III.2.2.1 Emission Line Intensities

First-row transition metals have the d orbital partially filled. In the case of the chromium compounds, for which especial attention will be given in this section, the electronic configuration will be  $[K][L] 3s^2 3p^6 3d^x$ . The value given to x can vary from zero to 3, according to the oxidation state of the chromium (from +6 to +3, respectively) present in the sample. As a result of the presence of unpaired electrons in the 3d orbitals, the compounds of such elements are generally paramagnetic, due to the spin angular momentum associated to the electrons of this orbital. As the oxidation number of these elements in their various compounds is governed by the number of existing electrons in the d orbital, one concludes that most of the physical and chemical properties of these compounds may be understood in terms of the 3d shell.

Table III.3 shows the results obtained for the  $K\beta'$  intensity as a function of the oxidation state of the emitting atom for several chromium compounds. Similar results for the vanadium compounds are summarized in Table III.4. For the titanium compounds, as a whole, the  $K\beta'$  relative intensity was found to be practically constant (around 8%). The intensity of the  $K\beta'$  peak was expressed by means of the ratio  $(100 IK\beta'/IK\beta_{1,3})$ , where  $IK\beta'$  is the height of the  $K\beta'$  satellite peak and  $IK\beta_{1,3}$  is the height of the  $K\beta_{1,3}$  main peak. In some cases, however, it was almost impossible to discern clearly  $IK\beta'$ , since the satellite peak

was not completely resolved, it appearing as a tail on the lower energy side of  $K\beta_{1,3}$ . In order to overcome this difficulty, the intensity of  $K\beta'$  was considered as being the count rate at a point situated 12 eV to 14 eV apart from the  $K\beta_{1,3}$  main peak (on the lower energy side), depending on the oxidation number of the transition metal, as suggested from the analysis of the deconvoluted spectra (see Figure III.8). Indeed, for the chromium compounds it was found, as an average, that the  $K\beta_{1,3} - K\beta'$  energy separations are :

- for metallic chromium, -12 eV;
- for Cr(III) compounds, -14 eV;
- for Cr(IV) compounds, -14 eV;
- for Cr(VI) compounds, -13 eV.

On the other hand, only a minor variation was found to occur for the  $K\beta_{1,3} - K\beta'$  energy separation for the vanadium compounds, so that it was assumed for them a mean value of -14 eV.

In both measurements, that is,  $IK\beta_{1,3}$  and  $IK\beta'$ , the background level was considered as being the same, and it was taken as the count rate at a point far away from the peak region.

We observe from the results of Table III.3 that the  $K\beta'$  intensity varies with the chromium oxidation state, increasing as the oxidation number decreases. Although the same consideration is also valid for the vanadium compounds (Table III.4), a much smaller variation is observed here.



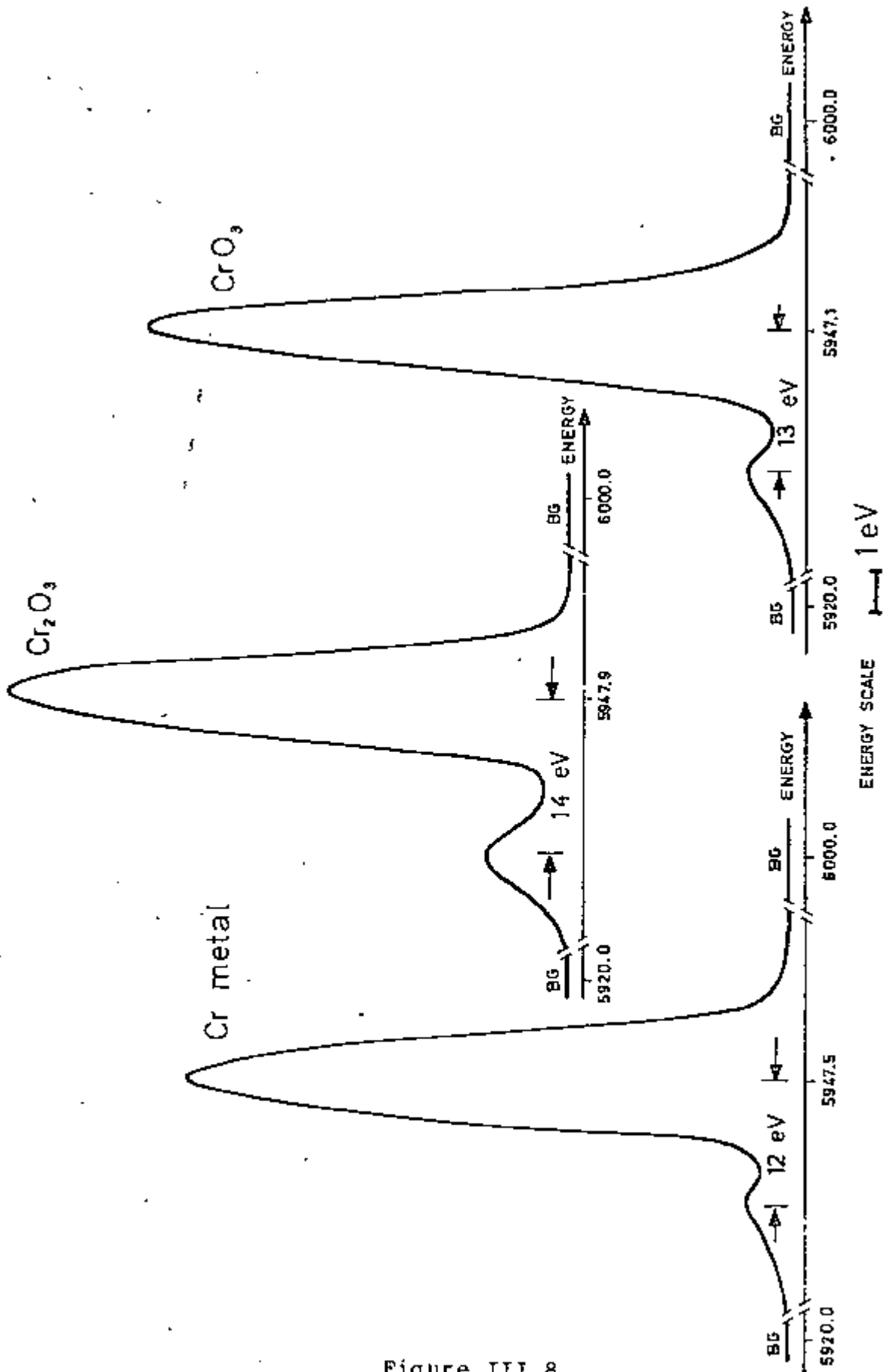


Figure III.8

Energy separation between  $K\beta_{1,3}$  and  $K\beta'$   
for different chromium compounds

COMPOUND	OXIDTN.	K $\beta$ '
	NUMBER	INTENSITY
		8
CHROMIUM METAL	0	19
CHROMIUM (III) OXIDE	+3	23
ACETYLACETONATOCHROMIUM (III)	+3	24
TRIETHYLENEDIAMINECHROMIUM (III) CHLORIDE	+3	25
POTASSIUM TRIOXALATOCHROMIUM (III)	+3	23
HEXAUREACHROMIUM (III) CHLORIDE	+3	23
CHROMIUM (III) SULPHATE	+3	23
POTASSIUM HEXATHIOCYANATOCHROMIUM (III)	+3	23
CHROMIUM (III) CHLORIDE	+3	24
CHROMIUM (IV) OXIDE	+4	22
CHROMIUM (VI) OXIDE	+6	17
SODIUM CHROMATE	+6	16
POTASSIUM CHROMATE	+6	16
LEAD CHROMATE	+6	18
POTASSIUM DICHROMATE	+6	16

Table III.3

Chromium K $\beta$ ' intensity as a function of the oxidation state  
of the emitting atom

COMPOUND	OXIDTN. NUMBER	K $\beta$ ' INTENSITY %
VANADIUM METAL	0	13
ACETYLACETONATOVANADIUM (III)	+3	13
VANADIUM (III) FLUORIDE	+3	13
VANADIUM (III) OXIDE	+3	14
VANADYL SULPHATE	+4	13
VANADYL ACETYLACETONATE	+4	13
VANADYL PHTHALOCYANINE	+4	13
AMMONIUM METAVANADATE	+5	10
VANADIUM PENTOXIDE	+5	10

Table III.4

Vanadium K $\beta$ ' intensity as a function of the oxidation state of the emitting atom

Indeed, in this case the number of available electrons in the 3d orbital is less than for chromium (3d population varies from 0 to 2, as the vanadium oxidation state decreases from +5 to +3). It is therefore expected that any interaction between these electrons with unpaired 3p electrons should be less intense.

(a) The spin-only exchange model

According to Tsutsumi (1959), electronic interactions may occur between the 3p<sup>5</sup> and 3d uncoupled electrons, due to a coupling of the respective spin angular momenta, producing multiple final states. The two final states would then give rise to the two existing emission lines K $\beta$ ' and K $\beta_{1,2}$ . In

other words,  $K\beta_{1,3}$  and  $K\beta'$  lines are emitted due to transitions from the states having the total spins equal to  $s + 1/2$  and  $s - 1/2$ , respectively, where  $s$  is the total spin of the partially filled 3d shell and  $1/2$  is that of the partially filled 3p shell in the final state. The separation in energy between the  $K\beta_{1,3}$  and  $K\beta'$  lines will therefore be similar to the difference between the exchange energies for  $s + 1/2$  and  $s - 1/2$ .

Although this proposal is quite simple, involving exclusively the idea of the coupling of the spin angular momenta of uncoupled electrons, it is by itself sufficient to invalidate Rooke and Lukirskii's statements that the only explanation for the origin of  $K\beta'$  would be the plasmon excitation. Yet, it is seen that the spin coupling hypothesis of Tsutsumi (1959) presents limitations, so that it cannot be taken as the only physical process responsible for the origin of  $K\beta'$ . Problems arise, anyway, when one attempts to relate the experimental results collected for the  $K\beta'$  relative intensity to the theoretical predictions of Tsutsumi. According to his theoretical calculations, based on the multiplicity of the two possible final states of the ion, the relative intensity for a chromium (III) compound (configuration  $d^3$ ) should be  $I_{K\beta'}/I_{K\beta_{1,3}} = 0.60$ . The experimental values of the relative intensity for such compounds ( $\sim 0.24$ ) are actually much lower than the one resulting only from the exchange coupling model. We shall come back to this point in section (c), where a more sophisticated model is presented.

(b) Attenuation of the main  $K\beta_{1,3}$  peak due to successive electronic excitations

Koster and Mendel (1970) proposed that the main  $K\beta_{1,3}$  X-ray photon is attenuated by specific electronic excitation processes involving the 3d electrons, that is, the X-ray analogue of "shake-up". The changes in intensity of  $K\beta'$  with valence would then be simply due to the increased probability of attenuation caused by an increase in the number of d electrons. In other words, the formation of  $K\beta'$  was thought to be due to promotion of 3d electrons to the conduction band. The energy for this transition was supplied by the self-absorption of part of the  $K\beta_{1,3}$  quantum, whose energy was accordingly decreased by the same amount. The presence of the low-energy tail on the  $K\beta_{1,3}$  line for chromium (VI) compounds, whose configuration is  $d^0$  cannot be explained by the simple exchange model. Actually, the absence of electrons in the 3d orbital would dismiss any possibility of multiplet effects. According to the theory of Koster and Mendel (1970), however, in such a case the  $3p \rightarrow 1s$  transition would be accompanied by the excitation of a valence electron to a vacant shell, giving rise to a shake-up satellite.

(c) The spin-orbit coupling model

More refined models, however, emerge when the spin-orbit coupling is taken into account. Fadley et al (1970) analysed the splittings in the several compounds showing the 3d orbital partially filled. According to them, these splittings are due to the various possible multiplet states

formed by coupling a hole in a metal atom subshell to an unfilled valence shell. In this case, the orbital angular momentum of the 3p electron permits several possible L - S couplings within the  $3p^5 3d^x$  final state configuration.

Results collected by Faddley et al (1970) and by Ekstig et al (1970) indicate that the spectrum obtained in practice is more complex than the two peaks foreseen by the simple electronic spin coupling. Even in the case in which the spectrum may be divided into two peaks, the intensity of the second one will be much weaker than the expected by applying the spin-orbit model. The  $K\beta'$  relative intensity obtained by Ekstig et al (1970) for a  $d^3$  compound, 0.43, is indeed smaller than the calculated value of Tsutsumi (1959), 0.60. Ekstig's result would be further reduced to 0.33, if the configuration effect was taken into account in the spin-orbit coupling method. Of course, all these calculations were carried out considering only free atoms or ions. It is not therefore surprising that they are not in good agreement with the experimental results, where we should expect a large chemical combination effect.

Slater and Urch (1972), studying the  $K\beta'$  region for several iron compounds, observed a prominent  $K\beta'$  peak for high-spin ferrous and ferric compounds, whilst no such a peak was seen for the low-spin cyanide complexes. The origin of  $K\beta'$  would then be connected with the population of unpaired electrons of the 3d orbital. Iron can appear in two different oxidation states ( $Fe^{2+}$ , whose configuration is  $d^6$ , and  $Fe^{3+}$ , whose configuration is  $d^5$ ). When the iron atom is surrounded by "weak ligands", its orbitals will receive very

little influence of the outer orbitals of the ligand atom. In such a case, the principle of maximum multiplicity will prevail (Hund's rule). We shall thus have a total number of 4 uncoupled electrons for the  $\text{Fe}^{2+}$  cation and 5 in the case of the  $\text{Fe}^{3+}$  cation. On the other hand, when the ligand is "strong", the d orbitals will no more be degenerate, but will be unfolded into two energy levels. For molecules with octahedral spacial orientation, the  $t_{2g}$  symmetry orbitals will be more tightly bound, whereas those of  $e_g$  symmetry will be less tightly bound. Therefore, the  $\text{Fe}^{3+}$  complexes will have a single unpaired electron, whilst in the  $\text{Fe}^{2+}$  complexes all electrons will be coupled. The results obtained by Slater and Urch (1972) - see Table III.5 - clearly illustrate this behaviour.

SAMPLE	NUMBER OF UNPAIRED 3d ELECTRONS	$K\beta'/K\beta_{1,3}$ INTENSITY RATIO %	TYPE OF LIGAND
$\text{Fe}_2\text{O}_3$	5	30	weak
$\text{Fe}_2(\text{SO}_4)_3$	5	30	weak
$\text{K}_3\text{Fe}(\text{C}_2\text{O}_4)_3$	5	25	weak
$\text{Fe}^{\text{II}}$ alum	4	22	weak
$\text{Fe}^{\text{III}}$ alum	4	28	weak
$\text{K}_4\text{Fe}(\text{CN})_6$	0	<5	strong
$\text{K}_3\text{Fe}(\text{CN})_6$	1	<5	strong

Table III.5

$K\beta'/K\beta_{1,3}$  intensity ratio (%) for some iron compounds as a function of the number of 3d unpaired electrons  
(from Slater and Urch, 1972)

In conclusion, one can say that changes occur in the  $K\beta$  X-ray emission spectrum which are due to variations in the emitting atom oxidation state, that is, in the population of the 3d orbital. The experimental results obtained here show that the electronic interaction forming multiple final states is the most adequate explanation for the origin of  $K\beta'$ . Indeed, for this hypothesis, theoretical predictions and experimental results are in better agreement. The spin-only exchange model does not seem completely suitable because the  $K\beta'$  satellite intensity predicted by this model is roughly the triple of the experimental results obtained. The origin of the  $K\beta'$  line seems to be more related to the multiplicity of the metallic ion itself than to its formal oxidation state. Of course, effects such as configuration interaction must also be taken into consideration to account for  $d^0$  compounds which present some emission in the  $K\beta'$  region.

### III.2.3 Shifts in the $K\beta_{1,3} + K\beta'$ Emission Spectrum Energies

In this section we shall be concerned with the shifts which occur in the total  $K\beta_{1,3} + K\beta'$  spectrum for the chromium compounds. As discussed in the previous section, the relative intensity of the  $K\beta'$  satellite peak varies with the oxidation state of the central atom. We should therefore expect a displacement in the centre of gravity of the system. This displacement has to be taken into account in the study of the shift in the  $K\beta$  emission spectrum as a whole. The corrected energy value ( $E_{corr}$ ) was evaluated as



follows :

$$E_{\text{corr}} = \frac{EK\beta' \cdot r + EK\beta_{1,3}}{1 + r} \quad (\text{III.1})$$

where :  $r = IK\beta' / IK\beta_{1,3}$  ;

$EK\beta'$  and  $EK\beta_{1,3}$  are the experimental energies of the  $K\beta'$  and  $K\beta_{1,3}$  peaks, respectively.

We now recast the same problem of section III.2.1.1, namely that of the determination of energy shifts, as shown in Table III.6.

OXIDTN. NUMBER	r (AVERAGE)	$EK\beta_{1,3}$ (AVERAGE)	$EK\beta'$ (AVERAGE)	$E_{\text{corr}}$ (AVERAGE)	SHIFTS (AVERAGE)
0	0.19	5947.5	5935.5	5945.6	0.0
+3	0.23	5948.1	5934.1	5945.4	-0.2
+4	0.22	5947.9	5933.9	5945.4	-0.2
+6	0.17	5946.8	5933.8	5945.0	-0.6

Table III.6

Influence of  $K\beta'$  on the  $K\beta$  emission spectrum shifts

It is now seen that all the shifts occur to the lower-energy side with respect to the metallic chromium, and their absolute values increase with the increasing of the oxidation state.

Although the above explanation concerning the influence of the satellite line ( $K\beta'$ ) implies in a different trend for the  $K\beta_{1,3}$  energy shifts, it cannot be used for the  $K\alpha$  shifts (see Figure III.5), for the simple reason that the very small effect of such a non-diagram line was completely lost in the experimental results. Calculations carried out by Demekhin et al (1974) for iron compounds, however, show that a weak satellite line really exists on the low-energy side of the  $K\alpha_{1,2}$  doublet.

### III.3 High-energy Satellite Lines : the $K\beta_{2,5}$ Region

#### III.3.1 Introduction and Experimental Results

On the side of higher energy of the  $K\beta_{1,3}$  main peak one normally finds the so called  $K\beta_{2,5}$  region (see Figure III.2). The peaks present in this region have their origin in the electronic transition  $4p \rightarrow 1s$ . Such X-ray emission lines are, therefore, connected with transitions directly related to the valence band. The relative intensity and position of these satellite lines vary with the type of ligand and oxidation state of the metal atom. In general, these satellite lines for the transition metal compounds consist of two peaks, in order of increasing energy  $K\beta'' < K\beta_{2,5}$ .

The first researchers who analysed the  $K\beta_{2,5}$  line attributed it to the  $3d \rightarrow 1s$  transition (Idei, 1929). Indeed, the calculated binding energy difference ( $3p - 3d$ ) was very close to the transition energy gap between the peaks  $K\beta_{1,3}$  and  $K\beta_{2,5}$ . The assumption which led the first

investigators to attribute the  $K\beta_{2,5}$  spectral line to the  $3d \rightarrow 1s$  transition, was based on the study of the "free atom". Yet, the electronic configuration of an element in the gaseous state cannot be considered equivalent to the electronic configuration for the solid state, especially regarding the outer shells near to the valence band. On the other hand, the X-ray emission spectra of isolated transition metal ions were never studied. The experimental results were collected for compounds in which the ions are bound to different elements. We should therefore expect the metal 4p to be involved in the bond.

According to the first explanations, the  $K\beta_{2,5}$  emission line would be associated with a quadrupole transition, because the  $3d \rightarrow 1s$  transition corresponds to a dipole-forbidden transition. Nevertheless, it is possible to verify from the experimental results that the  $K\beta_{2,5}$  intensity (relative to the  $K\beta_{1,3}$  main peak) for the transition metal compounds is stronger than the real  $K\beta_5$  peak for the remaining elements of the same row. The larger  $K\beta_{2,5}$  intensity for the transition metal compounds indicates that this emission band should not be explained in terms of a  $3d \rightarrow 1s$  quadrupole transition.

The origin of the  $K\beta_{2,5}$  and  $K\beta''$  transitions can be explained in a similar way to the  $K\beta_{1,3}$  and  $K\beta'$  peaks observed in the elements of the second main group. With that purpose, Urch (1970, 1971) studied the bond formed between second group elements and several ligands, such as oxygen and fluorine.

For the compounds of particular interest in this investigation, the transition metal ion is either octahedrally or tetrahedrally coordinated to the ligands. We shall not discuss here the bonding in both tetrahedral ( $ML_4$ ) and octahedral ( $ML_6$ ) units, since this topic will be presented in Chapter V. From the analysis of the molecular orbital diagrams, one observes that the only allowed transition for the  $1s$  level is the one which originates in  $t_2$  symmetry orbitals for  $ML_4$ , and  $t_{1u}$  for  $ML_6$  compounds.

In order to obtain results concerning to the energy and intensity of such peaks, the short wavelength profile of the  $K\beta_{1,3}$  main peak was subtracted from the corresponding  $K\beta_{2,5}$  and  $K\beta''$  intensities. In Figure III.9 this operation is shown for  $K_2CrO_4$ . The results obtained for the line intensities, for the energy gap between  $K\beta_{2,5}$  and  $K\beta''$  and for the  $K\beta_{2,5}$  energy shifts, are shown in Tables III.7 and III.8. In these tables the relative intensity of the  $K\beta_{2,5}$  spectral line was expressed as :  $(100 IK\beta_{2,5}/IK\beta_{1,3})$ , where  $IK\beta_{2,5}$  is the height of the  $K\beta_{2,5}$  peak and  $IK\beta_{1,3}$  is the height of the  $K\beta_{1,3}$  main peak. In the same way, the relative intensity of  $K\beta''$  was evaluated in terms of :  $(100 IK\beta''/IK\beta_{2,5})$ , where  $IK\beta''$  is the height of the  $K\beta''$  satellite peak.

For all the compounds studied, a  $K\beta_{2,5}$  peak was always observed with an intensity of between 1% and 4% of the  $K\beta_{1,3}$  main peak. The  $K\beta''$  satellite peak increased in intensity relative to  $K\beta_{2,5}$  with the oxidation state of the transition metal.

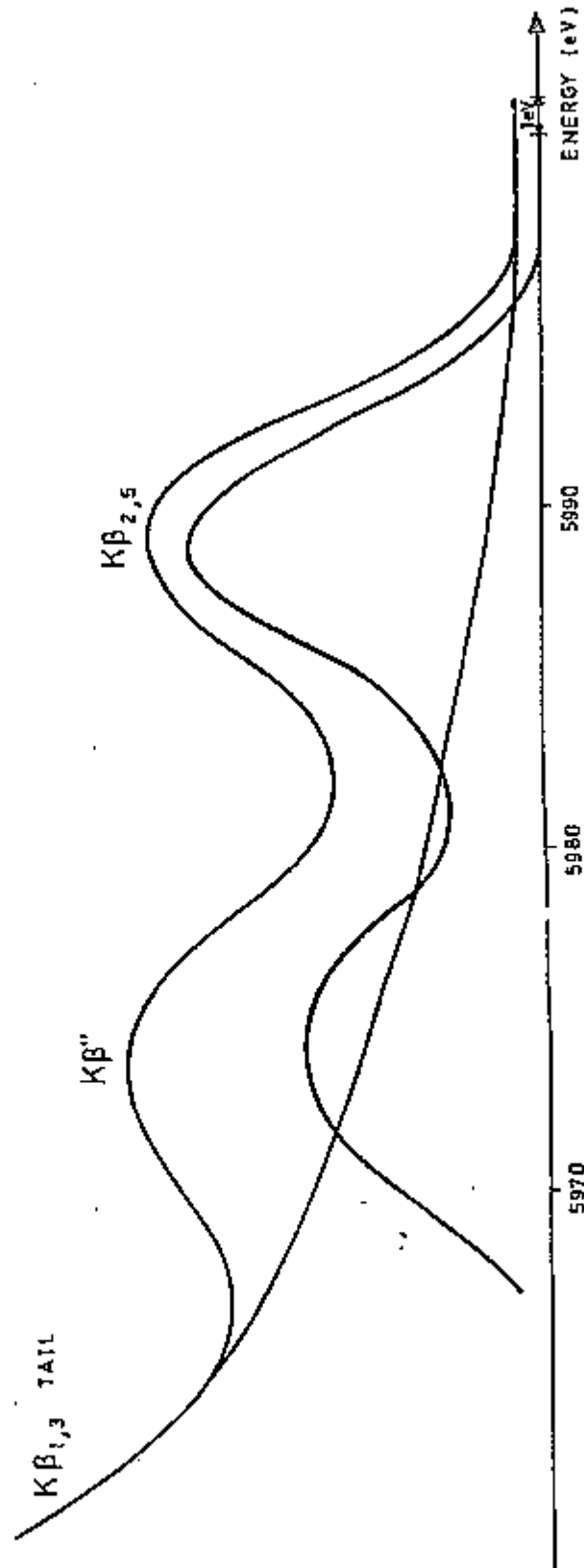


Figure III.9

$K\beta_{2,5}$  and  $K\beta''$  peaks for  $K_2CrO_4$   
after subtraction of the  $K\beta_{1,3}$  main peak tail

COMPOUND	OXIDTN. STATE	INTENSITY (%)		* $\Delta$ (eV)	$K\beta_{2,5}$ SHIFT (eV)
		$K\beta_{2,5}$	$K\beta''$		
CHROMIUM METAL	0	3.0	--	----	0.0
ACETYLACETONATO CHROMIUM (III)	+3	2.1	--	----	-3.2
HEXAUREACHROMIUM (III) CHLORIDE	+3	2.2	--	----	-3.7
CHROMIUM (III) SULPHATE	+3	2.1	--	----	-1.7
POTASSIUM TRIOXALATO CHROMIUM (III)	+3	2.2	11	15.5	-2.9
CHROMIUM (III) OXIDE	+3	2.1	18	14.6	-1.4
TRIETHYLENEDIAMINE CHROMIUM (III) CHLORIDE	+3	2.2	17	6.0	0.0
CHROMIUM (III) CLORIDE	+3	1.8	--	----	-1.7
CHROMIUM (IV) OXIDE	+4	2.5	20	14.0	-0.9
CHROMIUM (VI) OXIDE	+6	2.9	82	14.5	+1.9
LEAD CHROMATE	+6	3.0	77	14.5	+1.6
POTASSIUM DICHROMATE	+6	2.5	88	15.0	+1.5
SODIUM CHROMATE	+6	3.1	80	15.4	+2.6
POTASSIUM CHROMATE	+6	3.1	75	15.5	+2.2

Table III.7

Chromium  $K\beta_{2,5}$  and  $K\beta''$  emission line intensity and energy separation.  $K\beta_{2,5}$  energy shifts

\* ( $K\beta_{2,5}$  -  $K\beta''$ ) energy separation

COMPOUND	OXIDTN. STATE	INTENSITY (%)		* $\Delta$ (eV)	$K\beta_{2,5}$ SHIFT (eV)
		$K\beta_{2,5}$	$K\beta''$		
TITANIUM METAL	0	1.9	--	-----	0.0
TITANIUM (III) OXIDE	+3	2.5	--	-----	-5.0
TITANIUM (III) FLUORIDE	+3	3.3	--	-----	-2.0
TITANIUM CARBIDE	+4	3.0	54	7.0	-1.0
TITANIUM (IV) OXIDE	+4	3.2	64	15.0	-0.5
CALCIUM ORTHOTITANATE	+4	3.3	61	14.9	+0.5
CALCIUM METATITANATE	+4	3.7	75	15.1	+0.5
STRONTIUM METATITANATE	+4	3.6	67	14.1	+0.5
METHYL METATITANATE	+4	3.0	43	14.8	+0.5
POTASSIUM HEXAFLUORO TITANIUM (IV)	+4	4.5	64	21.0	+1.5
VANADIUM METAL	0	2.3	--	-----	0.0
ACETYLACETONATO VANADIUM (III)	+3	2.2	50	14.6	-2.0
VANADIUM (III) FLUORIDE	+3	2.5	--	-----	-2.5
VANADIUM (III) OXIDE	+3	2.9	41	15.2	-1.5
VANADYL SULPHATE	+4	2.6	58	14.3	-1.0
VANADYL ACETYLACETONATE	+4	2.1	57	14.3	-1.0
VANADYL PHTHALOCYANINE	+4	2.9	47	15.1	-0.5
AMMONIUM METAVANADATE	+5	3.7	72	15.4	+0.5
VANADIUM PENTOXIDE	+5	3.5	75	14.4	+0.5

Table III.8

Titanium and vanadium  $K\beta_{2,5}$  and  $K\beta''$  emission line intensity and energy separation.  $K\beta_{2,5}$  energy shifts

\* ( $K\beta_{2,5} - K\beta''$ ) energy separation

In  $ML_6$  compounds, the metal 4p orbital participates in sigma bonds, by overlapping with the ligand orbitals of same symmetry, i.e.,  $t_{1u}$ . One therefore realizes that the 2p and 2s ligand orbitals strongly interact with the 4p orbital, giving rise to the  $K\beta_{2,5}$  and  $K\beta''$  transitions. The higher energy peak  $K\beta_{2,5}$  is related to the electronic transitions from M with 4p character, and from L with 2p character. On the other hand, the lower energy peak ( $K\beta''$ ) is related to the electronic transitions from M with 4p character, and from L with 2s character.

In  $ML_4$  compounds, the existence of similar peaks may be understood in the same way. In this case, the metal 4p orbital will interact with the  $t_2$  symmetry orbitals of the ligand derived from 2p and 2s orbitals, giving rise to the same set of peaks.

### III.3.2 Changes in the $K\beta_{2,5}$ and $K\beta''$ Relative Intensities

It can be seen from Tables III.7 and III.8 that the  $K\beta_{2,5}$  relative intensity increases as the central atom oxidation state does so. This fact is not at all surprising because with the increase of the oxidation state, the 4p electrons will be more tightly bound (larger ionization energy) decreasing the gap between this orbital and the 2p orbital of the ligand atom. Consequently, there will be a larger influence of the 4p orbital in the  $t_2$  molecular orbital for tetrahedral configuration and  $t_{1u}$  for octahedral configuration, whose nature is predominately determined by the ligand 2p orbital, and therefore a greater amount of 4p character present in these orbitals. This will have the



effect of increasing the  $K\beta_{2,5}$  relative intensity with the central atom oxidation state.

The influence of the metal oxidation state in the studied compounds can also be seen in the intensity of the  $K\beta''$  line. For the compounds in which the metal has a higher oxidation state, the electrons will be more influenced by the nucleus positive charge and will be more tightly bound. All the electrons will therefore have a higher ionization energy, decreasing the separation between the 4p orbital of the metal and the 2s orbital of the ligand atom, thus favouring the overlap. For this reason, the lower energy peak ( $K\beta''$ ) becomes more intense as the metal oxidation state increases. Thus, the bonds to transition metal ions in high oxidation states will have pronounced covalent character.

### III.3.3 Energy Separation between $K\beta_{2,5}$ and $K\beta''$

The experimental results obtained in the present work, concerning the separation in energy ( $\Delta$ ) between  $K\beta_{2,5}$  and  $K\beta''$ , are shown in Tables III.7 and III.8. As the molecular orbitals formed by overlapping the metal 4p orbital with the ligand orbitals of same symmetry (i.e. 2p and 2s orbitals) are mainly influenced by the ligand orbitals, the  $K\beta_{2,5} - K\beta''$  difference in energy will be a function of the separation between the valence electrons of the ligand atoms, that is, the difference between the 2s and 2p binding energies. In Table III.9 the approximate atomic orbital ionization energies computed from the atomic spectra (Moore, 1949) can be seen.

ELEMENT	ATOMIC ORBITAL IONIZATION ENERGIES		
	ENERGIES (eV)		
	2s	2p	2s - 2p
C	16.6	11.2	5.4
N	20.4	14.4	6.0
O	28.4	13.6	14.8
F	37.8	17.4	20.4
	3s	3p	3s - 3p
S	20.2	10.4	9.8
Cl	24.6	13.0	11.6

Table III.9

Approximate atomic orbital ionization energies

The difference  $\Delta$  found for the compounds in which the ligand atoms are basically oxygen corresponds to the difference between the ionization energy of the 2p and 2s atomic orbitals of the ligand atom, it being approximately 15 eV. It is therefore clear that the molecular orbitals, which are responsible for the  $K\beta''$  and  $K\beta_{2,5}$  transitions, have predominantly oxygen 2s and oxygen 2p character, respectively. The same reasoning is also valid for compounds in which the ligand atoms are other than the oxygen. Potassium hexafluorotitanium (IV), for example, presents for  $\Delta$  a value of 21.0 eV, which is approximately equivalent to the difference between the ionization energies of the 2s and 2p atomic orbitals (20.4 eV) of the ligand atoms (fluorine). Titanium carbide presents  $\Delta$  equal to 7.0 eV. This value also agrees with the energy separation between

the 2s and 2p atomic orbital ionization energies for carbon (5.4 eV).

Best (1965, 1966) performed a series of measurements of the  $K\beta$  X-ray emission spectra from the metal atoms in  $MnO_4^-$ ,  $CrO_4^{2-}$  and  $VO_4^{3-}$  ions. The observed emission lines were attributed to transitions from the  $3t_2$  (metal 3p), the  $4t_2$  (oxygen 2s) and the valence  $6t_2$  (predominantly oxygen 2p) orbitals. Other authors, studying the origin of the  $K\beta''$  spectral line in other compounds, supported Best's interpretation. It is the case, for instance, of Ern et al (1965), who stated that the titanium  $K\beta''$  X-ray line in the compounds titanium boride and carbide comes from the transition between the  $4t_2$  orbital (mostly ligand 2s in character) and metal 1s orbital. In both cases the energy differences between emission lines formed the basis for the assignment. Indeed, the energy separation between the  $K\beta_{1,3}$  and  $K\beta''$  X-ray lines agreed well with the metal 3p - ligand 2s energy separation. The same reasoning was used for the  $K\beta_{1,3}$  and  $K\beta_{2,5}$ , the encountered difference in energy being close to the value observed for the separation in energy between the metal 3p and the ligand 2p orbitals. Nevertheless, these considerations did not allow Best to conclude anything about the origin of the  $K\beta_{2,5}$ , that is, whether  $5t_2$  and  $6t_2$  would participate in the transition, or whether  $K\beta_{2,5}$  would be formed by an unresolved doublet.

### III.3.4 $K\beta_{2,5}$ Energy Shifts

In Tables III.7 and III.8 the observed energy shifts in the  $K\beta_{2,5}$  peaks for some chromium, titanium and vanadium compounds were presented. The reference in all the cases was assumed to be the  $K\beta_{2,5}$  peak energy of the corresponding metallic element. It is seen that the  $K\beta_{2,5}$  peak is shifted to the higher energy side, as one goes from the less to the more oxidized state. When the transition which gives rise to the X-ray emission directly involves electrons of the valence shell, the variation of the formal oxidation state of the emitting atom causes a much more pronounced energy shift. The effect observed is indeed rather strong, but completely opposed to that shown by the  $K\beta_{1,3}$  peak (see Tables III.1 and III.2). Since in the molecular orbitals the ligand character is the dominant effect, the ionization energies of these orbitals will be determined by the ligand orbital energies. The ionization energy of the 1s electrons, on the other hand, increases with the increase of the formal oxidation number of the metal atom. In Figure III.10 the energy shifts of the levels involved in the  $K\beta_{2,5}$  transition for the chromium oxides are depicted. It is observed that the Cr 1s orbital is more tightly bound in the Cr(VI) than in the Cr(III) compounds, that is, the 1s energy is decreasing as one goes from Cr(VI) to Cr(III). Yet, the energy of the molecular orbital involved in the same transition is practically constant.

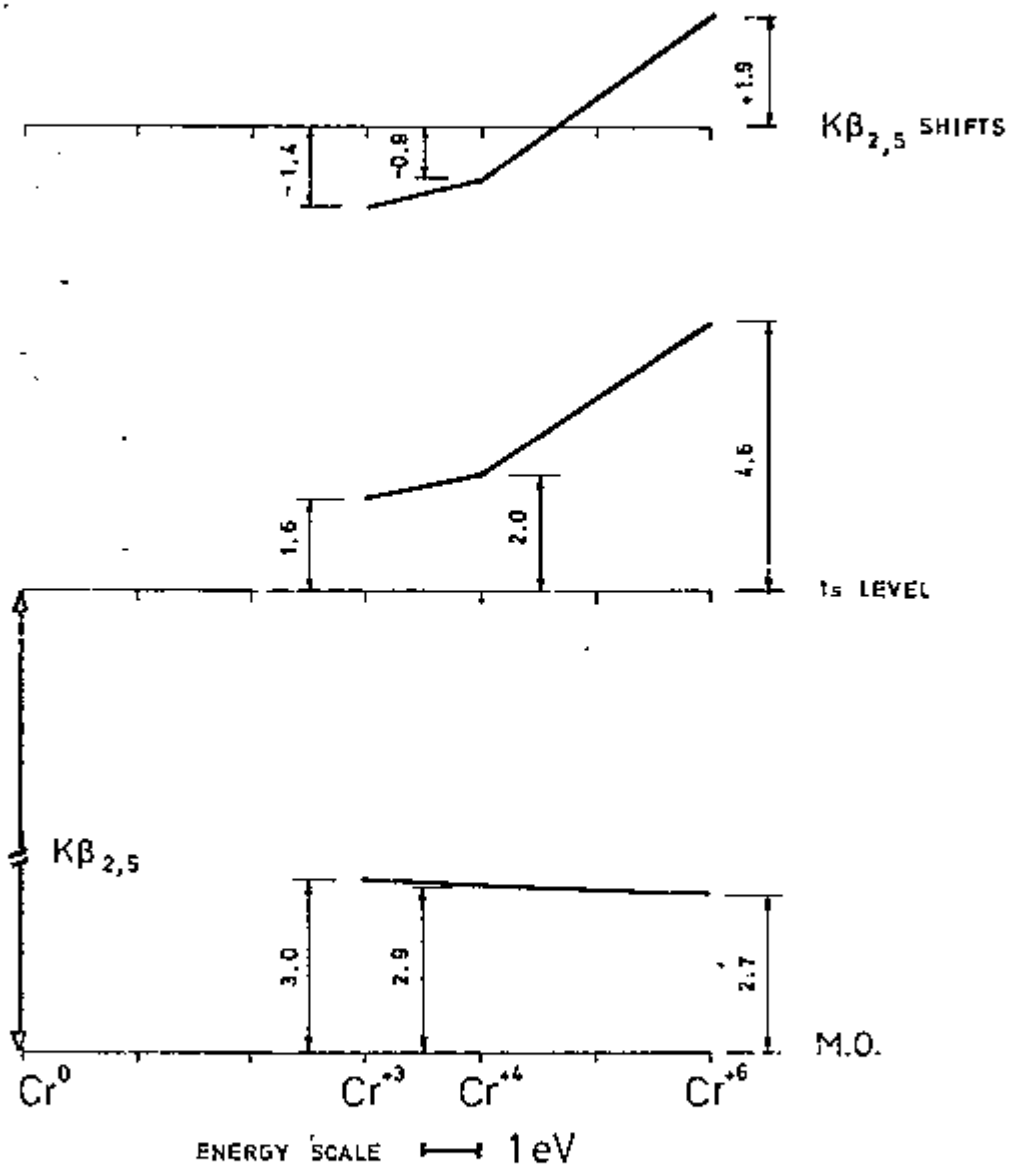


Figure III.10

Energy level diagram for the Cr  $K\beta_{2,5}$  line

CHAPTER IVCHEMICAL EFFECTS IN  $K\beta/K\alpha$  X-RAY EMISSION INTENSITIESIV.1 Introduction

Up to this point, we have mainly studied the chemical effects which occur in emission spectra for different compounds in terms of the absolute energy of the peaks. In the present chapter we shall investigate the variations which occur in the intensity of the  $K\beta$  and  $K\alpha$  emission lines in terms of the formal oxidation state of the transition metal in the compound.

Chemical effects in X-rays arising from core transitions are usually small and most investigations have concentrated on precise measurement of the shifts in peak energies. For first-row transition elements, perturbations in  $K\alpha_{1,2}$ ,  $K\beta_{1,3}$ ,  $K\beta'$  and  $K\beta_{2,5}$  energies have been studied for many compounds. Changes in peak intensities, however, have been less investigated, with the exception of the relative intensities of  $K\beta'/K\beta_{1,3}$  which were found to be correlated with the number of unpaired 3d electrons (Slater & Urch, 1972). Urch (1975) suggested that the relative peak intensities might also be influenced by the chemical state, that is, valence and ligand environment of the emitting atom, and that such information could then be used to investigate the chemical state of a radioactive recoil atom in a solid matrix, provided it decayed by electron capture with consequent emission of X-rays. Chromium has such an isotope and the work described in this chapter is concerned

with a wide range of chromium, as well as vanadium and titanium compounds. Results using an energy-dispersive technique have already been reported (Tamaki et al, 1975, 1978, 1979) but the claim to have observed a clear variation in the  $K\beta/K\alpha$  intensity ratio with the chromium valence has been disputed (Lazzarini, 1978).

Emission of radiation can occur whenever the electronic states of an atom have been excited. Within the independent-electron approximation, excited states are considered to be created when one electron has been ejected from its normal state. In principle, any electron less tightly bound can fall to the vacancy formed. The excited states may, among other decay processes, radiate the excess of energy in the form of photons. There are normally several electrons that are capable of filling a vacancy.

The intensity of a particular X-ray line will depend upon the electronic populations of the levels between which the transition takes place, and upon the transition probability. If we are dealing with absolute intensities, it is important to consider the ionization cross section of the initially ionized level, as well. One way of avoiding this additional calculation is to consider the relative intensities between X-ray lines which have their origin in the same ionized level. This is the case, for instance, of the  $K\beta$  and  $K\alpha$  emission lines, whose transitions arise from vacancies formed in the same  $1s$  level. The electronic population of the level from whence the transition takes place can also be ignored, as we are dealing with compounds of transition metals, in which the  $2p$  and  $3p$  levels are

completely filled. The transition probability will therefore be the only important factor in the determination of the  $K\beta/K\alpha$  intensity ratio.

As it is known, the intensity of an X-ray emission line can also be influenced by the possibility of an Auger transition (Chapter I, section I.5). Here, again, the problem can be overcome by studying the relative intensities of two lines originating in the same initial level.

In Figure IV.1 the radial probability functions for the 1s, 2p and 3p orbitals of the hydrogen atom are illustrated (Huheey, 1978; Herzberg, 1944).

These functions give the probability of finding the electron in a spherical shell of thickness  $dr$  at a distance  $r$  from the nucleus. The presence of one or more nodes causes small maxima in electron density between the nucleus and the largest maximum. It is often stated that these nodes and maxima have no chemical effect, but this is slightly misleading. There are several ways in which these nodes and maxima could influence the bonding, affecting the total overlap of the atomic orbitals which combine to form the bond. It is possible to verify by the analysis of Figure IV.1 that the degree of interaction between the 1s and 2p orbitals is much more intense than in the case of the 1s and 3p orbitals.



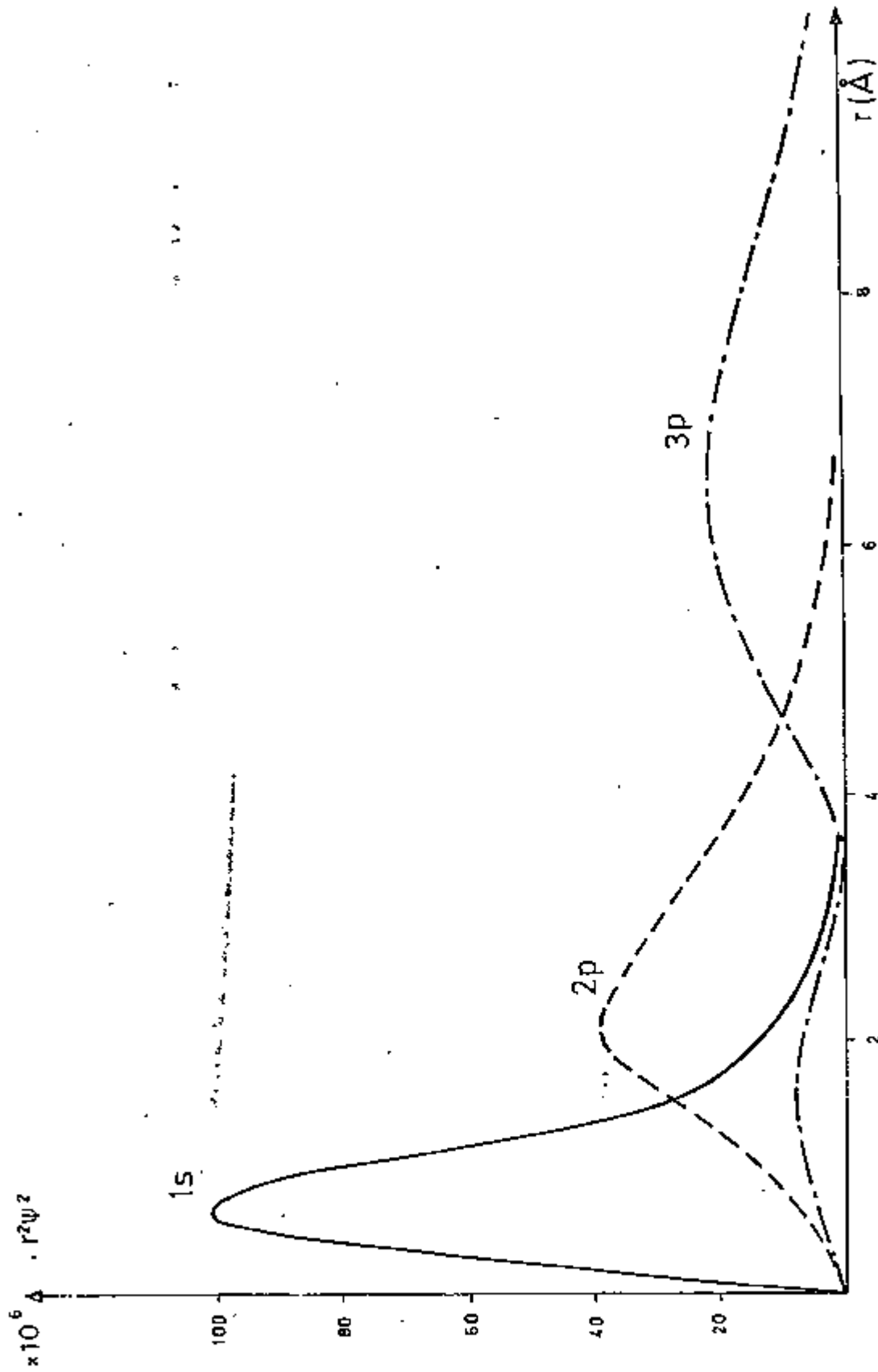


Figure IV.1

Radial distribution functions for  $n = 1, 2, 3$  for the hydrogen atom

As the 2p and 3p orbitals are completely filled for the transition elements, the first experiments performed did not take into account, in the final results, the effects of chemical composition or of the oxidation state of the element under investigation. It was originally thought (Beckman, 1933; Meyer, 1929; Williams, 1933) that the  $K\beta_{1,3}/K\alpha_{1,2}$  ratio was only dependent on the different degree of interaction of the 3p and 2p orbitals with the 1s orbital. It was also believed that the ratio varied very little with the increase of atomic number for the first-row transition metals. As the 3p and 2p orbitals represent "core levels" with the same electronic population, it was then concluded that the radial distribution curve for the 3p and 2p orbitals did not vary extensively due to the increase of valence electrons in the 3d sub-shell.

It is now known that the change in valence of a transition metal implies in variations in the atomic orbital radial function (Urch, 1971). As the transition probability is influenced by these variations in atomic orbital radial function, we should also expect changes in the corresponding emission peak intensities. The purpose of the present chapter is to measure the intensity of emission lines such as  $K\beta$  and  $K\alpha$  for transition metal compounds in different oxidation states, and establish to what extent these changes can be experimentally verified.

#### IV.2 Theoretical Calculations of X-ray Emission Rates in the Filling of Vacancies in the K Shell

Theoretical calculations of the radioactive transition rates have been carried out by several authors (Asaad, 1959; Babushkin, 1964; Lasker, 1955; Massey et al, 1936; Payne et al, 1956; Scofield, 1969; Taylor et al, 1960). All of these calculations except Asaad's were based on the Coulomb potential. Massey, Lasker and Babushkin introduced an effective nuclear charge to account for the screening of the nucleus by the electrons. Scofield calculated the  $K\beta/K\alpha$  ratio for the titanium, vanadium and chromium metals, obtaining the values 0.1138, 0.1367 and 0.1337, respectively.

#### IV.3 Experimental Data on the Relative Intensities of X-ray Lines

In the first experiments several attempts were made in order to measure the relative intensities of some lines in the K series of certain isolated elements (Allison et al, 1925; Duane et al, 1920; Siegbahn et al, 1923; Woo, 1926). As the main aim at that time was to obtain reliable data on the relative transition probabilities of these lines, it was necessary to apply very accurate corrections to the experimental results.

In all the methods there was little difficulty in obtaining reliable results on the relative intensities of two lines of small wavelength separation. As the separation of the two lines increases, however, the corrections which had to be applied became increasingly difficult to

calculate. This is because the reflection coefficient of the analysing crystal varies with the incident beam wavelength, as was verified in the course of the present experimental work.

The range of atomic numbers in which these early experiments were performed has been completely covered in the work of Meyer (1929), of Williams (1933) and of Beckman (1933). Meyer measured the relative intensities in the K series from vanadium to indium. But the values given by him were uncorrected for absorption effects. On the other hand, Williams had made measurements from chromium to tellurium correcting his observations for the fraction of the direct beam absorbed in the length of the ionization chamber, the absorption in the air path, in the windows of the X-ray tube and ionization chamber, and for the variation of the coefficient of reflection of the crystal with wavelength.

In order to obtain data on the relative transition probabilities of these lines, a correction had also to be made for self-absorption within the target. This correction was very difficult to calculate with high accuracy. A rough estimate was made assuming that the rate of loss of kinetic energy of the incident radiation (as a function of the penetration depth of the target) and the probability of ionizing the K shell (as a function of electron velocity) were known. Williams has carried out such a calculation and found that the correction to be applied to the intensity ratio  $K\beta_{1,3}/K\alpha$  (as measured on the surface of the target) varied from a factor of 0.97 in chromium to 1.00 in tellurium, it thus being within the experimental error. A

survey of the results obtained up to the 1960's was tabulated by Wapstra et al (1959).

With the advent of various theoretical models used to calculate the radioactive transition rates to the K shell, the measurement of the  $K\beta/K\alpha$  ratio became important as a test of these models. Several experimental studies were therefore made using high-resolution solid state X-ray detectors.

One feature of the theoretical results is that  $K\beta/K\alpha$  is relatively constant for  $21 \leq Z \leq 30$ , where the 3d levels are being filled. The experimental results of Salem et al (1969), however, showed a rapidly increasing ratio with Z and no flat portion anywhere in this region. Their results favoured the theoretical calculations by Babushkin (1964) who found no flat region for  $21 \leq Z \leq 30$ . But the results of Slivinsky et al (1972) formed a smoothly varying function with Z which agrees well with the calculation by Scofield (1969).

Hansen et al (1970) performed  $K\beta/K\alpha$  measurements for cases of K vacancies created by K-electron capture. Hansen's results showed a relatively flat portion of the curve only for  $26 \leq Z \leq 33$ ; for elements with  $Z \leq 26$ ,  $K\beta/K\alpha$  decreased more rapidly with decreasing Z than the theory indicates (Scofield, 1969). Their data concerning the Ti, V and Cr elements displayed a marked departure from the body of  $K\beta/K\alpha$  ratios measured via excitation by bremsstrahlung X-rays or electron bombardment (see Table IV.1).

REFERENCE	Ti	V	Cr
Scotfield (1969)	0.1138	0.1367	0.1337
Salem et al (1972)	0.135	0.137	0.138
Hansen et al (1970)	0.0945(*)	0.2053(*)	0.1135±0.0023(*)
Slivinsky et al (1972)	0.1319±0.0017	0.1339±0.0011	0.1344±0.0011
Gohshi et al (1973)		0.134±0.002	0.134±0.002
Paic et al (1976)	0.133±0.002 0.123±0.002(*)	0.134±0.002 0.121±0.002(*)	0.134±0.002 0.127±0.002(*)
Tamaki et al (1975, 1978, 1979)		0.132(*) 0.120(*) 0.123-0.135(*) 0.131-0.144(*)	0.134 labelled CrII compounds labelled CrIII compounds labelled CrVI compounds
Lazzarini et al (1978)		0.147-0.136(*) 0.141-0.136(*)	labelled CrIII compounds labelled CrVI compounds

Table IV.1

K $\beta$ /K $\alpha$  intensity ratios (\*\*)

(\*) experimental data obtained from K-capture excitation

(\*\*) all the values were compiled from experimental results, except Scotfield's theoretical calculations.

Besides the work of Hansen et al (1970), there was a measurement of the  $K\beta/K\alpha$  ratio in the  $Z < 28$  region, with especial emphasis on the comparison of X-ray excitation and K-capture decay (Paić et al, 1976). It can be seen that the results obtained by X-ray excitation are in very good agreement with the evaluated values proposed by Salem et al (1972) and Slivinsky et al (1972). On the other hand, differences exist between the  $K\beta/K\alpha$  ratio for K-capture nuclei and that for X-ray excitation, although the discrepancies are not so significant as in the experimental results of Hansen et al (1970) (see Table IV.1).

A survey of the theoretical and experimental results obtained in the 1960's has been carried out by Nelson et al (1970). They plotted different relative transition probabilities as functions of atomic number. In Figure IV.2 the transition probability ratio  $K\beta/K\alpha$ , where  $K\beta = K\beta_{1,3} + K\beta' + K\beta_{2,5}$  and  $K\alpha = K\alpha_1 + K\alpha_2$ , is shown.

In all the measurements which had been carried out up to that time, an emphasis was placed on a comparison of the experimental results with theoretical calculations. The effect of the chemical composition on the  $K\beta/K\alpha$  intensity ratio, however, has never been considered at all.

Slivinsky et al (1972) mentioned that chemical effects, such as an oxidized thin target, did not change the results. Salem et al (1972) have compared the results obtained from amorphous samples with those from crystalline metal samples, but did not find significant effects.

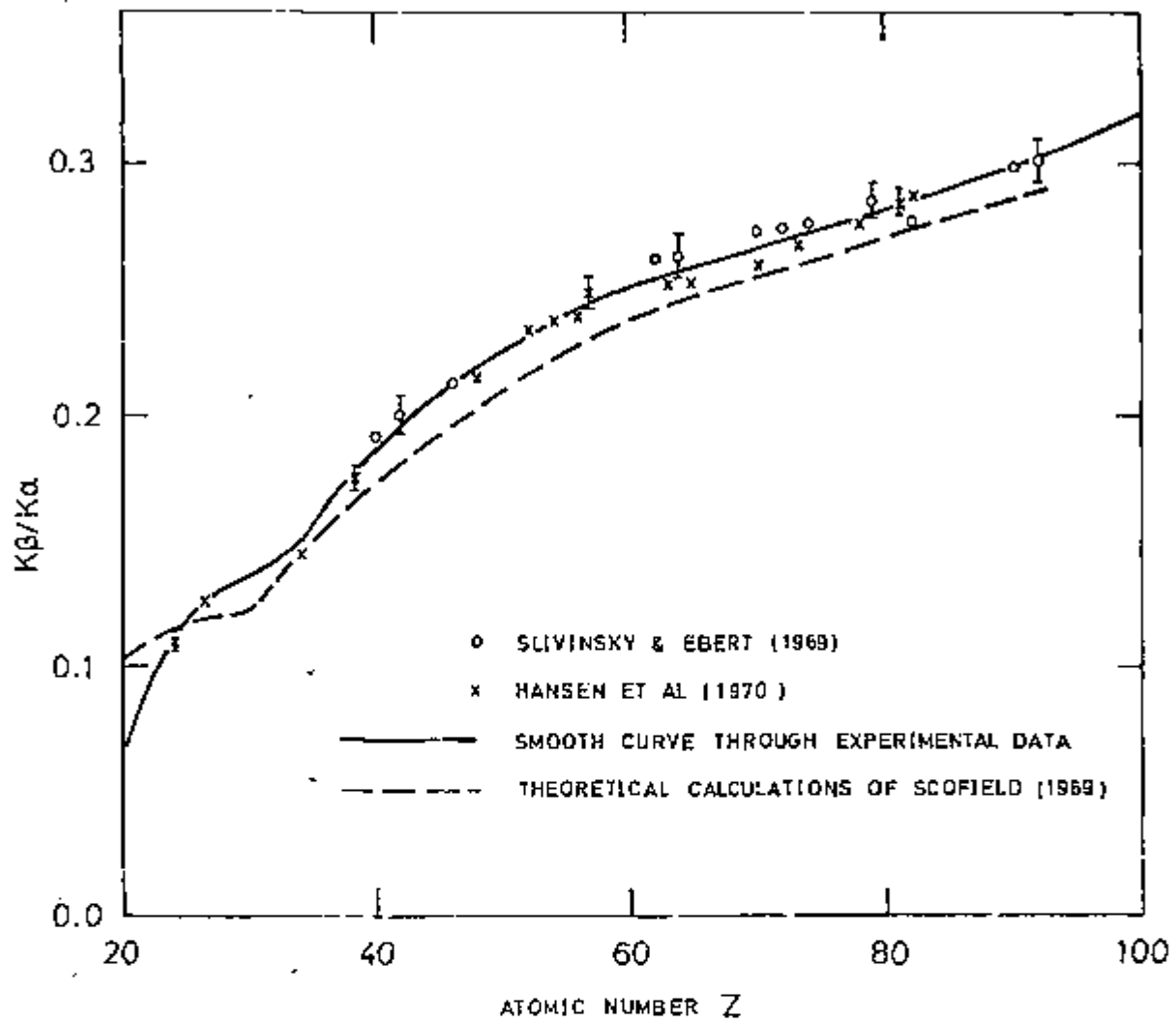


Figure IV.2.

Transition probability ratio  $K\beta/K\alpha$  as function of the atomic number ( $Z$ )

from Nelson et al (1970)

On the other hand, studies by means of an X-ray fluorescence spectrometer have revealed that the X-ray energy and intensity are altered by the chemical state of the target compounds (Urch, 1971). In particular, the appearance of  $K\beta$  satellite peaks gives rise to alterations in peak shape, energy and intensity. These alterations



should affect the  $K\beta/K\alpha$  intensity ratio measurements, as well.

Tamaki et al (1975, 1978, 1979) and Lazzarini et al (1978) studied the  $K\beta/K\alpha$  intensity ratios by measuring X-ray emitted from various Cr - labelled compounds. The  $^{51}\text{Cr}$  decays primarily to ground state of  $^{51}\text{V}$  by electron capture. Thus, a hole created in the K shell as a consequence of electron capture is quickly filled by a cascade of electrons, with the simultaneous ejection of Auger electrons and emission of X-rays. Lazzarini et al (1978) stated that the chemical bond would influence not only the relative probability of the two transitions, but also the probability that the transition occurs with emission of radiation. In this latter case, a competition between the de-excitation by means of the Auger transition, and the de-excitation by means of the X-ray emission would be occurring. The Auger transition, however, should not affect the result, since we are dealing with the relative intensity of two lines originated in the same initial excited state. Although in the electron capture decay the effects of recoil and of electronic excitation as a result of the sudden change in nuclear charge may, to some extent, be associated, on the moment of X-ray emission we can consider that the chemical structure of the parent molecule still remains unchanged in the daughter molecule.

The results obtained by the two authors, using the same experimental technique can be seen in Table IV.1. The data obtained by Lazzarini et al (1978) for the  $\text{Cr}^{3+}$  doped crystals seem to suggest that the lattice parameters of the

host crystals have a great influence on the phenomenon. Indeed, they found that the  $K\beta/K\alpha$  ratio depends both on the chemical form of the parent radionuclides and on the type of crystals in which the radionuclides are embedded. The formal oxidation number of the emitting atom, on the other hand, was found to have no influence on the values of the  $K\beta/K\alpha$  ratio, contrary to results found by Tamaki et al (1975, 1978, 1979).

In the next section the experimental results obtained in the present work will be presented. We shall then compare our results with the previous experiments and calculations.

#### IV.4 Experimental Results and Discussion

The experimental results were obtained by stepping over the peak positions at  $0.02^\circ$   $2\theta$ -intervals, and counting for a fixed time. The time of counting was adjusted for each sample. At least two determinations of each spectrum were made and the results obtained were compared with each other.

The intensity of an emission line may be estimated by the height of the respective peak or by the area under the spectrum. The second approach, it being more accurate, was chosen for the development of the present study. Actually, it allows small variations in shape and peak width to be taken into account, whereas in the former approach they would be crudely neglected. For each sample the intensity of  $K\beta$  and  $K\alpha$  were therefore obtained by the evaluation of the area under the spectrum. The final  $K\beta/K\alpha$  ratio was expressed by the following equation :

$$\frac{AK\beta \pm \Delta AK\beta}{AK\alpha \pm \Delta AK\alpha} = \frac{AK\beta}{AK\alpha} \pm \frac{AK\beta}{AK\alpha} \left[ \left( \frac{\Delta AK\alpha}{AK\alpha} \right)^2 + \left( \frac{\Delta AK\beta}{AK\beta} \right)^2 \right]^{1/2}, \quad (\text{IV.1})$$

where :  $AK\beta$  = area under the  $K\beta$  spectrum;

$AK\alpha$  = area under the  $K\alpha$  spectrum;

$\Delta AK\alpha, \Delta AK\beta$  = absolute standard deviations of the  
; quantities  $AK\alpha$  and  $AK\beta$ , respectively.

In principle, the intensity  $I(\lambda_j)$  of an X-ray line arising from an element  $j$  in a matrix made up of different elements is affected by both primary and secondary absorptions. Since we are dealing with  $K\beta/K\alpha$  intensity ratios, the primary absorption can be duly neglected, on the grounds that both lines originate in transitions from the same initial ionized state ( $1s^+$ ). As for the secondary absorption, its influence can be estimated by the exponential law :

$$I = I_0 \exp(-\mu\rho x) \quad , \quad (\text{IV.2})$$

where :  $I/I_0$  = fraction of the radiation which passes  
through the absorber;

$\mu$  = mass absorption coefficient of the matrix;

$\rho$  = density of the matrix;

$x$  = penetration depth of the radiation.

Therefore, the radiation intensity measured should be corrected to take into account the secondary absorption.

SAMPLE	$A \pm \Delta A$	$A \pm \Delta A$	(*)	(*)
	$K\beta_{1,3} + K\beta'$	$K\alpha_{1,2}$	$\frac{K\beta_{1,3} + K\beta'}{K\alpha_{1,2}}$	$\frac{K\beta_{1,3}}{K\alpha_{1,2}}$
VANADIUM METAL	$0.7812 \pm 0.0068$	$12.757 \pm 0.086$	0.061	0.055
ACETYLACETONATO VANADIUM (III)	$0.3893 \pm 0.0033$	$6.128 \pm 0.041$	0.064	0.056
VANADIUM (III) FLUORIDE	$0.5608 \pm 0.0048$	$8.484 \pm 0.057$	0.066	0.058
VANADIUM (III) OXIDE	$0.5409 \pm 0.0046$	$8.472 \pm 0.057$	0.064	0.056
VANADYL SULPHATE	$0.3248 \pm 0.0028$	$4.829 \pm 0.033$	0.067	0.060
VANADYL ACETYLACETONE	$0.4861 \pm 0.0041$	$7.592 \pm 0.051$	0.064	0.057
VANADYL PHTHALOCIANINE	$0.1666 \pm 0.0015$	$2.818 \pm 0.019$	0.059	0.053
VANADIUM PENTOXIDE	$0.7122 \pm 0.0062$	$11.176 \pm 0.076$	0.064	0.058
AMMONIUM METAVANADATE	$0.6654 \pm 0.0058$	$10.299 \pm 0.071$	0.065	0.058

Table IV.2

Intensity of vanadium  $K\beta_{1,3} + K\beta'$  and  $K\alpha_{1,2}$  X-ray emission peaks. Relative intensities

(\*) The absolute standard deviation of this ratio is 0.001

SAMPLE	$A \pm \Delta A$	$A \pm \Delta A$	(*)	(*)
	$K\beta_{1,3} + K\beta'$	$K\alpha_{1,2}$	$\frac{K\beta_{1,3} + K\beta'}{K\alpha_{1,2}}$	$\frac{K\beta_{1,3}}{K\alpha_{1,2}}$
TITANIUM METAL	0.2057±0.0018	3.032±0.021	0.068	0.063
TITANIUM (III) OXIDE	0.1711±0.0015	2.444±0.017	0.070	0.064
TITANIUM (III) FLUCRIDE	0.1123±0.0010	1.659±0.012	0.068	0.063
Ti <sub>3</sub> O <sub>5</sub>	0.2137±0.0019	3.060±0.022	0.070	0.066
Ti <sub>2</sub> O <sub>3</sub> + TiO <sub>2</sub> + TiO	0.1725±0.0016	2.407±0.017	0.072	0.067
TITANIUM CARBIDE	0.2189±0.0020	3.130±0.022	0.070	0.066
TITANIUM (IV) OXIDE	0.2256±0.0021	3.221±0.023	0.070	0.066
CALCIUM ORTHOTITANATE	0.0685±0.0006	0.950±0.007	0.072	0.068
CALCIUM METATITANATE	0.0549±0.0005	0.745±0.005	0.074	0.069
STRONTIUM METATITANATE	0.0407±0.0004	0.555±0.004	0.073	0.070
ETHYL METATITANATE	0.1220±0.0011	1.779±0.013	0.069	0.064
POTASSIUM HEXAFLUORO TITANIUM (IV)	0.0395±0.0004	0.527±0.004	0.075	0.071

Table IV.3

Intensity of titanium  $K\beta_{1,3} + K\beta'$  and  $K\alpha_{1,2}$  X-ray emission peaks. Relative intensities

SAMPLE	$A \pm \Delta A$	$A \pm \Delta A$	(*)	(*)
	$K\beta_{1,3} + K\beta'$	$K\alpha_{1,2}$	$\frac{K\beta_{1,3} + K\beta'}{K\alpha_{1,2}}$	$\frac{K\beta_{1,3}}{K\alpha_{1,2}}$
CHROMIUM METAL	0.2153±0.0020	2.843±0.022	0.076	0.064
CHROMIUM (III) OXIDE	0.4840±0.0044	6.426±0.050	0.075	0.061
ACETYLACETONATO CHROMIUM (III)	0.3063±0.0027	4.041±0.031	0.076	0.061
TRIETHYLENEDIAMINE CHROMIUM (III) CHLORIDE	0.1269±0.0011	1.641±0.013	0.077	0.062
HEXAUREACHROMIUM (III) CHLORIDE	0.1507±0.0014	1.861±0.014	0.081	0.060
CHROMIUM (III) SULPHATE	0.2195±0.0020	2.790±0.021	0.079	0.064
POTASSIUM HEXATHIOCYANATO CHROMIUM (III)	0.0304±0.0003	0.409±0.003	0.074	0.060
POTASSIUM TRIOXALATO CHROMIUM (III)	0.1060±0.0010	1.341±0.010	0.079	0.064
CHROMIUM (III) CHLORIDE	0.1056±0.0010	1.367±0.011	0.077	0.061
CHROMIUM (IV) OXIDE	0.2065±0.0019	2.665±0.021	0.077	0.064
CHROMIUM (VI) OXIDE	0.5316±0.0047	7.155±0.055	0.074	0.061
POTASSIUM CHROMATE	0.1563±0.0015	1.966±0.016	0.080	0.061
SODIUM CHROMATE	0.3941±0.0037	5.136±0.040	0.077	0.061
LEAD CHROMATE	0.0456±0.0004	0.555±0.004	0.082	0.071
POTASSIUM DICRHOMATE	0.2014±0.0019	2.517±0.020	0.080	0.061

Table IV.4

Intensity of chromium  $K\beta_{1,3} + K\beta'$  and  $K\alpha_{1,2}$  X-ray emission peaks. Relative intensities

Nevertheless, it can be shown that the correction factor which should be applied to the  $K\beta/K\alpha$  intensity ratios is roughly equal to one. Therefore, within the order of the experimental errors, we may assume that the theoretical values of the  $K\beta/K\alpha$  ratios are practically the same as those determined experimentally.

The results obtained for the  $K\beta/K\alpha$  ratio for the chromium, vanadium and titanium compounds are summarized in Tables IV.2, IV.3 and IV.4.

The  $K\alpha$  characteristic emission spectrum has its origin in the  $2p \rightarrow 1s$  electronic transition. In the final configuration, the  $2p^5$  is splitted in two energy levels ( $j = 1/2$  and  $j = 3/2$ ) due to the spin-orbit coupling. The emission spectra is therefore made up of two spectral lines  $K\alpha_1$  and  $K\alpha_2$ , which correspond to the transitions  $2p_{3/2} \rightarrow 1s$  and  $2p_{1/2} \rightarrow 1s$ , respectively. In analogy with what we have described for the  $3p^5$  orbital in Chapter III, electronic interactions will also occur between the  $2p^5$  electrons and the uncoupled  $3d$  electrons. The coupling of the respective spin angular momenta will give rise to multiple final states, which on their turn will influence the shape and the intensity of the obtained peaks, exactly in the same way as for the  $3p^5$  electrons. Yet, due to the fact that the  $3p$  electrons are not considered "true core electrons", the degree of interaction will be different in both cases, the "chemical effects" being more pronounced for the electrons belonging to the  $3p$  subshell. Indeed, it is possible to verify by the analysis of the radial probability functions that the degree of overlap between the  $3p$  and the

3d orbitals is much more intense than in the case of the 2p and the 3d orbitals. The above argument leads logically to the idea of greater chemical effects for the  $K\beta_{1,3} + K\beta'$  than for the  $K\alpha_{1,2}$ . If there were observable effects in both  $K\beta_{1,3} + K\beta'$  and  $K\alpha_{1,2}$ , then the ratio might well be invariant. If, on the other hand, the two emission peaks were subjected to different valence shell effects, then these effects might be present in the  $K\beta/K\alpha$  ratio, as well. The direct analysis of the experimental results obtained does not lead to any correlation between the  $K\beta/K\alpha$  ratio and the formal oxidation number of the transition metal present in the molecule.

In Chapter III a more detailed study on the  $K\beta$  spectrum was pursued and it was verified that the  $K\beta'$  intensity increases as the oxidation number of the transition metal decreases. This increase in the  $K\beta'$  peak intensity must occur at the expense of a drop in the main peak ( $K\beta_{1,3}$ ) intensity, in order to keep the overall intensity unchanged. We therefore decided to study the  $K\beta/K\alpha$  ratio from other viewpoint, trying to eliminate the influence of the  $K\beta'$  peak on the area under the  $K\beta$  emission spectrum. In other words, we have attempted to consider separately the intensity of the main peak ( $K\beta_{1,3}$ ). To do so, the values obtained for the  $K\beta' + K\beta_{1,3}$  area were multiplied by the factor :

$$F = \left( 1 + \frac{IK\beta'}{IK\beta_{1,3}} \right)^{-1} \quad , \quad (IV.3)$$

where :  $IK\beta'$  =  $K\beta'$  peak intensity;

$IK\beta_{1,3}$  =  $K\beta_{1,3}$  peak intensity.



The results thus obtained are summarized in Tables IV.2, IV.3 and IV.4. We can now discern an increase in the  $K\beta_{1,3}/K\alpha_{1,2}$  ratio, as the oxidation number of the emitting atom increases. We were able to verify this behaviour from the experimental spectra only because of the high resolution of the spectrometer, which separates the  $K\beta_{1,3}$  main peak from the  $K\beta'$  satellite line, whenever they are resolvable. It is therefore surprising that Tamaki et al (1975, 1978, 1979) have managed to obtain the same variation using an energy-dispersive detector, which exhibits poorer resolution than wavelength-dispersive methods.

Estimation of an emission line intensity (by the evaluation of the area under the spectrum) supplied us with reliable results, since we were interested in the investigation of the relative  $K\beta/K\alpha$  ratio for a series of compounds of the same element. Yet, problems do occur when the results are compared in absolute values with those of all other experimental works. All the studied spectra were recorded using an order of reflection equal or superior to 3, which gave us the best experimental compromise between efficiency and resolution. Since the separation between the two lines ( $K\alpha$  and  $K\beta$ ) increases with the increasing of the order of reflection, it is possible that the effect of factors such as the reflection coefficient of the analysing crystal be varying, as well. The  $K\beta/K\alpha$  ratio of metallic samples were studied for different order of reflections. The results obtained (Table IV.5) show that the ratio is indeed varying with  $n$ , in a dramatic way, approaching the values found in the literature as  $n$  is getting smaller.

METALLIC SAMPLE	n = 4	n = 3	n = 2
TITANIUM		0.068±0.001	0.139±0.002
VANADIUM	0.061±0.001	0.122±0.002	0.131±0.002
CHROMIUM	0.076±0.001	0.136±0.002	0.138±0.002

Table IV.5

$(K\beta_{1,3} + K\beta') / K\alpha_{1,2}$  ratio for different order of reflections

For the specific case of the determination of  $K\beta$  and  $K\alpha$  spectra for the vanadium compounds, we have used the fourth order of reflection. If we evaluate the angular dispersion ratio between  $K\beta$  and  $K\alpha$  for the order  $n$  equal to 4, we shall find (for metallic vanadium) :

$$R_4 = \frac{(d\theta/d\lambda) K\beta}{(d\theta/d\lambda) K\alpha} = \frac{(\cos \theta) K\alpha}{(\cos \theta) K\beta} = 0.66 \quad (IV.4)$$

Analogously, for the third order we shall have :

$$R_3 = 0.93 \quad (IV.5)$$

Therefore, this ratio has increased by a factor of 42% when we go from  $n = 4$  to  $n = 3$ .

We can also see that the angular dispersion in both cases ( $K\beta$  and  $K\alpha$ ) is getting closer, as the angle of incidence for the  $K\beta$  and  $K\alpha$  tend to the same value, that is,

when the order of reflection  $n$  tends to 1, the ratio  $R_n$  also tends to 1. The angular dispersion might therefore be one of the possible factors (due to the analysing crystal) responsible for the difference found in the  $K\beta/K\alpha$  intensity ratios. Unfortunately, it was not possible to obtain reliable results for the  $K\beta/K\alpha$  ratio for the first order of reflection, because the corresponding Bragg angles were very close to each other. Anyhow, the results shown in Table IV.5 (for the second order of reflection) are already very close to those found in the literature (compare with Table IV.1).

The analysis of Tables IV.2, IV.3 and IV.4 allows us to conclude that the  $K\beta_{1,3}/K\alpha_{1,2}$  ratio is being affected by the oxidation state of the X-ray emitting atom. The chemical environment of the emitting atom was found to influence very little the  $K\beta_{1,3}/K\alpha_{1,2}$  ratio, the variations being practically within the experimental error (see, for instance, the results concerning the potassium, sodium and lead chromates). The influence of the chemical bond in the relative probability of the two transitions seems, therefore, the most reasonable explanation for the results obtained.

CHAPTER VMOLECULAR ORBITAL INTERPRETATION OF X-RAY EMISSION SPECTRA  
INVOLVING VALENCE BAND ELECTRONSV.1 Introduction

In this chapter we shall investigate spectral lines which originate from electronic transitions in the valence band region. The X-ray emission lines  $L\alpha_{1,2}$  and  $L\beta_1$  are photons emitted when an atom ionized in the 2p subshell undergoes radioactive decay by means of the  $3d \rightarrow 2p$  transition. Due to the spin-orbit coupling, the initial state  $2p^+$  split into two energy levels  $2p_{3/2}^+$  and  $2p_{1/2}^+$ . Transitions from the  $3d_{3/2}$  level to either state are allowed according to the electric dipole selection rule. On the other hand, the  $3d_{5/2}$  level can only relax by means of a transition to the  $2p_{3/2}$  level, the  $3d_{5/2} \rightarrow 2p_{1/2}$  transition being forbidden, as it transgresses the dipole selection rule  $\Delta J = 0, \pm 1$ . We therefore have two emission lines,  $L\alpha_{1,2}$  ( $3d_{3/2,5/2} \rightarrow 2p_{3/2}$ ) and  $L\beta_1$  ( $3d_{3/2} \rightarrow 2p_{1/2}$ ). Since the  $2p_{3/2}^+$  state is less excited than the  $2p_{1/2}^+$  state, the  $L\beta_1$  photons will be of shorter wavelength.

The  $K\beta_{2,5}$  region, on the higher-energy side of the  $K\beta_{1,3}$  peak, also relates to valence band electronic transitions. Indeed, in such a region of the spectrum we normally find one or more peaks arising from the  $4p \rightarrow 1s$  electronic transition.

At a slightly higher energy than these emissions from valence band orbitals, the corresponding absorption edges

will be found. However, for elements with a partially filled 3d shell (such as vanadium, titanium and chromium), emission and absorption could, to a first approximation, have the same energy. Nevertheless, the edge is actually observed a few eV above the emission peak. This is usually less than the  $L\alpha - L\beta$  energy difference, so that the  $L\beta$  spectral line is readily absorbed by the sample itself.

## V.2 Molecular Orbital Theory Applied to the Interpretation of Soft X-ray Spectra

The combination of the  $K\beta_{2,5}$  and  $L\alpha$  X-ray emission spectra gives useful information about both 4p ( $K\beta_{2,5}$  emission line), and 3d and 4s ( $L\alpha$  emission line) character in the valence band.

Fischer and Baun (1968), and Fischer (1969), studying the  $L\alpha_{1,2}$  and  $L\beta_1$  spectra of some titanium and vanadium compounds, reported an anomalous satellite peak on the lower-energy side of the main peak  $L\alpha_{1,2}$ . By supposing that the metal-ligand bonding is mainly ionic and assuming a complete transferring of the metal charge to the ligand, they showed that the satellite line depended on the ligand anion. It was suggested that this additional band, which was not found in the pure metal, was due to a transition from the 2p level of the anion to an  $L_{111}$  vacancy in the metal. Similar ionic models had been previously used by the same author to explain the  $K\beta$  band of some compounds of third-row elements (Fischer, 1970a).

One objection to the ionic model is that it did not take into account the obvious interactions between the outer

orbitals of the metal and ligand in forming a compound. It is unlikely that the bonding in these compounds is purely ionic, there probably being a certain amount of covalent character present.

More recently, however, Urch (1970), reviewing the low-energy satellite peaks and the theories to explain their origin, concluded that molecular orbital theory (MOT) could be used to explain the origin of these peaks. He suggested that the low-energy satellite peaks arose from the perturbation and splitting of atomic orbitals due to bond formation. This new approach provided an explanation for the high emission intensity of the observed satellites, which is more adequate than the crossover transition theory of O'Brien and Skinner (1940).

Many investigators seemed to have the impression that molecular orbital theory was somehow restricted to highly covalent materials. Actually, the theory is quite capable of handling the various types of bonding, from completely ionic at one end to completely covalent at the other. Many other researchers have also recognized the utility of MOT in explaining certain features of X-ray band spectra which are difficult or impossible to rationalize by any other means (Best, 1966, 1968; Dodd et al, 1968; Manne, 1970; Seka et al, 1969). Among these authors, the only ones to study first-row transition metal compounds were Best (1966) and Seka et al (1969).

Having in mind the MOT approach, Fischer published a series of papers in which he tried to give a molecular orbital interpretation to the soft X-ray spectra from some

titanium and vanadium compounds (1970b) and from chromium compounds (1971). He used an experimental technique in which the soft X-ray emission and absorption spectra were combined to construct a complete molecular orbital diagram for the compounds studied. X-ray emission bands, according to the theory, are due to electronic transitions from the occupied valence band to an inner-level vacancy. On the other hand, the absorption spectra are due to the ejection of an inner-level electron into one of the available vacant states in the outer region of the atom. These combined techniques allowed him to have a complete picture of the MO energy level diagram, involving both occupied and vacant orbitals within 20 eV or so of the Fermi level. Although dealing with insulators, Fischer used this level as a reference for the alignment of all the X-ray spectra with the MO structure. He placed the zero of energy at the Cr L<sub>III</sub> absorption edge, by assuming for a common absorption edge for all spectra the point where the emission and absorption spectra for the given element overlap.

This assumption may not however be true, and the use of core ionization energies directly determined by X-ray photoelectron spectroscopy is perhaps a better basis of alignment for the X-ray emission spectra. In the next section the application of the XPS and XRES combined techniques will be presented.

### V.2.1 Alignment of the X-ray Emission and X-ray Photoelectron Spectra

The purpose, here, is to study the electronic structure of the valence band, using as experimental techniques X-ray emission and X-ray photoelectron spectroscopies. Although these techniques are related to different types and probabilities of electronic transitions, they supply complementary results, since the former allows us to investigate the difference in energy between orbitals of the constituent atoms, whilst the latter gives the energy of all the orbitals present in the molecule (both core and valence band).

When a compound such as  $ML_n$  (where M is the metal and L is the ligand) is formed, the 3d, 4s and 4p levels of the metal atom interact with the 2s and 2p levels of the ligand atoms. The ligand atoms are normally composed of second-row elements, for which the 2p orbital is only partially filled. For the sake of brevity, we shall refer to any of these elements as L in what follows. The major difference in the molecular orbital energy level diagrams will be caused by the energies of the ligand 2p and 2s orbitals. In fact, there is a considerable decrease in the 2p - 2s energy separation, as one goes from oxygen to nitrogen and to carbon (Siegbahn et al, 1967). This decrease will move the resultant molecular orbitals closer together and the X-ray emission band spectra will therefore be spread over a smaller range. It is important to note, here, the addition of ligand 2s interaction with the metal orbitals. The ligand 2s orbitals are usually considered to be too tightly bound



to take part in the bonding. In Chapter III, however, it was shown that these orbitals need to be considered to account for the  $K\beta$  satellites in the spectra.

A combination of the metal  $K\beta_{2,5}$ ,  $L\alpha_{1,2}$  and the ligand  $K\alpha$  X-ray emission spectra will therefore provide us with useful information about the distribution of the molecular orbitals. These spectra, however, cannot be directly compared by plotting them in a same energy scale, unless the ionization energies of some inner orbitals of the atoms concerned are known. Nevertheless, it is possible to place the different emission spectra on a common energy scale by utilizing core-level binding energies determined by X-ray photoelectron spectroscopy. XPS measurements of metal 2p and ligand 1s level, for instance, allow us to draw the  $L\alpha$  and the ligand  $K\alpha$  on a same scale of the XPS valence band spectrum.

The same reasoning can also be applied to the  $K\beta_{2,5}$  emission spectrum. The energy of this peak can be considered as the difference between the metal binding energies of 4p and 1s orbitals. This latter energy can be indirectly obtained from :

$$\begin{aligned} \text{binding energy (M1s)} &= \text{energy of MK}\alpha + \\ &+ \text{binding energy (M2p)} \quad . \quad (\text{V.1}) \end{aligned}$$

In order to interpret all the available spectra once they are plotted in a same energy scale, it is important to have also at hand the schematic molecular orbital energy-level diagram. Of course, this diagram will be different for each compound, depending upon its structure. The common

structures which use d valence orbitals for forming  $\sigma$  bonding molecular orbitals are tetrahedral and octahedral. These configurations will be discussed in more detail in the next sections.

### V.3 Bonding in Chromium Compounds

#### V.3.1 The Chromate Ion

In the chromate anion the chromium atom is surrounded by a regular tetrahedral arrangement of oxygen atoms. The metal ion can be considered as being at the centre of a cube, the alternate vertices of which form the tetrahedron; the Cartesian axes pass through the centres of the faces of the cube. On each ligand atom a p orbital (namely a  $p_k$  orbital, if we consider a k,l,m Cartesian system for each ligand atom) is directed towards the metal atom. In this arrangement, the ligands do not directly approach any of the metal d orbitals, but they come closer to the  $3d_{xy,yz,xz}$  orbitals, directed to the edges of the cube, rather than to the  $d_{x^2-y^2,z^2}$  orbitals, directed to the centres of the faces of the cube.

If the atomic orbitals of M and L are classified according to their symmetry properties, we get :

TYPE OF ORBITAL	NUMBER OF ORBITALS	REPRESENTATION
M 3d	5	$e + t_2$
M 4s	1	$a_1$
M 4p	3	$t_2$
L 2s	4	$a_1 + t_2$
L 2p pointing to M - $2p_k$	4	$a_1 + t_2$
L 2p perpendicular to M - L bond $2p_i$ and $2p_m$	8	$e + t_1 + t_2$

Table V.1

Representation of the atomic orbitals of M and L according to the point group  $T_d$

The determination of the molecular orbital energies can be greatly simplified if it is considered that the Hamiltonian operator commutes with the various symmetry operations, such as reflection or rotation. Therefore, the only atomic orbitals which have to be considered as interacting are those belonging to the same irreducible representation.

a<sub>1</sub> representation

Only three types of orbitals will interact according to this representation : the 4s orbital of the chromium and the 2s and 2p<sub>k</sub> orbitals of the oxygen. Since four oxygen atoms are involved, the resulting functions, which interact with each other in order to produce three molecular orbitals will be :

Cr 4s orbital;

$$\Phi_1 = \frac{1}{2} (O_1 2s + O_2 2s + O_3 2s + O_4 2s) \quad ; \quad (V.2)$$

$$\Phi_2 = \frac{1}{2} (O_1 2p_k + O_2 2p_k + O_3 2p_k + O_4 2p_k) \quad ; \quad (V.3)$$

where each individual ligand atom is distinguished by the subscripts 1 to 4.

t<sub>2</sub> representation

The orbitals which transform according to this representation may give rise to two types of bonding ( $\sigma$  and  $\pi$ ). Within any degenerate representation, the component functions will be orthogonal. In the case of any trio of functions which transform as t<sub>2</sub> (under T<sub>d</sub> configuration), it will be possible to identify them as members of three orthogonal subgroups. In the case of tetrahedral complexes of the transition metals, each subgroup will have four members. If we consider the 4p<sub>x</sub> orbital of the central atom, for instance, each of the four 2p<sub>k</sub> orbitals of the ligands will have the same amount of overlap with this orbital, and

will enter into the combination with the same coefficient, with the appropriate sign (see Figure V.1a).

The overlap of the ligand  $2p_k$  orbitals with the metal  $d$  orbitals may also be investigated in the same way. The metal  $3d_{xy}$  orbital has its lobes directed through the edges in the  $xy$  plane. This is represented in Figure V.1b by the appropriate  $+$  and  $-$  signs in these edges. It can be seen that the  $2p_k$  ligand orbitals overlap with the  $d_{xy}$  metal orbital in precisely the same way as they do for the  $4p_z$  orbital, except that all the signs are reversed.

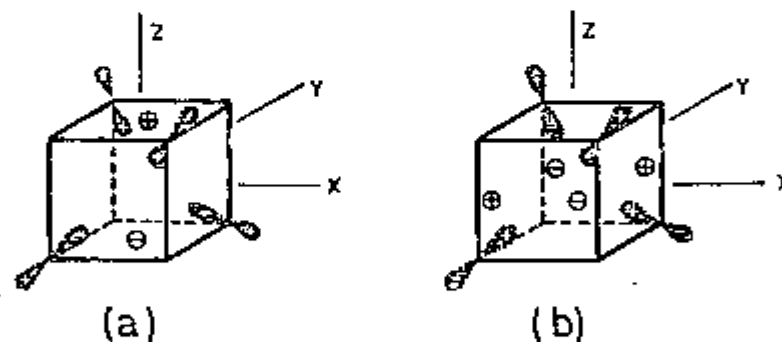


Figure V.1

Overlap of ligand  $2p_k$  orbital with metal  $p$  and  $d$  orbitals

Concisely, the  $4p_z$  orbital of the central atom may be combined with the  $3d_{xy}$  orbital of the same atom, and the  $2s$  and  $2p_k$  orbitals of the ligand atoms. The set of resulting functions, in this case, will be :

Cr  $4p_z$  orbital;

Cr  $3d_{xy}$  orbital;

$$\Phi_3 = \frac{1}{2} (O_1 2s + O_2 2s - O_3 2s - O_4 2s) \quad ; \quad (V.4)$$

$$\Phi_4 = \frac{1}{2} (O_1 2p_k + O_2 2p_k - O_3 2p_k - O_4 2p_k) \quad . \quad (V.5)$$

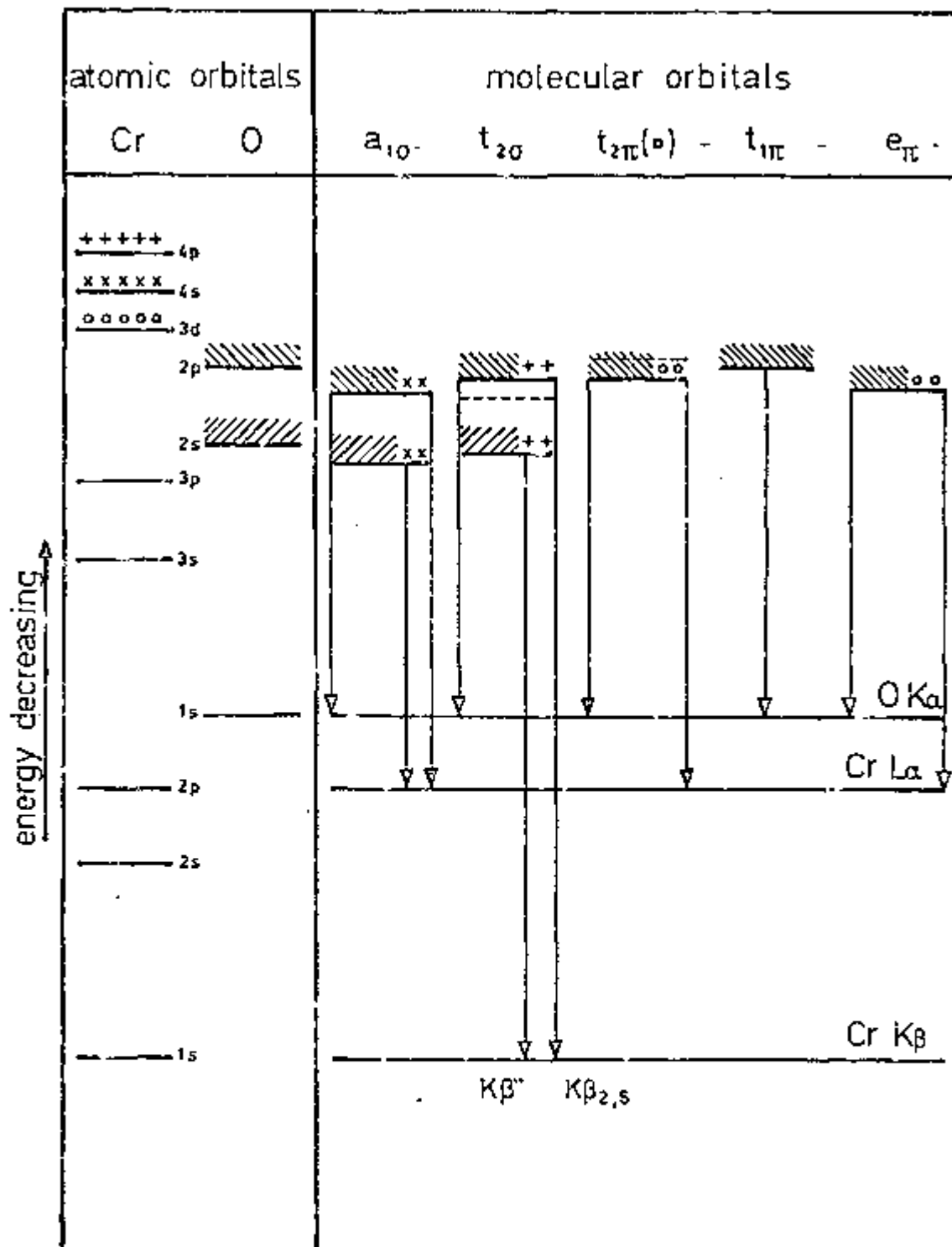
In principle, all the metal-atom d orbitals which transform as  $t_2$ , as well as the p orbitals, can enter into  $\pi$  bonding with the ligand atoms. The overlap of the central-atom p orbitals and the  $p\pi$  orbitals of the ligand atoms, however, will be very poor. The  $\pi$  bonding will then be predominantly of the type  $d\pi - p\pi$ , with only a small contribution from the chromium 4p orbitals.

#### e representation

The p ligand orbitals with e symmetry can interact with the chromium  $3d_{x^2-y^2, z^2}$  functions which belong to the same symmetry. Such an interaction will be very similar to the  $d\pi - p\pi$  type of the  $t_2$  symmetry and a pair of bonding and antibonding orbitals will be formed.

#### $t_1$ representation

The  $p\pi$  orbitals of the ligand atoms are the only ones which belong to this representation. This set of ligand orbitals will therefore constitute a group of non-bonding functions and will play no part in bond formation.



(\*) some mixing was considered here between the  $t_{2g}$  and  $t_{2g}$  molecular orbitals

Figure V.2

Representation of the occupied molecular orbitals in the chromate anion

Having in mind what has been discussed above, we can draw a qualitative molecular orbital diagram for the chromate ion (Figure V.2), with some of the possible X-ray emission transitions. Since the  $t_{2g}$  bond has a node where the  $t_{2\pi}$  bond has a maximum, the interaction between these orbitals should be very poor. Even so, we could consider the possibility of a very small interaction which might then result in the  $t_{2\pi}$  molecular orbital being less tightly bound than the  $t_{1g}$  non-bonding orbital. In the next section we shall try to assign each of the molecular orbitals present in Figure V.2 with all the XPS and XRES spectra obtained for the chromate ion.

#### V.3.1.1 Experimental Results

In Figure V.3 is depicted the LA emission spectrum obtained for the chromate ion using a soft X-ray tube as a source of excitation. As the penetration power of this tube is not so effective as in the case of the sealed X-ray tube, the outer layers of the target material (where any contamination may eventually be present) might play a rather relevant rôle. In order to be sure about the reliability of the experimental results, the LA spectrum was repeated under the same experimental conditions, but using the chromium-sealed tube instead of the CGR elent 10 soft X-ray tube. The spectra are shown in Figure V.3. The sample 1 spectrum was obtained by using the CGR elent 10 soft X-ray tube, whereas those for the samples 2 and 3 were obtained with the chromium-sealed X-ray tube. For the sample 3 we have used the same conditions adopted for the sample 2, the only difference being the superimposition of an extra



collimator in the X-ray path, between the primary collimator and the analysing crystal. Although the resolution achieved was considerably better in the latter case, the general features of the curve were not drastically changed, showing no evidence of surface decomposition.

The relevant XPS and XRES spectra obtained for  $\text{Na}_2\text{CrO}_4$  are shown in Figure V.4. Although the spectra depicted are concerned with  $\text{Na}_2\text{CrO}_4$ , experimental results were also pursued for potassium and lead chromates and it was verified that the nature of the cation has very little influence upon the spectra.

The spectra obtained in the present work for the chromate anion (Figure V.4) are indeed quite different in appearance from that obtained by Haycock (1978) for the sulphate ion (Figure V.5), although the two anions should be expected to show similarity, as they have the same symmetry, and the bonding involves, in principle, orbitals of the same type. The XPS valence band spectrum in the latter presents at least two emission peaks reasonably resolved. According to the molecular orbital diagram, these peaks (A and B in Figure V.5) were assigned to the  $2a_1$  and  $2t_2$  levels. In the case of our chromate ion, however, the valence band spectrum consists of one single peak (denoted by A in Figure V.4). Prins et al (1972) and Wertheim et al (1973), on the other hand, measuring the X-ray photoelectron spectra of both valence region and O 2s for the chromate ion, obtained two peaks whose shapes, relative intensity and FWHM are indeed very close to ours (A and B, respectively, in Figure V.4).

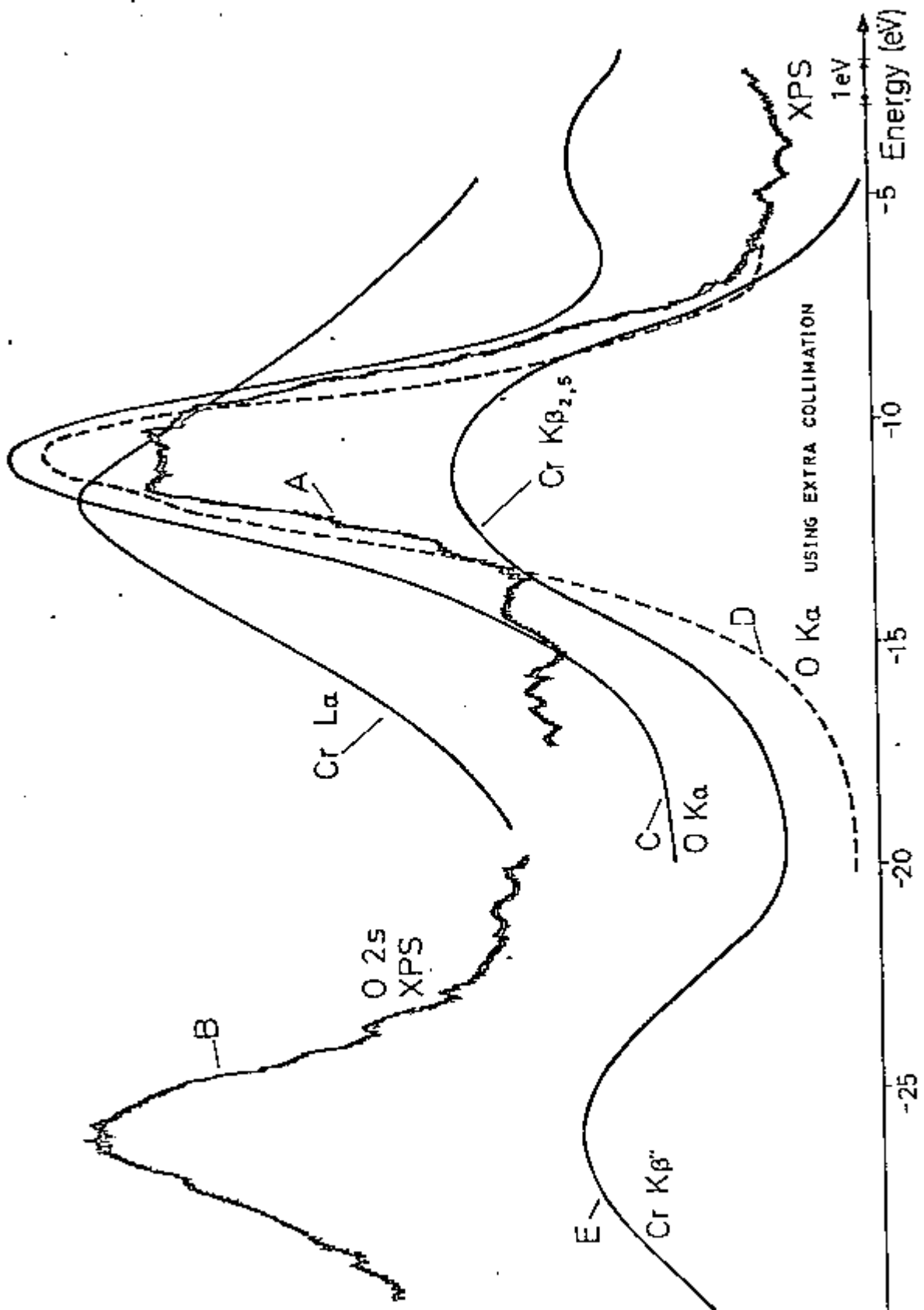


Figure V.4

X-ray emission data for the chromate anion

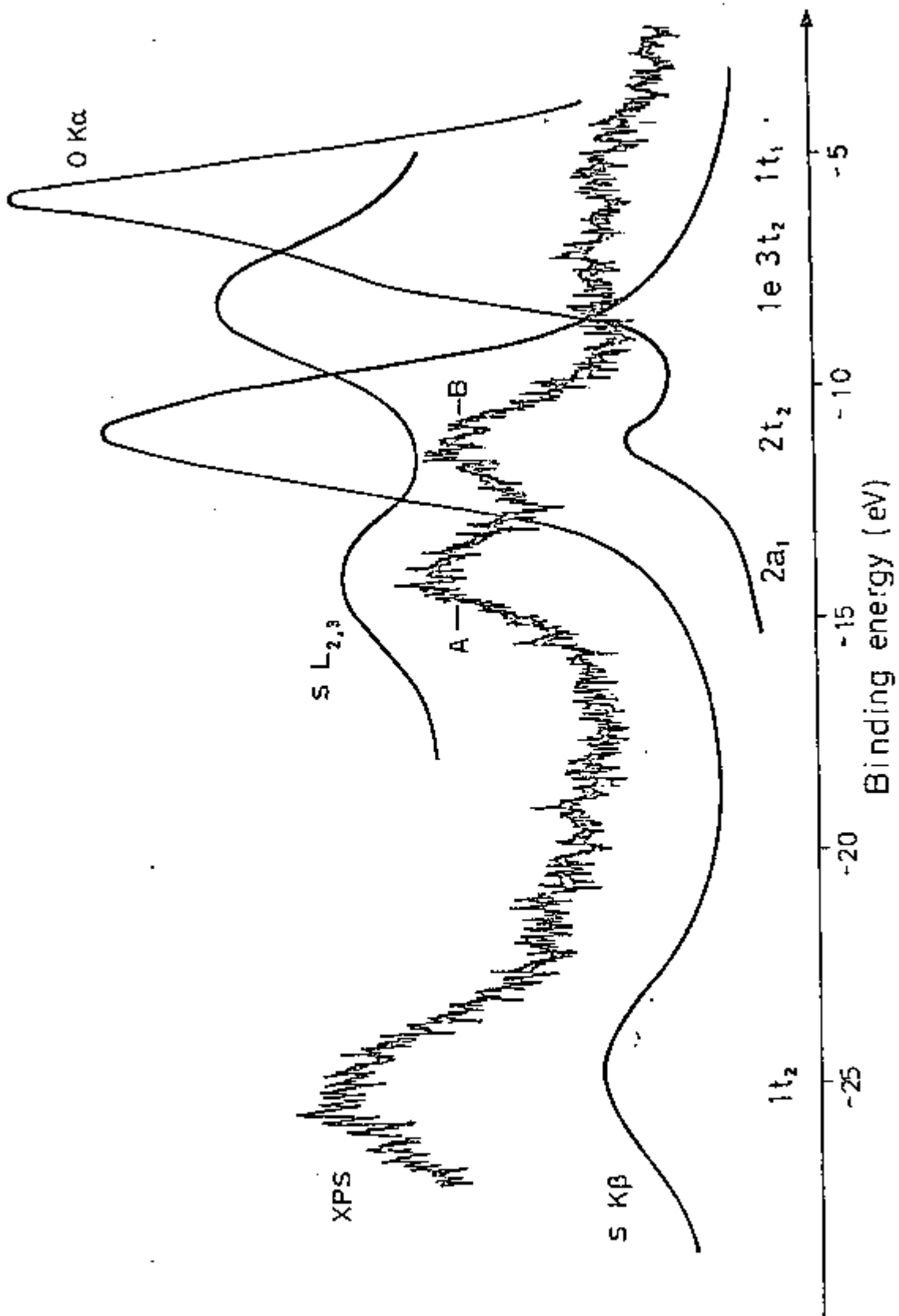


Figure V.5

X-ray data for the sulphate anion  
 (from Haycock, 1978; Dolenko et al, 1974)

With regard to the lining up of all the experimental spectra, a good agreement was found between our results and Fischer's, although using different techniques as a basis of alignment.

Having in mind all the chromate spectra obtained in the present work (Figure V.4), we shall firstly try to assign each emission band to any possible molecular orbital level. We shall then attempt to compare our results with those obtained theoretically (Clack, 1972; Hillier et al, 1971; Cleary et al, 1965; Viste et al, 1964) and experimentally (Fischer, 1971; Kurmaev et al, 1979; Mazalov, 1977; Sadovskii et al, 1975), as well as to discuss the possible observed discrepancies.

The O 2s XPS spectrum is aligned with the Cr  $K\beta$  emission band (peaks B and E, respectively, in the same Figure V.4). We can therefore position in this region the molecular orbitals which present a high percentage of O 2s in their composition, that is,  $1a_1$  and  $1t_2$ . The five remaining orbitals (that is,  $2a_1$ ,  $2t_2$ ,  $1e$ ,  $3t_2$  and  $t_1$ ) can be positioned under the XPS valence band spectrum (peak A) and the O  $K\alpha$  emission (peaks C or D). Except for the  $t_1$  orbital, which is entirely formed by the oxygen 2p "lone-pairs", all the other orbitals should be present in some extent in the Cr L $\alpha$  band. Since the  $2t_2$  and  $3t_2$  are the only orbitals presenting in their composition some amount of Cr 4p, these two orbitals should be aligned with the Cr  $K\beta_{2,5}$  band, as well.

In the lining up of all the spectra available, it is found that the Cr L $\alpha$  band has a considerable emission on the

high-energy side, which corresponds to no appreciable emission in the XPS or in any other spectrum, like O K $\alpha$ . It is difficult to be sure about the relevance of any corresponding emission present in the XPS spectrum, since it seems to be greatly influenced by the position where we locate the background level. We should therefore expect in this region an orbital whose composition has almost none contribution from the O 2p atomic orbital. There are, of course, some difficulties in the interpretation of such a short-wave sub-band on the basis of MO-LCAO theory. The possibility of an interaction between the  $t_{2\pi}$  and  $t_{2\sigma}$  orbitals, shown in Figure V.2, could make the  $t_{2\pi}$  less tightly bound than the  $t_1$  non-bonding orbital. This could provide a "one-electron" solution for the Cr L $\alpha$  short-wave emission, although it does not explain why we do not have any corresponding emission in the other spectra. Before we proceed with the discussion of the experimental results, however, we shall try to compare them with the electronic structure calculations.

The energies, symmetry designations and orbital components of the valence molecular orbitals used in Clack's calculation are shown in Table V.2. According to him, the highest filled orbitals are  $1t_1$ ,  $2a_1$  and  $3t_2$ , mainly of oxygen non-bonding 2p character. Metal-oxygen bonding occurs mainly through the  $1e$  and  $2t_2$  which are closely spaced.

ORBITAL ENERGY (eV)	SYMMETRY	ATOMIC COMPOSITION (%)				
		Cr ORBITAL			O ORBITAL	
		3d	4s	4p	2s	2p
+ 2.27	1t <sub>1</sub>					100.00
+ 0.46	2a <sub>1</sub>		6.07		3.20	90.74
- 0.81	3t <sub>2</sub>	2.03		7.46	6.48	84.01
- 2.83	1e	30.51				69.49
- 4.19	2t <sub>2</sub>	36.54		3.29	0.02	60.14
-21.89	1t <sub>2</sub>	3.78		17.14	77.79	1.27
-23.65	1a <sub>1</sub>		22.80		77.19	0.18

Table V.2

Molecular orbitals for chromate ions (from Clack, 1972)

An O 2s atomic orbital contribution in molecular orbitals which are predominantly O 2p in character, was found in the theoretical calculations of Clack (1972) and Hillier et al (1971). This contribution will, of course, be relevant in the XPS valence band intensity, since the photoionization cross section is greater for the O 2s electrons than for the O 2p electrons. From Table V.2, and the theoretical results of the photoionization cross sections (Scofield, 1976), the ratio of relative intensities for XPS peaks O 2s/VB was calculated to be 3.82 : 1. Bearing in mind this theoretical value, and comparing it with the intensities obtained in the present experimental work (2550 cps and 1100 cps for the O 2s and valence band, respectively), it is realized that the intensity of the XPS valence-band peak cannot be explained as solely due to O 2p and Cr 3d. Some additional amount of O 2s (~12%) must be taken into account in the valence-band peak, in order to

explain its high relative intensity.

Considering the contribution of Cr 3d, 4s and O 2p atomic orbitals in the final molecular orbitals, the Cr L $\alpha$  and O K $\alpha$  emission spectra can be drawn (see Figure V.5). The X-ray experimental results of Figure V.4 do not agree well with the theoretical calculations. The O K $\alpha$  theoretical emission spectrum (FWHM  $\sim$  8.5 eV) is spread over a larger energy range than our experimental curve (FWHM  $\sim$  3.5 eV), whereas the trend for the Cr L $\alpha$  is the opposite (FWHM of 4.0 eV and 7.0 eV, respectively). Major differences are also found in the positioning of all the molecular orbitals in both cases. According to the calculations, the  $t_1$  non-bonding orbital (whose composition has to be 100% O 2p) is lying highest in energy than the occupied set. From the experimental results, however, this is not seen to be true, if we consider that the emission present on the high-energy side of the Cr L $\alpha$  is connected with some of the five occupied levels.

Fischer (1971) suggested that the main intensity maximum of the Cr L $\alpha$  spectrum was due to the  $1e$  MO  $\rightarrow$  Cr  $2p_{3/2}$  transition, and the short-wave emission was connected with the  $3t_2$  MO  $\rightarrow$  Cr  $2p_{3/2}$  transition. Clack (1972) has attempted to explain this by considering the way in which X-ray transitions are originated. Whilst the Cr K $\beta_{2,5}$  and Cr L $\alpha$  lines originate from transitions to core levels very close to the nucleus (1s and 2p, respectively), the O K $\alpha$  spectrum arises in transitions to the 1s level, which is more susceptible to the valence electrons. Clack therefore assumed that the exchange integral would be

greater in the latter transition (O K $\alpha$ ), causing a shift of the spectrum to lower energies. Still according to him, all the levels derived from the O K $\alpha$  spectrum should be shifted to higher energies in order to obtain a more realistic picture of the orbital energies. As the  $t_1$  level is the one which has the major percentage of O 2p character (100%), it should present the largest displacement to higher energies, and, therefore, occupy the highest filled level of the molecular orbital diagram. This explanation, however, does not seem very reasonable, for the simple reason that, if we do not believe in the experimental alignment of all the levels derived from O K $\alpha$  spectrum in the chromate example, we cannot be sure about the alignment for other oxy-compounds, as well. Furthermore, Clack's assumption does not explain satisfactorily the difference between the widths of the O K $\alpha$  curves obtained experimentally and theoretically.

Sadovskii et al (1975), on the other hand, associated the origin of the main peak with the  $2t_2$  MO  $\rightarrow$  Cr  $2p_{3/2}$  transition, and that of the short-wave band with the  $1e$  MO  $\rightarrow$  Cr  $2p_{3/2}$  transition. None of these assignments (given by Fischer, 1971, and Sadovskii et al, 1975), however, seems reasonable to us, for the simple reason that we do not have any relevant corresponding emission in the XPS or O K $\alpha$  spectra. These assignments also do not agree well with the theoretical calculations of Clack (1972), who found that the  $2t_2$ ,  $1e$  and the  $3t_2$ ,  $1e$  molecular orbitals are close in energy.



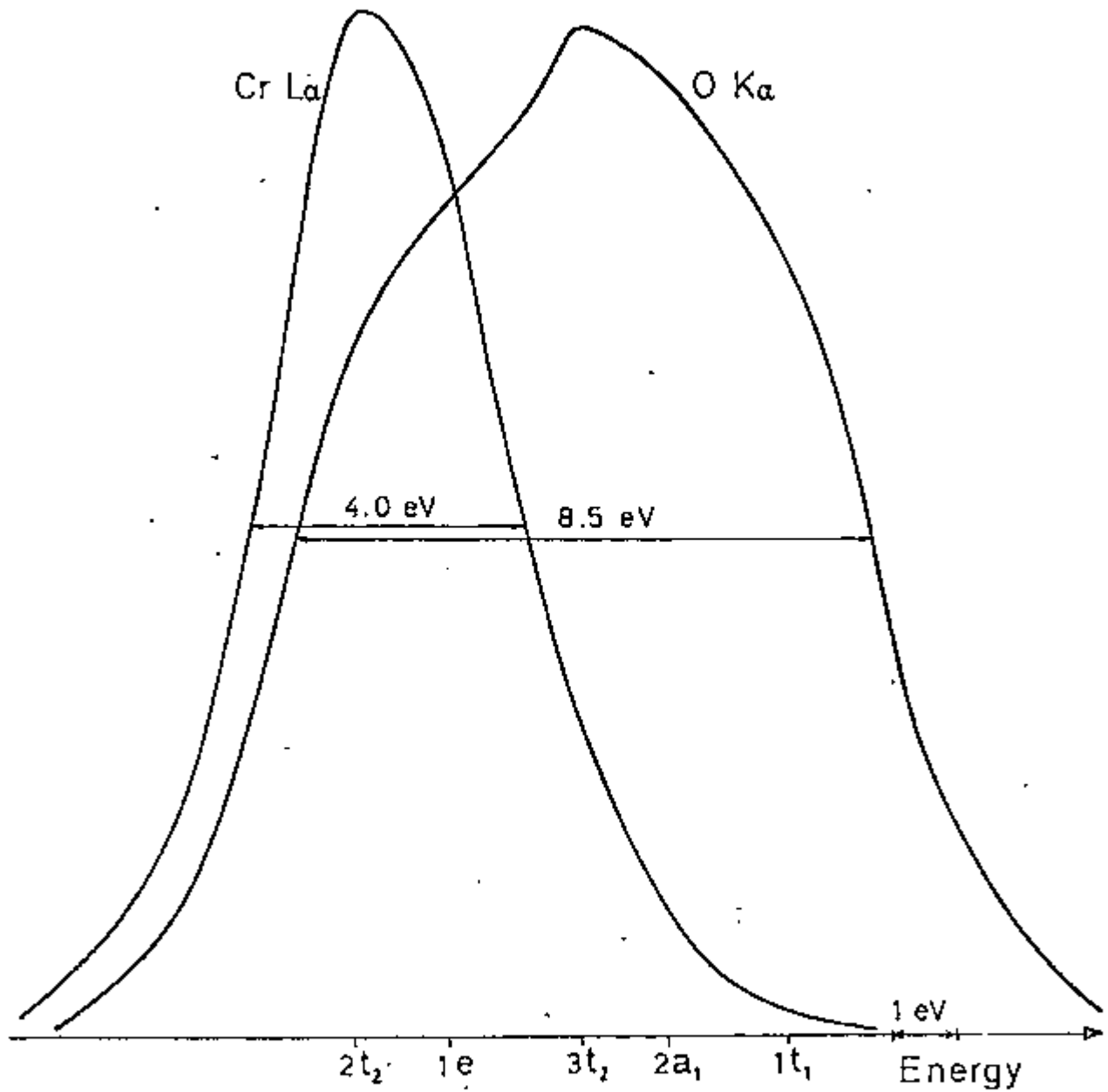


Figure V.6

Chromate O K $\alpha$  and Cr L $\alpha$  curves

(from the theoretical calculations of Clack, 1972)

The above discussion has shown that the interpretation of the experimental results is not straightforward. We shall next try to discuss the problem following different approaches, assuming that the theoretical calculations give the correct ordering of molecular orbitals. One possible interpretation connects the existence of such a short-wave emission with excited states (Kurmaev et al, 1979). In this case one of the empty levels (orbital  $2e$ , for instance) might be populated during X-ray spectra generation when an electron is excited to this orbital (i.e., "shake-up"). This electron would then decay to the metal  $2p_{3/2}$  level, giving rise to X-ray emission. Thus, it is possible that the low-energy emission of the metal L spectra of oxy-anions is due to  $1e, 2t_2, 3t_2, 2a_1$  MO  $\rightarrow$  Cr  $2p_{3/2}$  transitions and the short-wave band to  $2e^*$  or  $4t_2^*$  MO  $\rightarrow$  Cr  $2p_{3/2}$  transitions. The fact that we do not have any relevant corresponding emission in the XPS valence-band spectrum strengthens the above interpretation. The absence of any emission in the O K $\alpha$  spectrum (due to the  $2e^*$  or  $4t_2^*$  MO  $\rightarrow$  O  $1s$  transition), however, can be satisfactorily explained only if we assume that one of these orbitals have a very small contribution from the O  $2p$  atomic orbital. The corresponding  $1e$  or  $2t_2$  bonding orbitals could indeed be aligned to the emission present on the low-energy side of the Cr L $\alpha$  spectrum (see Figure V.4) which corresponds to a very weak peak in the XPS valence band and a tail in the O K $\alpha$  spectrum.

A second interpretation for the short-wave emission in the Cr L $\alpha$  spectrum takes into account the crossover transition theory of O'Brien and Skinner (1940). The higher-

energy sub-band of the Cr L $\alpha$  spectrum, nominally arising from Cr 3d,4s  $\rightarrow$  Cr 2p $_{3/2}$  transitions, could be assigned to a 1t $_1$   $\rightarrow$  Cr 2p transition, although neither the Cr 3p nor 4s orbitals belong to this representation. This latter approach does not agree with the normal assumption that the selection rules governing X-ray emission are atomic in nature, i.e., for L spectra the upper level must be an s or d state. On the contrary, it assumes that the correct selection rules are actually molecular in nature, i.e., determined by the T $_d$  point group. In this case, since the hole in the Cr 2p level (initial state) and the dipole moment operator are both of t $_2$  character, the allowed upper states can have a $_1$ , e or t $_1$  symmetries. The use of molecular selection rules admits the possibility that the highest filled orbital is in fact the 1t $_1$ , and therefore allows the participation of this orbital in the transition that gives origin to the higher-energy Cr L $\alpha$  sub-band (Tossell et al, 1974). We can make the general assumption that in cases in which the upper atomic levels normally involved in the X-ray transitions are essentially empty (e.g. Cr 3d and 4s in the chromate ion), absolute spectral intensities are reduced and transitions forbidden by atomic selection rules, but weakly allowed by the molecular selection rules, can generate appreciable relative intensity and, therefore, yield spectral features. For this approach to be correct, we should expect approximately the same width for O K $\alpha$  and Cr L $\alpha$  spectra. Nevertheless, experimental results (FWHM of 3.5 eV and 7.8 eV for O K $\alpha$  and Cr L $\alpha$ , respectively) do not agree well.

Another interpretation for the origin of such a short-wave sub-band emission considers the possibility of a transition from a doubly-ionized state. If, by some mechanism, a core Cr 2p electron were to be ejected at the same time of a less tightly bound electron, a doubly-ionized species would be obtained. The energy levels in this type of doubly-ionized species would, of course, be different to the energy levels in the singly-ionized species, giving rise to transitions at higher energy values. These high-energy satellites could, in principle, provide an explanation for the origin of the short-wave emission in the Cr L $\alpha$  spectrum, although it is not clear why we do not have any corresponding feature on the low-energy side of the XPS valence band spectrum.

As a final approach, we can consider that the approximation implied by Koopman's theorem, which has been used so far with good results, does not hold true for the chromate anion. In other words, the electrons in the chromate are being affected by the excitation of the sample and consequent creation of vacancies in core levels.

### V.3.2 The Chromium (VI) Oxide and the Dichromate Ion

The complete set of spectra obtained for the chromium (VI) oxide and the potassium dichromate are depicted in Figures V.7 and V.8, respectively. Dichromates result from the sharing of vertices between limited numbers of CrO<sub>4</sub> tetrahedra. In potassium dichromate the anion has the structure shown in Figure V.9a, where the bridging Cr - O bonds are much longer (1.79 Å) than the terminal ones, wit

mean 1.63 Å (Wells, 1975). The chromium (VI) oxide is built of infinite chains formed by the linking of  $\text{CrO}_4$  tetrahedra, by sharing two corners (Figure V.9b). Chromium in the oxide as in the dichromate is therefore approximately tetrahedrally coordinated. This tetrahedron, however, becomes more and more distorted as we progress from chromate to dichromate to  $\text{CrO}_3$ . As both  $\text{CrO}_3$  and dichromate have basically the same configuration as the chromate, we should expect, in principle, similar X-ray emission spectra, but for a considerable broadening of the related bands due to the symmetry distortion. This broadening, if any, should be visible in the O K $\alpha$  spectrum, since we have an increase in the number of bridging oxygens as we go from chromate to dichromate and to  $\text{CrO}_3$ . In practice, however, no appreciable change is observed in the width of the O K $\alpha$  spectra related to the mentioned compounds. The oxygen K $\alpha$  spectrum and the chromium K $\beta_{2,5}$  can be lined up with the XPS valence band in the same way as for the chromate anion. But problems arise if the Cr L $\alpha$  spectra are compared with each other. In  $\text{CrO}_3$ , the Cr L $\alpha$  spectrum presents short and long-wave sub-bands which correspond to a very weak emission in the XPS valence band, and to nothing in the O K $\alpha$  spectrum. The same feature in the L $\alpha$  spectrum is also visible in the dichromate ion. Although the problem is similar to that of the chromate ion, already presented in section V.3.1.1, it is seen that the structure is even more pronounced in the case of both  $\text{CrO}_3$  and dichromate. In all the spectra there is evidence of Cr 3d character in bonding molecular orbitals which are mainly oxygen in character.

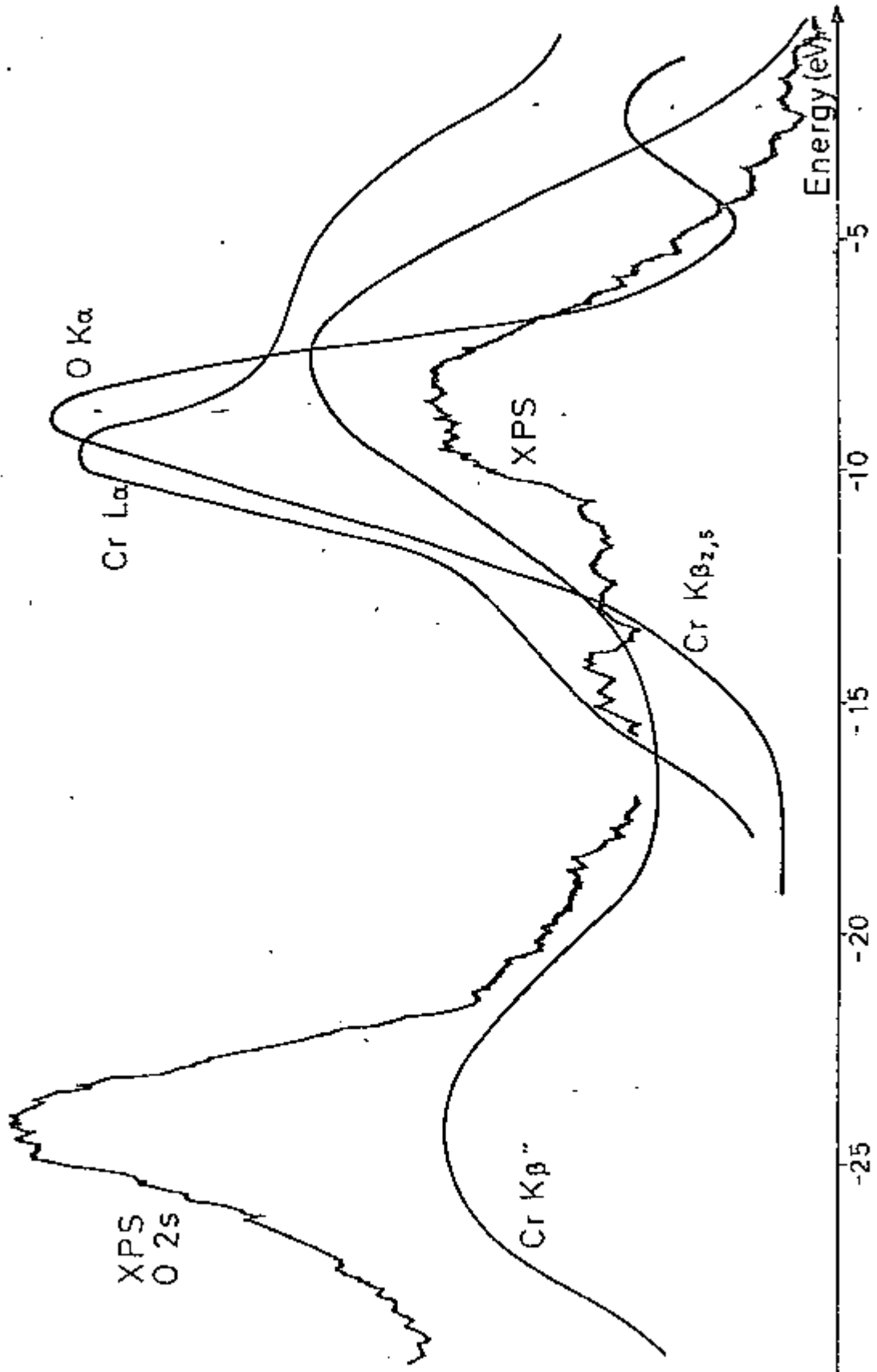


Figure V.7  
X-ray data for  $\text{CrO}_3$

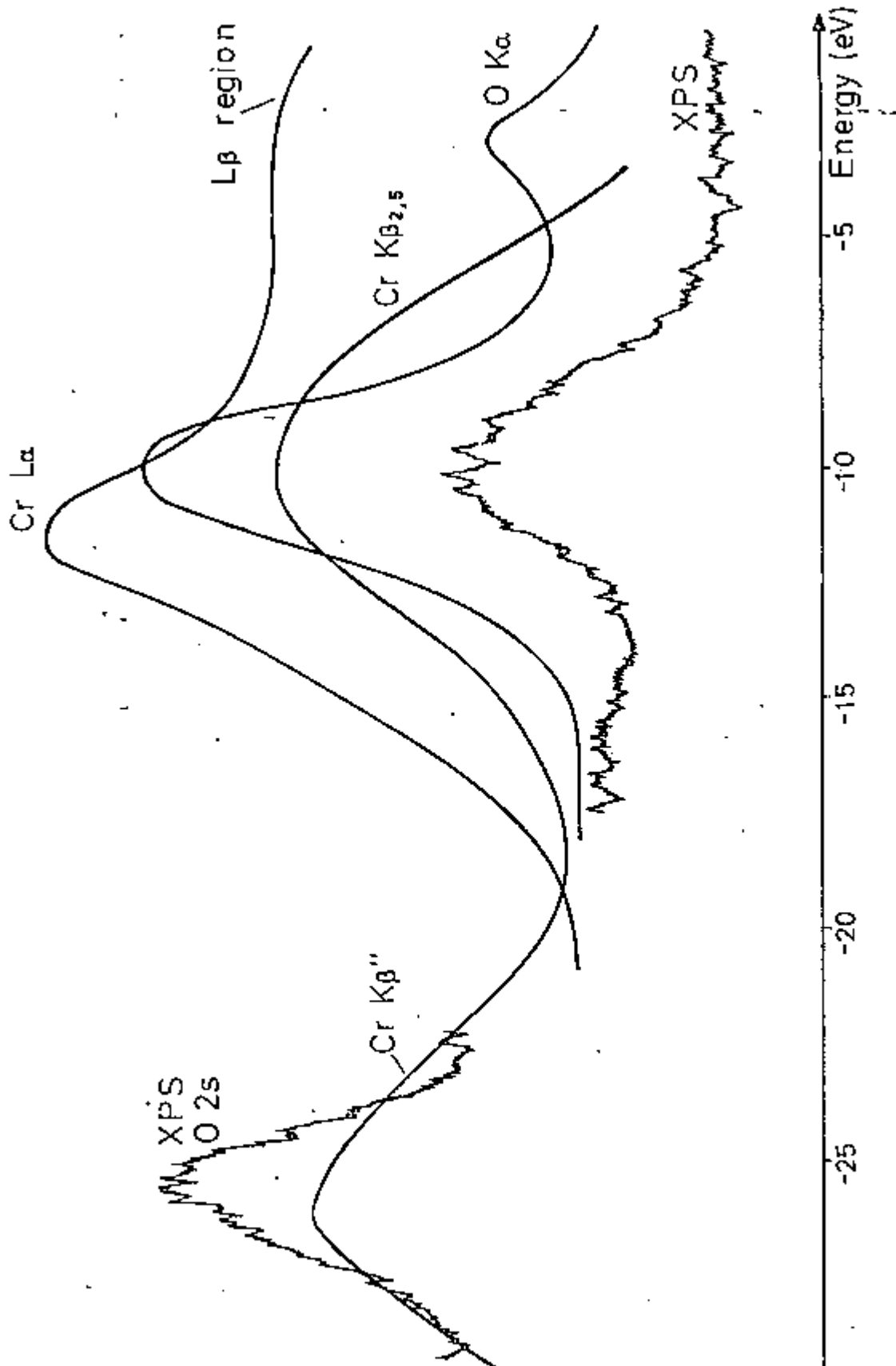
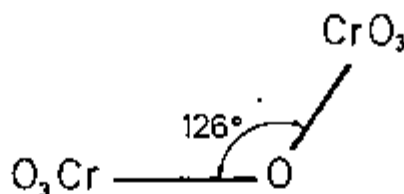
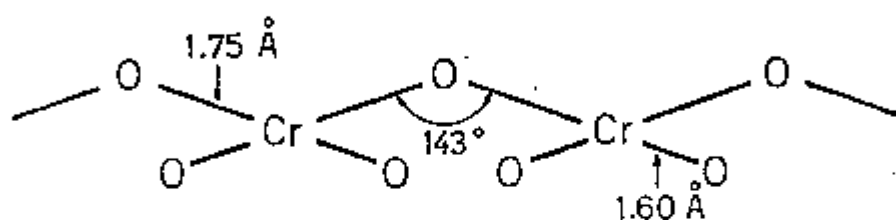


Figure V.8  
X-ray data for  $K_2Cr_2O_7$



(a) Potassium dichromate structure



(b) Chromium trioxide structure

Figure V.9

Even though difficult to interpret the chromate and related compounds using the one-electron model (see section V.3.1.1), it is possible to investigate the relative intensity of the various L $\alpha$  peaks, in order to try and estimate the amount of 3d character present in molecular orbitals with oxygen. If we compare the intensity of the Cr L $\alpha$  spectrum obtained for these compounds with the same peak for Cr $_2$ O $_3$  (namely a Cr 3d $^3$  compound), we can have an estimate of the number of electrons that are taking part in the bond formation. In Table V.3 the Cr L $\alpha$ /O K $\alpha$  intensity ratios obtained for different chromium compounds are



depicted. This ratio was obtained by taking into account the chemical composition, that is, the percentual weight of each individual element (Cr and O, respectively) in the compound. Since the intensity of O K $\alpha$  is expected to be constant, the ratio variation should roughly provide an indication of the number of 3d electrons taking part in the bond formation. It is therefore seen, from Table V.3, that the 3d electrons participation in molecular orbitals mainly O 2p in character is more pronounced in the CrO<sub>3</sub> and dichromate ion than for the chromate ion.

CHROMATE	0.16
DICHROMATE	0.46
CrO <sub>3</sub>	0.39
Cr <sub>2</sub> O <sub>3</sub>	0.78

Table V.3

Cr L $\alpha$ /O K $\alpha$  intensity ratio

### V.3.3 The Chromium (III) Oxide

The Cr<sub>2</sub>O<sub>3</sub> system can be treated as a 51-electron problem arising from an isolated Cr<sup>III</sup>O<sub>6</sub> species. The chromium (III) oxide has an hexagonal close-packed array of oxide ions in which six oxygen atoms form an octahedral group around the metal atom, and each oxygen atom is surrounded by four metal atoms (Newnham et al, 1962). For convenience, the six ligands can be considered as entering

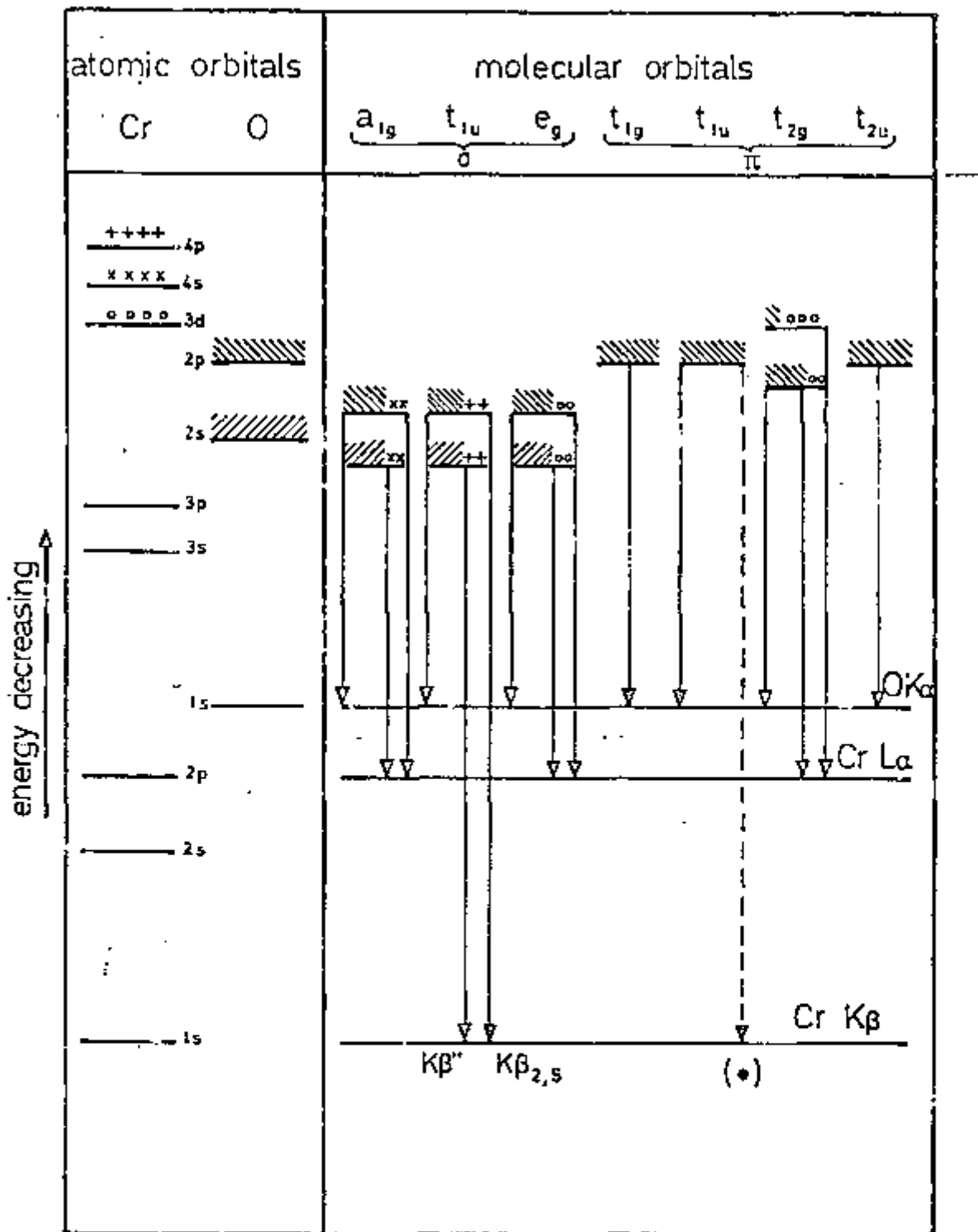
along the axes of the coordinate system. Under these conditions they will strongly interact with the  $d_z^2$  and  $d_{x^2-y^2}$  orbitals lying along the x, y and z axes. The complete classification of the atomic orbitals of the central atom (M) and of the ligand atoms (L), according to their symmetry properties, is given in Table V.4.

TYPE OF ORBITAL	NUMBER OF ORBITALS-	REPRESENTATION
M 3d	5	$e_g + t_{2g}$
M 4s	1	$a_{1g}$
M 4p	3	$t_{1u}$
L 2s	6	$a_{1g} + t_{1u} + e_g$
L 2p pointing to M	6	$a_{1g} + t_{1u} + e_g$
L 2p perpendicular to M - L bond	12	$t_{1g} + t_{2g} + t_{1u} + t_{2u}$

Table V.4

Representation of the atomic orbitals of M and L according to the point group  $O_h$

The  $t_{1u}$  (4p) and  $e_g$  (3d) orbitals are directed towards the ligands and are used to form strong sigma bonds. The  $t_{2g}$  metal 3d orbitals, on the other hand, are directed between the approaching ligands and will interact, forming  $\pi$  bond, with all the ligand orbitals belonging to the same irreducible representation. The  $t_{1g}$  and  $t_{2u}$  orbitals formed from the twelve appropriate atomic orbitals of the ligand atoms must remain non-bonding for the simple reason that there are no  $t_{2u}$  and  $t_{1g}$  orbitals in the central atom.



(\*) indicates X-ray transition arising as a result of  $\sigma-\pi$  mixing

Figure V.10

Representation of the occupied molecular orbitals in the chromium (III) oxide

In Figure V.10 a qualitative molecular orbital energy level diagram for the chromium (III) oxide is depicted, including an approximate indication of the atomic orbital character that might be present in each molecular orbital. In the following section, the experimental results obtained for the chromium (III) oxide is presented, as well as a discussion of the molecular orbitals involved in each emission.

### V.3.3.1 Experimental Results

The  $\text{Cr}_2\text{O}_3$  XPS spectrum is shown in Figure V.11. Also shown, in the same energy scale, are the positions and relative intensities of the various components present in the Cr  $K\beta_{2,5}$ , Cr  $K\beta''$ , Cr L $\alpha$  and O K $\alpha$  emission spectra.

From the calculations of the electronic band structure for  $\text{Cr}_2\text{O}_3$  carried out by Clack (1972) (see Table V.5), the Cr L $\alpha$  and O K $\alpha$  emission spectra were drawn. The theoretical curves obtained are depicted in Figure V.12. These curves are in better agreement with our experimental results than they were in the case of the chromate ion. It can be observed from Table V.5 that the orbital energy values calculated are higher than expected, probably due to the theoretical model chosen by Clack ( $\text{CrO}_6^{9-}$ ). From the molecular orbital representation (Figure V.10), we can assume that the Cr L $\alpha$  emission band is composed of peaks originating in the  $1t_{2g}$ ,  $2t_{2g}$  and  $2e_g$  orbitals. As the  $2t_{2g}$  is the orbital which is partially filled, it will be the one lying highest in energy. Clack assigned to this orbital 76% of contribution from the Cr 3d, whereas the  $2e_g$  and  $1t_{2g}$

orbitals have 18% and 24%, respectively, of Cr 3d character. The Cr L $\alpha$  will presumably have some intensity from transitions originated in the 2a $_{1g}$  orbital, which Clack calculated as having 11% 4s character. This contribution, however, does not appear to be present as a distinct feature in the L $\alpha$  spectrum.

ORBITAL ENERGY (eV)	SYMMETRY	ATOMIC COMPOSITION (%)				
		Cr ORBITAL			O ORBITAL	
		3d	4s	4p	2s	2p
53.43	2t $_{2g}$	76.40				23.60
51.10	3t $_{1u}$			1.73		98.27
49.87	1t $_{1g}$					100.00
49.55	1t $_{2u}$					100.00
49.13	2e $_g$	18.35				81.65
48.03	2a $_{1g}$		10.71		7.86	81.43
47.88	1t $_{2g}$	23.60				76.40
46.90	2t $_{1u}$			9.42	8.71	81.86
34.29	1e $_g$	2.21			97.19	0.60
27.50	1t $_{1u}$			20.87	77.15	1.99
25.40	1a $_{1g}$		24.95		34.30	0.75

Table V.5

Levels of valence molecular orbitals for Cr $_2$ O $_3$

(from Clack, 1972)

The XPS valence band spectrum consists of two distinct peaks. Peak C, of higher energy, is mostly 3d in character, since it is aligned with the main emission of the Cr L $\alpha$  band, it being therefore assigned to the 2t $_{2g}$  orbital. Peak D, lying lower in energy, is mostly O 2p in character, it

being mainly aligned with the O K $\alpha$  and Cr K $\beta_{2,5}$  emission bands. Seven valence molecular orbitals are primarily O 2p in character ( $2t_{1u}$ ,  $1t_{2g}$ ,  $2a_{1g}$ ,  $2e_g$ ,  $1t_{2u}$ ,  $1t_{1g}$  and  $3t_{1u}$ ). Of these, it is assumed that the  $1t_{1g}$  and  $1t_{2u}$  non-bonding 2p "lone-pairs" give rise to the main oxygen K $\alpha$  emission component (100% of O 2p character). Even the small contribution of 24% from the O 2p in the  $2t_{2g}$  orbital is evident in the O K $\alpha$  spectrum obtained using extra-collimation (see Figure V.11). The  $2t_{1u}$  and  $3t_{1u}$  are calculated to have some amount of Cr 4p character in their composition and are therefore assumed to give rise to the Cr K $\beta_{2,5}$  emission line.

The O 2s XPS spectrum (peak A in Figure V.11) is aligned with the Cr K $\beta''$  emission band (peak B in the same figure). In this region the orbitals which are mostly O 2s in character, that is,  $1a_{1g}$ ,  $1t_{1u}$  and  $1e_g$ , are found. According to Clack's calculations, the Cr 4p contribution was found to be greater for the  $1t_{1u}$  orbital (21%) than for the  $2t_{1u}$  and  $3t_{1u}$  (9% and 2%, respectively), this fact being in disagreement with the relative intensities obtained experimentally for the Cr K $\beta''$  and Cr K $\beta_{2,5}$  bands.

Still according to Clack's calculations, there is some contribution from the O 2s atomic orbital in two molecular orbitals which are predominantly O 2p in character. This contribution from the O 2s should also be visible in the intensity of our XPS valence band. We can compare the intensities experimentally obtained for the XPS O 2s peak and the XPS valence band spectrum (1800 cps and 850 cps, respectively) with the ratio of relative intensities

calculated from Table V.5, including the contribution of O 2s foreseen by Clack (O 2s : VB :: 3.63 : 1). We realize that indeed an even larger amount of O 2s (~13% more than already assumed) must be taken into account in the valence band peak to explain its high relative intensity, as in the case of the chromate ion.

Several authors (Adler et al, 1967a, 1967b; Morin, 1961) have suggested that the 3d electrons ( $t_{2g}$  symmetry) could give rise to two different kinds of bonding. One type would be related to the interaction between the chromium  $t_{2g}$  and oxygen  $p\pi$  electrons in the orbitals  $1t_{2g}$  and  $2t_{2g}$ . The other type would be formed by a direct cation-cation interaction, giving rise to a strong  $t_{2g} - t_{2g}$  covalent bonding between the chromium atoms. As a result of this bonding, the  $2t_{2g}$  orbital should split apart and therefore become non-degenerate. XPS peak C in Figure V.11, which corresponds to the  $2t_{2g}$  orbital, however, is too sharp (FWHM ~ 3.0 eV) to account for any possible splitting. Besides, the smallest distance between the chromium atoms (2.65 Å) is still too big to allow any extensive overlap of d orbitals from neighbouring  $Cr^{3+}$  ions, with ionic radius 0.55 Å (Cotton et al, 1966).

The above discussion was based in the assumption that the chromium (III) oxide is an isolated  $Cr^{III}O_6$  species, without considering the effect on the spectra caused by the oxygen bridging. This effect, if any, should be visible only as a band broadening in the O K $\alpha$  spectrum. Yet, the width of the O K $\alpha$  curve experimentally obtained (4.0 eV) is narrower than in the theoretical curve (5.0 eV in Figure V.12).

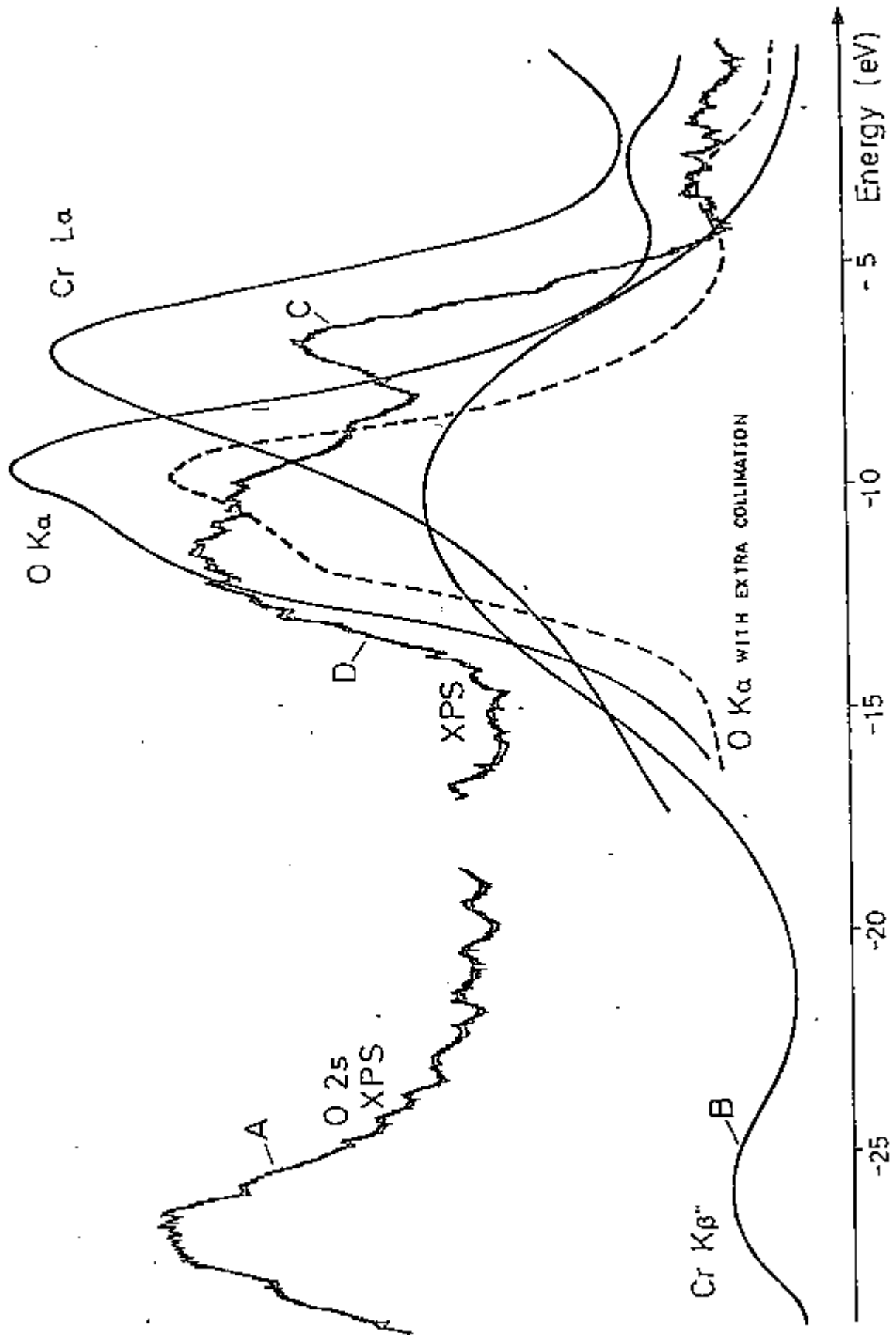


Figure V.11

X-ray emission data for  $\text{Cr}_2\text{O}_3$



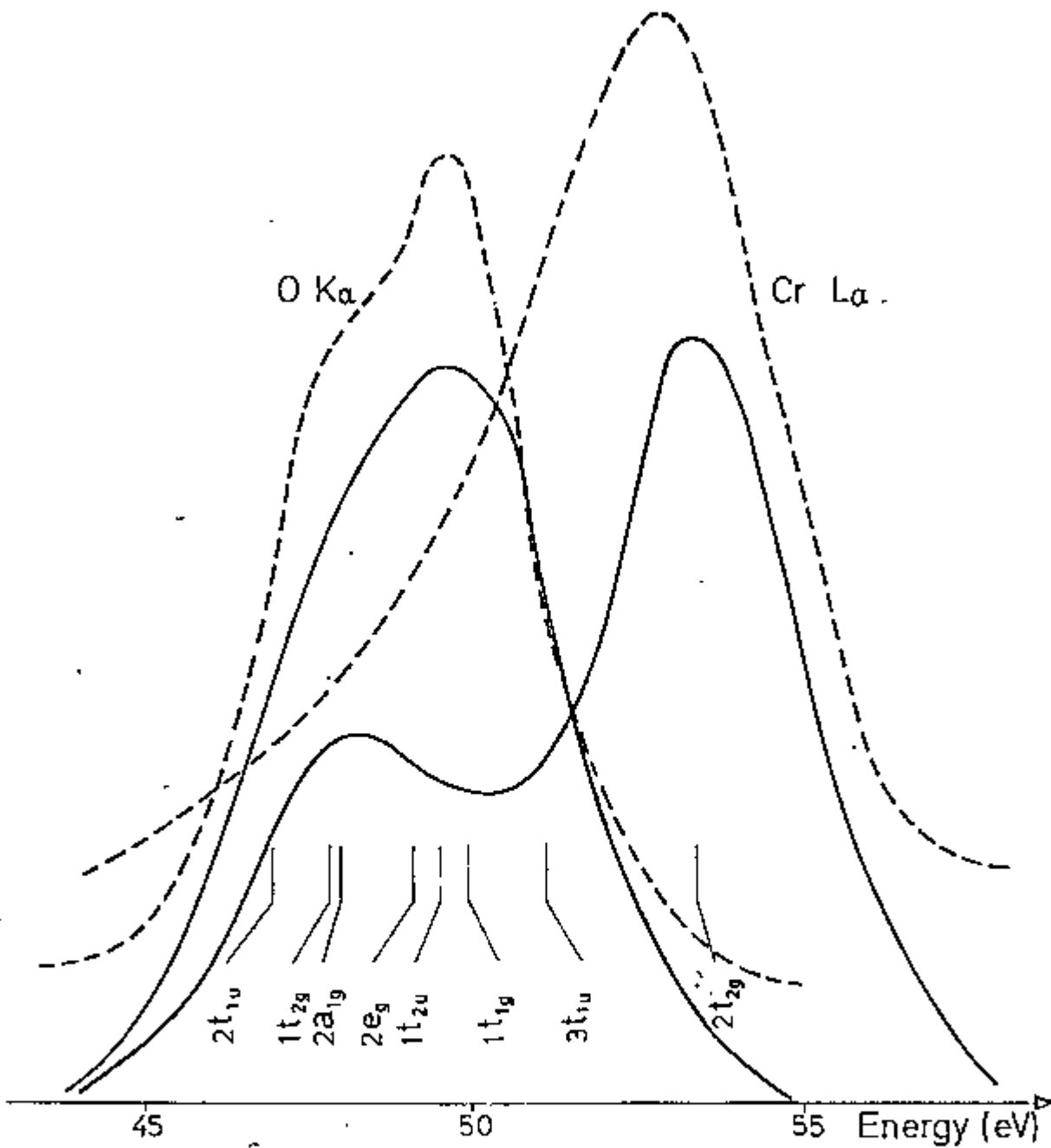


Figure V.12

$\text{Cr}_2\text{O}_3$  O K $\alpha$  and Cr L $\alpha$  curves from the theoretical calculations of Clack (1972). The dashed curves correspond to our experimental results

## 4 Bonding in Titanium and Vanadium compounds

### 4.1 Titanium Carbide

The XPS and XRES spectra obtained for the titanium carbide are shown in Figure V.13. The titanium carbide has a NaCl structure, in which each metal ion is octahedrally surrounded by six carbon atoms. Although the TiC does not have the same structure of  $\text{Cr}_2\text{O}_3$  outside the isolated  $\text{MO}_6$  species, we can assume that the schematic diagram of Figure 10 (for  $\text{Cr}_2\text{O}_3$ ) is applicable for TiC, as well. Of course, we do not have to consider here the transition which has its origin in the  $2t_{2g}$  orbital, since Ti in TiC has a  $d^0$  configuration. We should therefore expect that the major differences in the molecular orbital energy level diagrams would be due to the energies of the ligand 2p and 2s orbitals. In fact, there is a considerable decrease in the  $2p - 2s$  energy separation, as one goes from oxygen to carbon (15 eV and 6 eV, respectively). This decrease will move the resulting orbitals closer together, and the X-ray emission and spectra will therefore be spread over a smaller energy range.

The Ti  $K\beta_{2,5}$  emission band consists of two peaks (A and B) separated by  $\sim 7.0$  eV, which have their origin in transitions from the Ti 4p character in molecular orbitals, which are mostly C 2s and C 2p in character. Both peaks can be aligned with some emission in the XPS valence band spectrum. Figure V.13 shows that peak B and the Ti L $\alpha$  and  $K\alpha$  emission bands occur at approximately the same energy

position. This means that in this region the C 2p and Ti 3d and 4p states admixed together are found. The Ti L $\alpha$  spectrum presents some emission on the low-energy side, which is not far from peak A in the Ti K $\beta_{2,5}$  spectrum (mainly C 2s in character). As it is reasonable to expect that the atomic orbitals will interact more strongly with each other in the TiC than in the oxides, giving rather more covalent bonds, we can assume a considerable contribution from the Ti 3d orbital in the  $1e_g$  molecular orbital, this contribution being responsible for the low-energy sub-band in the Ti L $\alpha$  spectrum. The C K $\alpha$  spectrum, on the other hand, shows no peak in the region of Ti K $\beta_{2,5}$  peak A, which indicates that the possible carbon 2s - 2p mixing has not occurred. Calculations of the TiC structure carried out by a number of authors (Conklin et al, 1968; Ern et al, 1965) also included the C 2s level in the density-of-states histogram, and are in good agreement with our experimental results. The width of the K $\beta_{2,5}$  (peak B) line ( $\sim 5.0$  eV) agrees with the computed width (4.5 eV) of the 2p bands (from Ern et al, 1965). Further good agreement exists between the peak A - peak B distances as measured by us, ( $\sim 7.0$  eV) and the respective separation of the 2s and (3d + 2p) filled maxima in the density of states histogram (7.1 eV).

The high intensity of peak A in the Ti K $\beta_{2,5}$  may correspond to an enhanced transition probability because of the strong covalent character in TiC. The low-energy sub-band present in the Ti L $\alpha$  emission spectrum also illustrates this character. In fact, this structure which corresponds to some mixing between the Ti 3d and the C 2s is not seen to exist in titanium oxides (see section V.4.2).

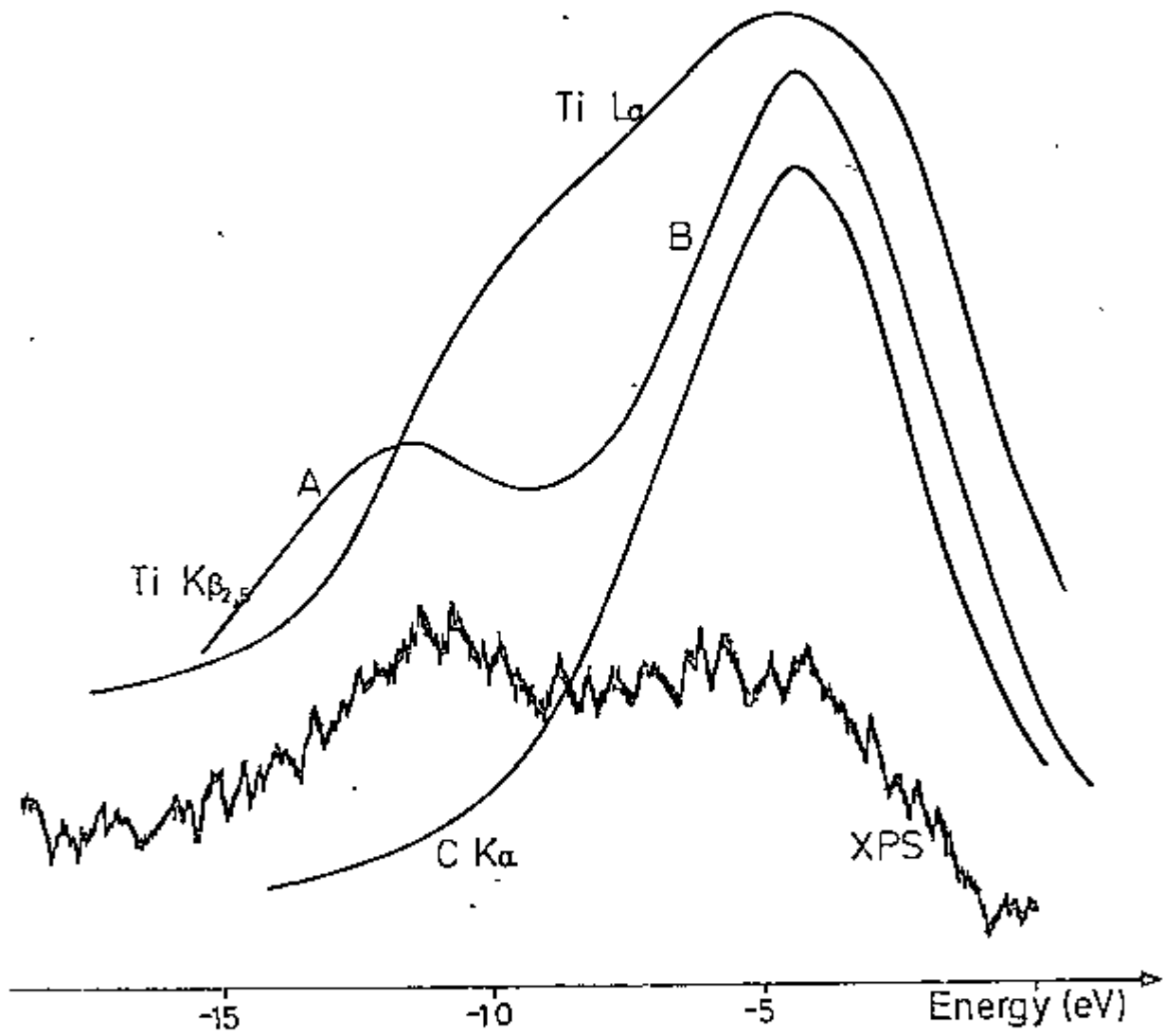


Figure V.13

X-ray emission data for TiC

#### 4.2 Titanium Oxides ( $\text{TiO}_2$ and $\text{Ti}_2\text{O}_3$ )

Transition metal oxides are ideal subjects for an investigation of insulating and metallic states, because of the wide variety of electrical properties observed in apparently similar materials. Metals are characterized by a low resistivity at room temperature and by a linear increase in resistivity as the temperature is raised. Insulators and semiconductors, on the other hand, have extremely high resistivity at room temperature, it decreasing exponentially with increasing temperature. Some materials, however, do not fall into either group. They are semiconductors at low temperatures, but at a certain higher temperature their conductivity suddenly jumps by a large factor (as great as  $10^7$ ) and they are typically metallic. Such a semiconductor-to-metal transition has been observed in  $\text{Ti}_2\text{O}_3$  and  $\text{Ti}_3\text{O}_5$ , for instance, whereas the  $\text{TiO}_2$  behaves always as an insulator. These different electrical properties are believed to be dependent on the degree of occupancy of the metal 3d orbital. Of course, the interaction between the metal 3d and O 2p orbitals is also important.

In order to explain the metal-to-insulator transition phenomenon, various theoretical models have been suggested for  $\text{Ti}_2\text{O}_3$  (Ashkenazi et al, 1973, 1975). In Figure V.14 a schematic diagram of the band structure for  $\text{Ti}_2\text{O}_3$ , as obtained by Ashkenazi et al (1975), is shown. The calculations performed by them included the oxygen 2s and 2p bands, as well as the titanium 3p band.

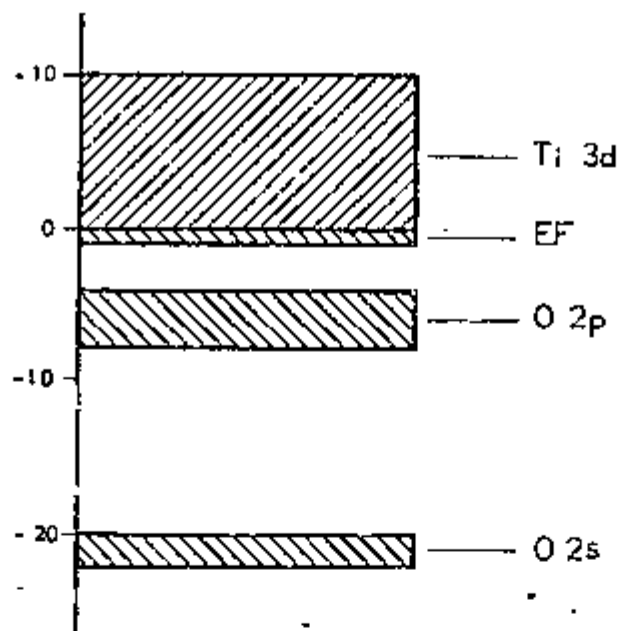


Figure V.14

Schematic diagram of the band structure for  $Ti_2O_3$

The  $Ti_2O_3$  has the corundum structure in which six oxygen atoms form an octahedral group around the metal atom, and each oxygen atom is surrounded by four titanium atoms. We can therefore assume that the schematic diagram of Figure V.10 (for  $Cr_2O_3$ ) is applicable for the local coordination of the Ti in  $Ti_2O_3$ , as well. The X-ray data obtained for  $Ti_2O_3$  are shown in Figure V.15. It is seen that the L $\alpha$  band is considerably broader (as a result of a worse resolution) for the Ti in  $Ti_2O_3$ , than it is for the Cr in all the compounds presented in section V.3. This comes from the fact that the RbAP crystal is not suitable for the analysis of the Ti L $\alpha$  ( $2\theta$  angle larger than  $140^\circ$ ), so that the Pb myristate with larger  $2d$  spacing has to be used instead, which gave a  $2\theta$  angle of only  $40.5^\circ$ .

According to Ashkenazi et al (1975), the width of the O 2p and O 2s bands are 4 eV and 2 eV, respectively. These values are in good agreement with our experimental results for the O K $\alpha$  spectrum and the XPS O 2s band (peak A in

Figure V.15), 4.0 eV and 3.5 eV, respectively, if we consider a line width of 1.5 eV for a single XPS line. It is also seen that the XPS peak B (FWHM = 5.0 eV), which is mainly O 2p in character, spreads over the same energy range as the O K $\alpha$  spectrum. The band structure diagram of Figure V.14 was calculated considering a completely ionic bond between the central metal and the oxygen atoms (that is, neglecting the possibility of any covalent character in the bond formation). In the molecular orbital picture, on the other hand, some mixing between the O 2p and the Ti 3d states has to be considered in the formation of the covalent bonds. To realize this, it suffices to compare the XPS O 2s/VB relative intensity for a typically ionic bond with that for Ti<sub>2</sub>O<sub>3</sub>. We therefore consider, firstly, the t<sub>2g</sub> orbitals of the sulphate ion (see Figure V.5), which is mainly non-bonding in character. Only three out of eight 2p -  $\pi$  orbitals are clearly non-bonding. The area under the XPS peak in the 1t<sub>1</sub> region, therefore, corresponds to only these three orbitals, and it would lead to the experimental ratio O 2s : O 2p :: 17.0 : 1. Nevertheless, if the bond were considered as wholly ionic, then we should have twelve 2p orbitals contributing for the area under the XPS O 2p region, that is, the O 2s/O 2p ratio should be four times smaller, or 4.3 : 1. We now return to Ti<sub>2</sub>O<sub>3</sub> (Figure V.15), where it is found that O 2s : VB :: 1.6 : 1. In conclusion, this ratio is smaller, thus indicating that there must be some contribution from the Ti 3d orbitals.

The main emission of the Ti L $\alpha$  spectrum lines up with a very weak peak in the XPS valence band (peak C in Figure V.15). This emission can be attributed to the

$2t_{2g}$  MO  $\rightarrow$  Ti 2p transition, since  $Ti_2O_3$  has one electron available in the 3d orbital ( $d^1$  configuration).

Rutile ( $TiO_2$ ), whose experimental results are shown in Figure V.16, crystallizes in a tetragonal structure in which the coordination numbers are six for the titanium and three for the oxygen, there being octahedral and triangular arrangement of nearest neighbours of positive and negative ions, respectively (Grant, 1959). This structure is illustrated in Figure V.17. In the experimental results of Figure V.16 it is quite difficult to discern how many sub-band emissions there are in the rutile Ti L $\alpha$  spectrum. If we consider that the Ti L $\alpha$  spectrum presented in section V.4.1 for TiC is formed by two sub-band emissions, we can have an estimate of the FWHM which can be achieved experimentally for this particular diagram line. This value was found to be of the order of 5 eV. Having in mind this value, and comparing it with the width of the rutile Ti L $\alpha$  spectrum of Figure V.16 ( $\sim 12.0$  eV), we observe that this spectrum shows at least two broad intense sub-peaks. We can assume that the long-wave sub-band is lining up with the main bonding orbitals of the system ( $2t_{1u}$ ,  $1t_{2g}$ ,  $2a_{1g}$  and  $2e_g$ ), which possess appreciable metal and oxygen character. Here, as in the case of the chromates, problems arise when we try to explain the origin of the short-wave sub-band. This sub-emission is aligned with the orbitals which are primarily O 2p non-bonding orbitals, with relatively little metal character and little density in the interatomic region ( $1t_{2u}$ ,  $1t_{1g}$  and  $3t_{1u}$ ). The electronic structure of rutile was calculated by Tossell et al (1974).



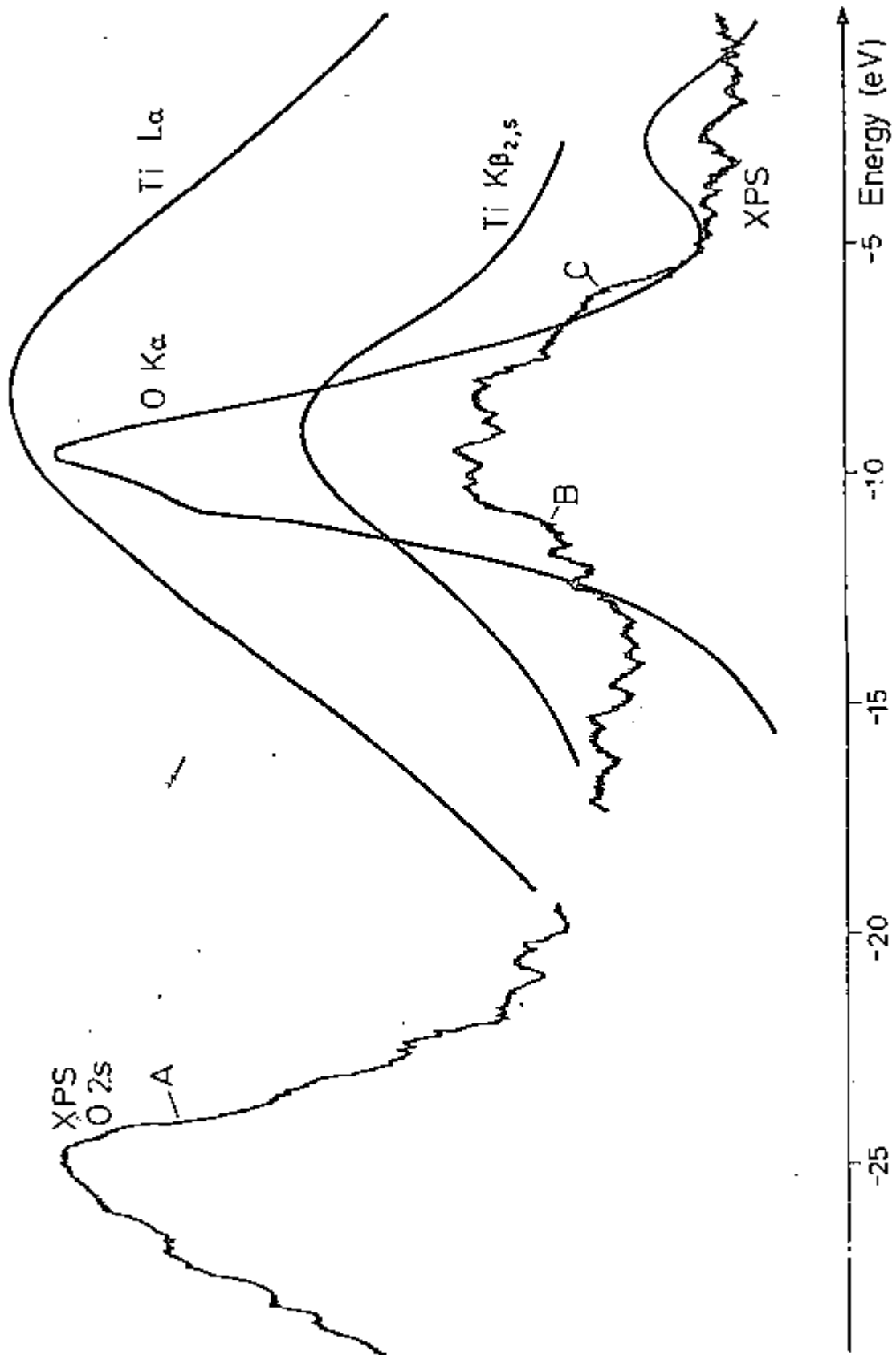


Figure V.15

X-ray emission spectra for  $Ti_2O_3$

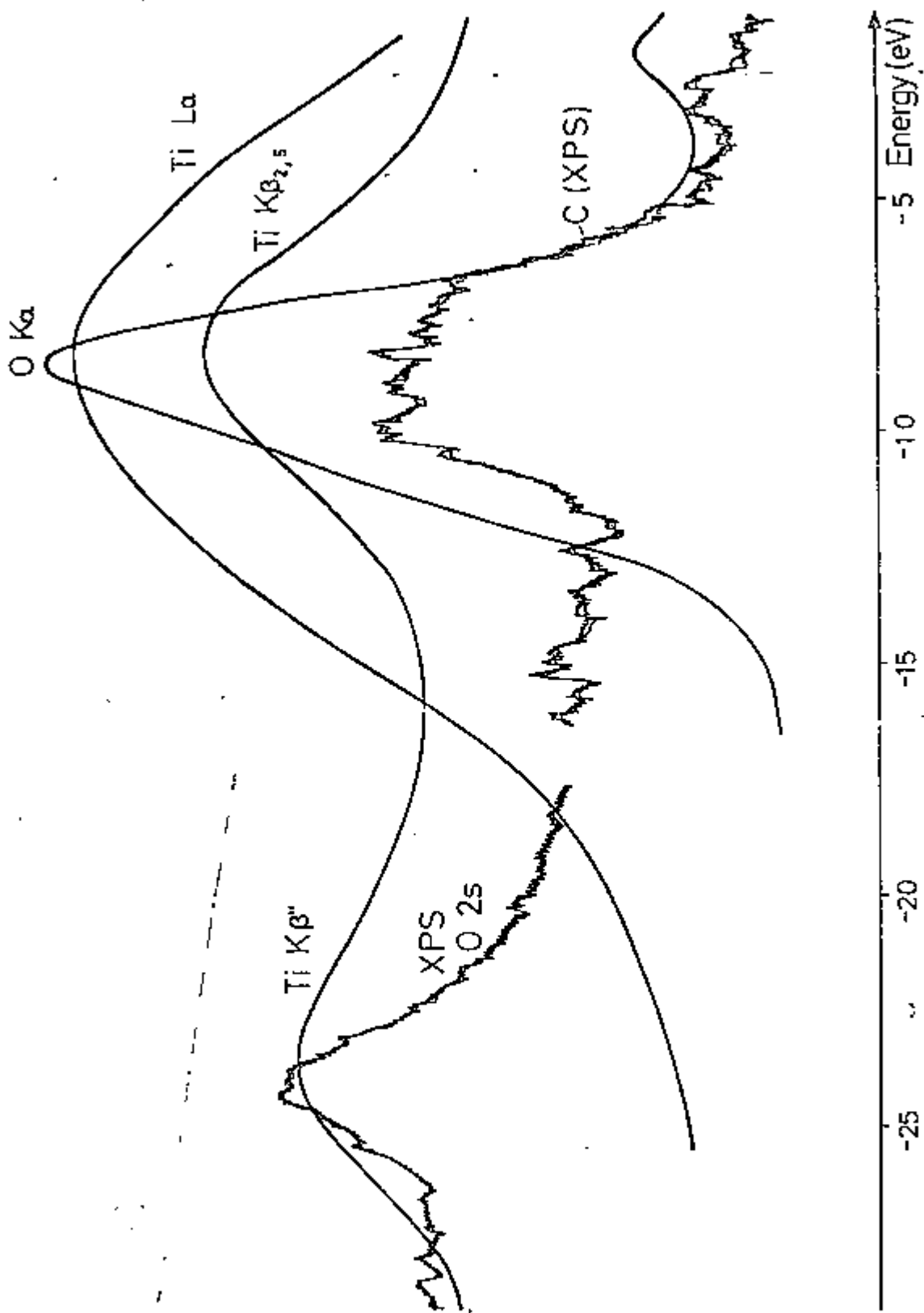


Figure V.16  
X-ray emission data for  $TiO_2$

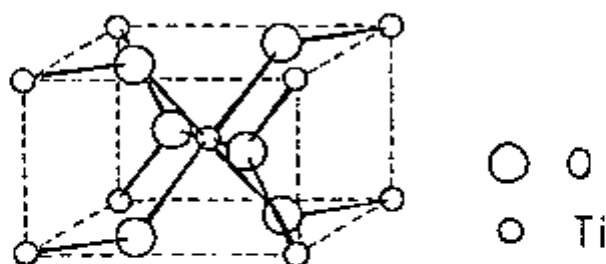


Figure V.17

The rutile structure

The higher-energy LA emission sub-band was assigned by them to a  $1t_{1g} \rightarrow Ti\ 2p$  transition, whereas Fischer (1972) assigned this peak to the  $1t_{2g}$  orbital, discounting the possibility of  $1t_{1g}$  participation, because neither the Ti 3d nor the Ti 4s orbitals belong to this representation. Of course, the approach followed by Tossell et al (1974), based on the crossover transition theory is not the only possible interpretation for the origin of such a short-wave sub-band. We are not going to discuss here all the possible approaches, since this was already done in section V.3.1 for the chromate ion.

As the 3d electronic population decreases as one goes from  $Cr^{3+}$  (3 electrons) to  $Ti^{3+}$  (1 electron) to  $Ti^{4+}$  (0 electrons), we should expect a decrease in the intensity of the peaks, which are mainly metal 3d in character (such as the metal LA and the XPS valence band spectra). Comparing the set of spectra obtained from  $Ti_2O_3$  (Figure V.15),  $TiO_2$  (Figure V.16) and  $Cr_2O_3$  (Figure V.11), we observe that the

main differences lie on the intensity of part of the XPS valence band (peak C in all the figures), which decreases with the number of 3d electrons-available. Changes are also observed in the relative position of the O K $\alpha$  and metal L $\alpha$  spectra. In the TiO<sub>2</sub> the O K $\alpha$  spectrum lines up with the Ti L $\alpha$  emission band, whereas in the Ti<sub>2</sub>O<sub>3</sub> and Cr<sub>2</sub>O<sub>3</sub> the main L $\alpha$  sub-band emission is shifted of a few eV to the right, with respect to the O K $\alpha$  spectrum. A great deal of information about the electric properties of these oxides should arise from the analysis of the Ti L $\alpha$  emission bands, since the overall shape of such emission spectra should be significantly affected by changes of the valence state of the titanium metal. Fischer (1972), studying these spectra from different titanium oxides, verified that the metal ion exerts its main influence on emission component assigned to the orbital 2t<sub>2g</sub> (which presents the higher percentage of 3d character). He argued that this component is indeed the predominant part of the TiO L $\alpha$  spectrum; it becomes considerably smaller in Ti<sub>2</sub>O<sub>3</sub> and it finally disappears in TiO<sub>2</sub>. These changes were interpreted as being due to the decrease in the number of 3d-like electrons of the metal ion, as the oxidation state increases. The lower-energy region of the Ti L $\alpha$  spectrum, on the other hand, reflects Ti 3d character in the 1t<sub>2g</sub> and 2e<sub>g</sub> orbitals, in which the titanium is forming covalent  $\sigma$  bonds with the ligand atoms (O 2p). The better resolution of Fischer's results showed here an increase in the relative intensity of these components, as one goes from TiO to Ti<sub>2</sub>O<sub>3</sub> to TiO<sub>2</sub>. The same tendency can also be observed in our results for Ti<sub>2</sub>O<sub>3</sub> and TiO<sub>2</sub>, despite the very poor resolution of the Ti L $\alpha$  spectra,

in the relative position of the O K $\alpha$  and Ti L $\alpha$  spectra. In Ti<sub>2</sub>O<sub>3</sub>, the main emission of Ti L $\alpha$  coincides with peak C in the XPS spectrum (mainly 3d in character) and is at a higher energy than the O K $\alpha$  peak, whereas in TiO<sub>2</sub> it is aligned with the O K $\alpha$  spectrum, it being in this case more influenced by the O 2p orbitals.

#### V.4.3 Metatitanates and Orthotitanates

For those metatitanates in which the bivalent cation is much larger than the Ti<sup>4+</sup> ion, the perovskite structure is adopted. Calcium, strontium and barium metatitanates are of this type. The mineral BaTiO<sub>3</sub> has a structure in which the oxide ions and the large cation (Ba<sup>2+</sup>) form a cubic close-packed array with the smaller cation (Ti<sup>4+</sup>) occupying the octahedral holes formed exclusively by oxide ions, as shown in Figure V.18. This structure, with the Ba atom surrounded by twelve oxygens, and the Ti atom by six oxygens, is often slightly distorted.

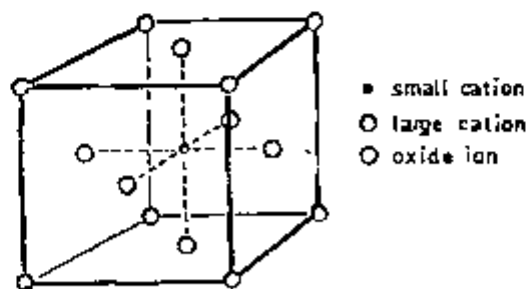


Figure V.18

The perovskite structure

The X-ray emission data related to the barium metatitanate are depicted in Figure V.19. It is expected that the  $\text{BaTiO}_3$  band structure should be similar to that of  $\text{TiO}_2$ , since the short-range order is virtually the same in both materials, although the long-range order is quite different. If the experimental results obtained for  $\text{TiO}_2$  and  $\text{BaTiO}_3$  (Figures V.16 and V.19, respectively) are compared, we realize that they are indeed very similar, except for the O K $\alpha$  spectrum, which shows a little more structure on the low-energy side for the metatitanate ion. The differences observed in the O K $\alpha$  spectrum can be explained by the fact that in  $\text{BaTiO}_3$  the Ti-O bonds are being affected by the Ba-O bonds, which are mainly ionic in character, so that the Ti-O bonds in  $\text{BaTiO}_3$  are more covalent than in  $\text{TiO}_2$ . Furthermore, in Figure V.19, the Ti L $\alpha$  and the Ti K $\beta_{2,5}$  overlap with the shoulder of the O K $\alpha$  spectrum, mostly Ti - O bonding in character, in a slightly different way than for the  $\text{TiO}_2$ .

The only orthotitanate whose experimental results were pursued was  $\text{Sr}_2\text{TiO}_4$  (see Figure V.20). This compound has the  $\text{K}_2\text{NiF}_4$  type of structure (Ruddlesden et al, 1957), which is closely related to the perovskite structure. In the  $\text{K}_2\text{NiF}_4$  structure, the one-unit cells are displaced with respect to one another, so that the Ti atoms have the same environment as in the perovskite, namely six oxygens arranged octahedrally, but the Sr atoms have an unusual arrangement of nine oxygens instead of the original twelve neighbours. The major difference between the set of spectra obtained from  $\text{Sr}_2\text{TiO}_4$  and  $\text{BaTiO}_3$  lies in the presence of a peak A in the  $\text{Sr}_2\text{TiO}_4$  XPS spectrum. This peak arises from the Sr 3f level.

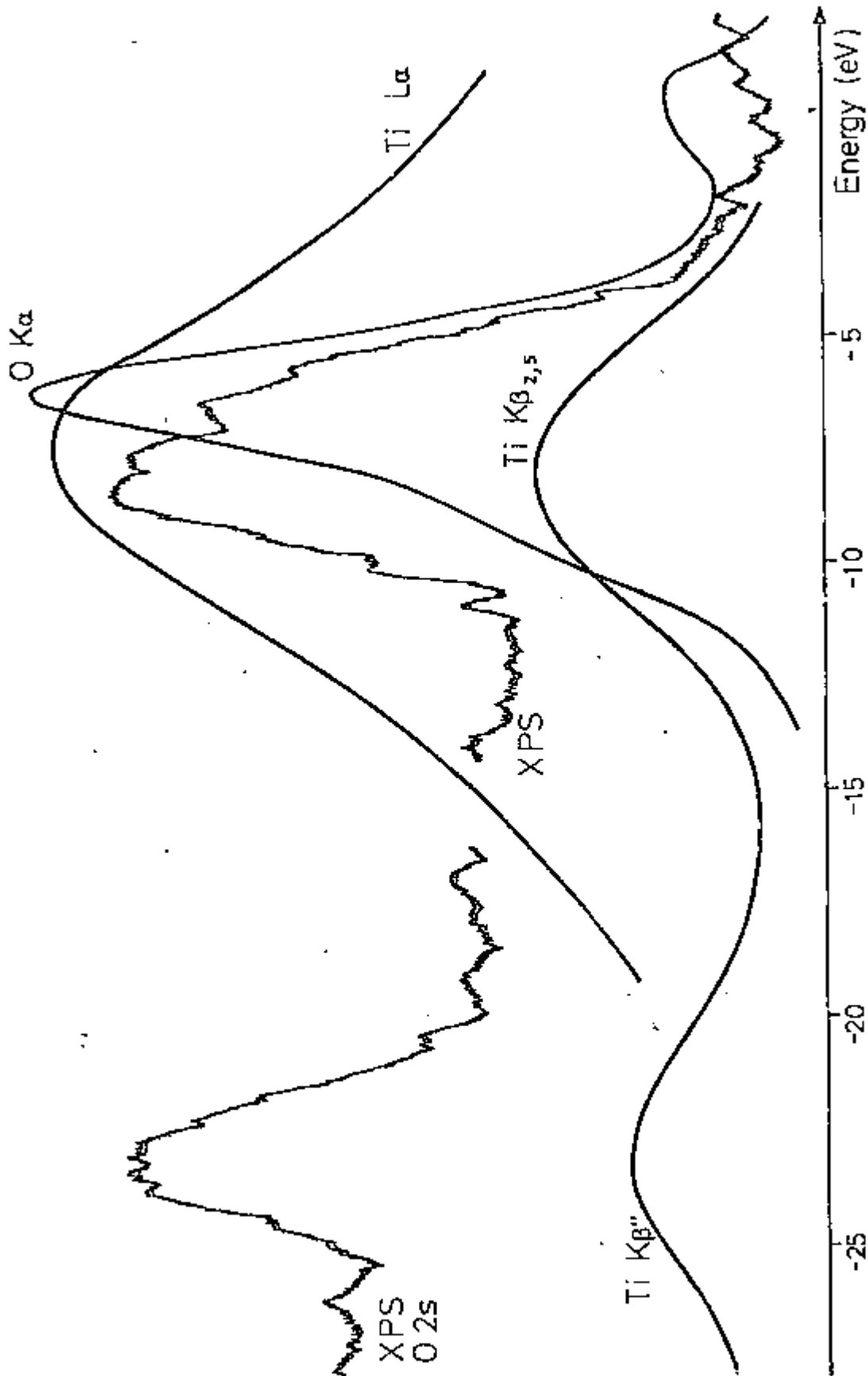


Figure V.19

X-ray emission data for the metatitanate ion ( $\text{BaTiO}_3$ )

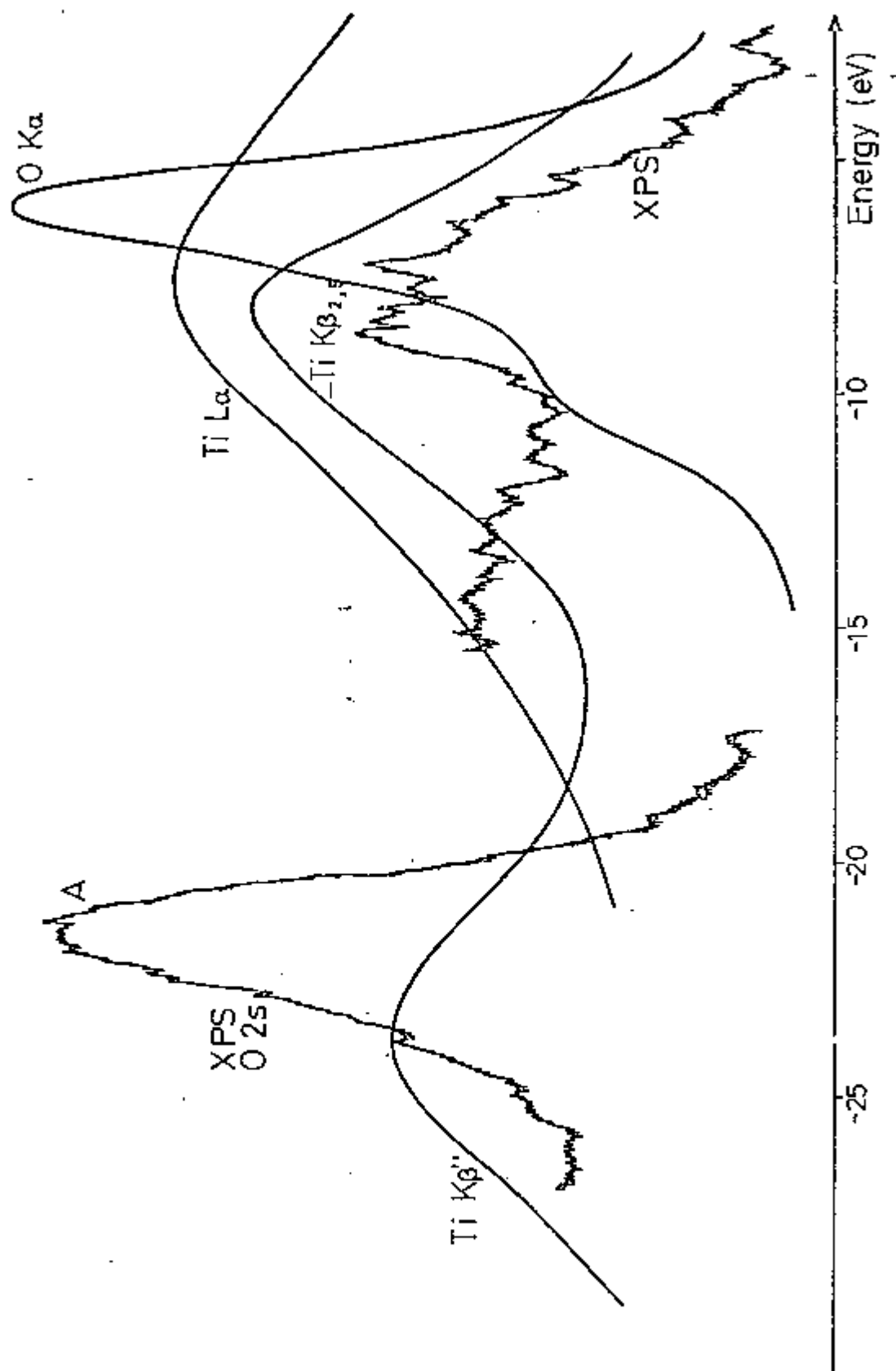


Figure V.20

X-ray emission data for the orthotitanate ion ( $\text{Sr}_2\text{TiO}_4$ )



All the other features of the  $\text{Sr}_2\text{TiO}_4$  spectra are very close to that obtained from  $\text{BaTiO}_3$ , showing that the local coordination of titanium is of paramount importance and that structural changes beyond the basic  $\text{TiO}_6$  coordination unit are of little importance.

#### V.4.4 Titanium Fluoride

In the titanium trifluoride the metal atoms occupy octahedral holes in a close packed arrangement of fluorine atoms. The metal atom has six equidistant F atoms, the Ti-F distance being  $1.97 \text{ \AA}$  (Siegel, 1956). These  $\text{MF}_6$  species are linked by bridging fluorine atoms, such that each fluorine atom is bound to two metal atoms, the interbond angle being  $\sim 150^\circ$ . In Figure V.21 the set of spectra obtained for  $\text{TiF}_3$  is depicted. The intense main peak present in the F K $\alpha$  is attributed to the F (2p)  $\rightarrow$  F (1s) transition. This transition takes place in a singly-ionized species. The high-energy satellite (K $\alpha_{3,4}$ ) observed at about 3 - 4 eV from the main F K $\alpha$  peak is thought to arise from transitions involving doubly-ionized initial levels. The doubly-ionized species could be obtained if a core F 1s electron and a 2p electron were to be ejected at the same time. The transitions between the perturbed energy levels in the doubly-ionized species would result in higher-energy emission lines. Since the fluorine is the most electronegative element, it should form bonds which are mainly ionic in character. In the absence of any interaction between the F 2p and the metal valence orbitals, we should expect the 2p orbitals to be degenerate.

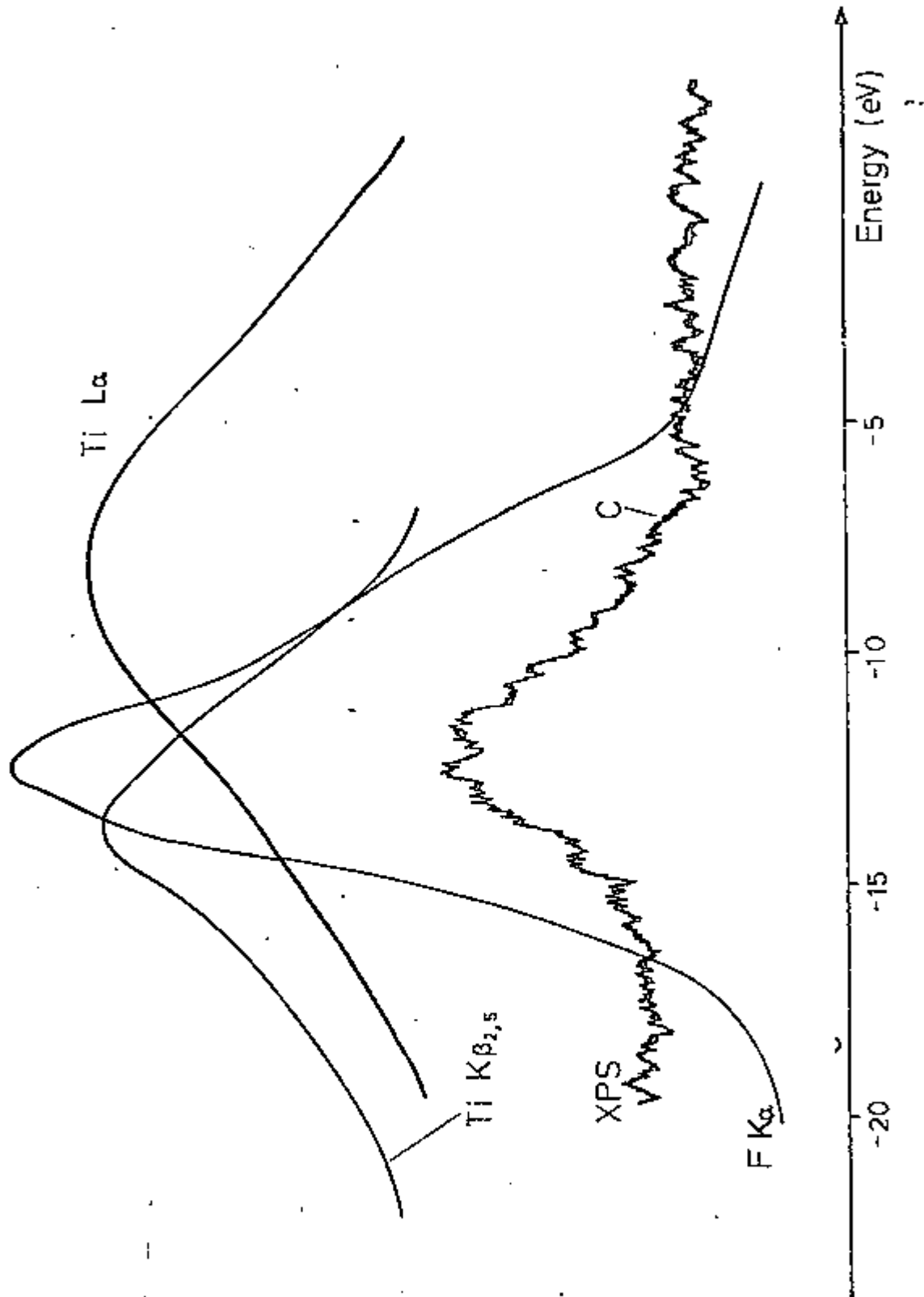


Figure V.21

X-ray emission data for  $\text{TiF}_3$

In this case, the transition  $2p \rightarrow 1s$  should give rise to only one emission diagram line (neglecting the spin-orbit coupling). In practice, however, a small degree of overlap between the metal and the fluorine valence orbitals is possible, and the F K $\alpha$  is expected to show some more structure than just one single emission line. In the TiF<sub>3</sub> each fluorine atom is linked to two Ti atoms and we have one of the F 2p orbitals directed along the Ti - F - Ti axis. These orbitals will therefore interact with all the metal orbitals belonging to the same irreducible representation. Some interaction will also occur between the F 2p "lone-pair" orbitals lying perpendicular to the Ti - F - Ti axis. These small perturbing effects will cause a certain broadening of the F K $\alpha$  peak. The main perturbing influence will of course be that due to the interaction between a F atom and its nearest metal atoms. As a consequence of this overlapping, we should expect to see some more structure on the low-energy side of the main F K $\alpha$  spectrum, which is indeed observed in the spectrum experimentally obtained (see Figure V.21). The experimental F K $\alpha$  spectrum does not show here separate emission lines because the resolution of the spectrometer for X-rays of about 700 eV is of the order of 3 eV. Furthermore, in the alignment of all the spectra available, we found that the Ti L $\alpha$  band presents some low-energy emission which lines up with the low-energy shoulder in the F K $\alpha$  spectrum, as would be expected if the Ti 3d orbitals were making bonds with the fluorine. The Ti K $\beta_{2,5}$  also does line up in the same region, showing the participation of Ti 4p orbitals. This means that in this

region the F 2p, Ti 3d and Ti 4p states are found admixed together. The XPS valence band spectrum shows a broad peak, which also lines up with the F K $\alpha$  and Ti K $\beta_{2,5}$ . On the low-binding-energy side of the XPS spectrum an unresolved peak (C in Figure V.21) can be seen. In this region the Ti 3d orbitals which are non-bonding in character are found. This fact is confirmed by the increase in the relative intensity of the Ti L $\alpha$  spectrum in the same region.

#### V.4.5 Vanadium Oxyanions

X-ray emission spectra were also obtained for some vanadium oxyanions. In Figures V.22, V.23 and V.24 the set of spectra related to V<sub>2</sub>O<sub>5</sub>, NH<sub>4</sub>VO<sub>3</sub> and acetylacetonato vanadium (III) complex are depicted. In V<sub>2</sub>O<sub>5</sub> and NH<sub>4</sub>VO<sub>3</sub> compounds, the metal atom has the highest possible oxidation number. It is clearly seen in Figures V.22 and V.23 that the L $\alpha$  emission bands of both compounds present some structure on the high-energy side. This structure appears as a distinct peak A for the NH<sub>4</sub>VO<sub>3</sub> and as a high-energy sub-band in the V<sub>2</sub>O<sub>5</sub> compound. Both emissions do not present any relevant corresponding feature either in the XPS valence band or in the O K $\alpha$  emission spectra. In the NH<sub>4</sub>VO<sub>3</sub> the central atom is surrounded by a tetrahedral arrangement of oxygen atoms. Since the NH<sub>4</sub>VO<sub>3</sub> has the same problem as for the chromate ion, we shall assume here the same interpretation given in section V.3.1.1. The V<sub>2</sub>O<sub>5</sub> compound (in which the oxygen atoms form a very distorted octahedron around the central atom) was studied by Fischer (1969) and Kurmaev et al (1979).

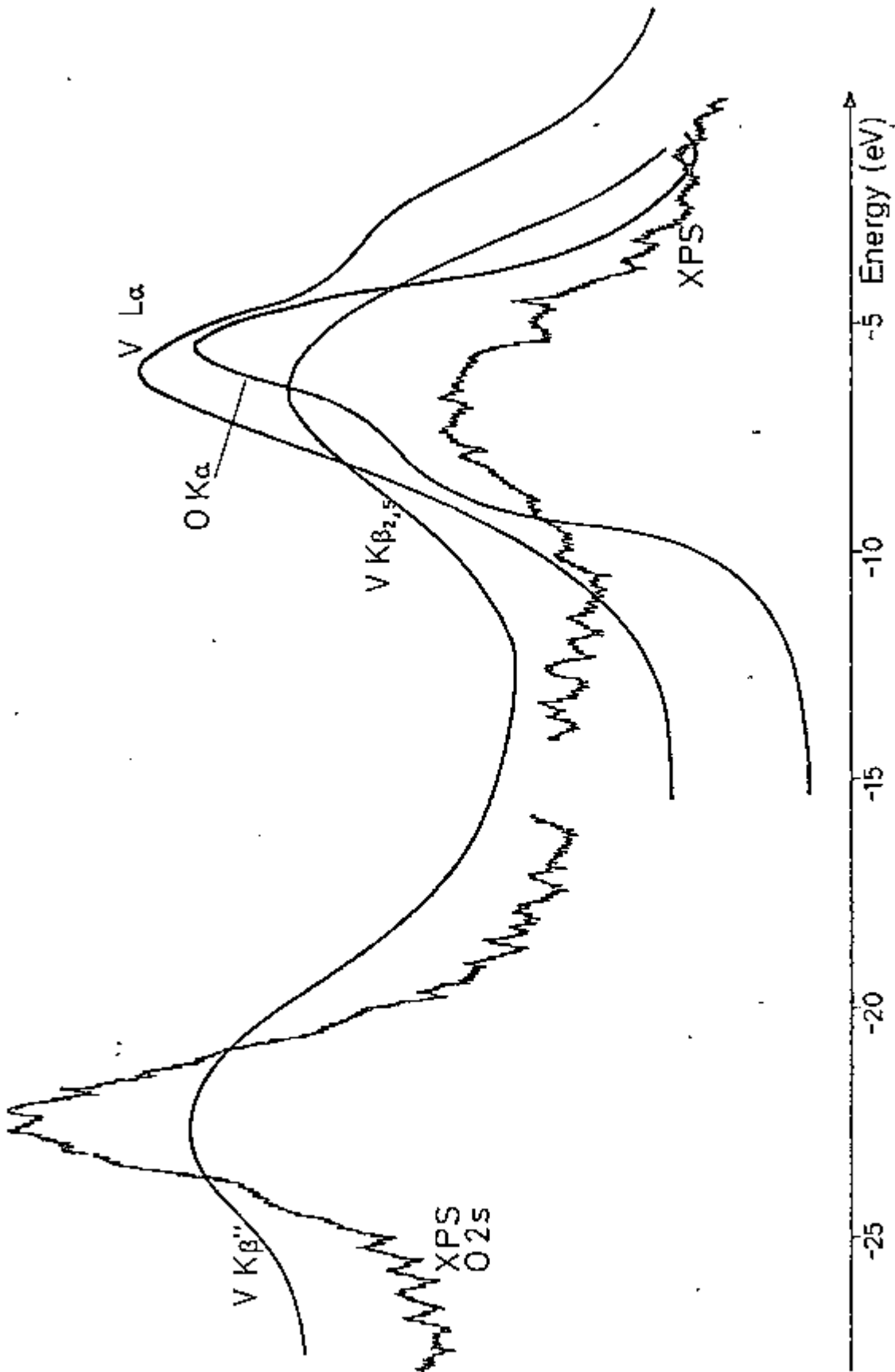


Figure V.22

X-ray emission data for  $V_2O_5$

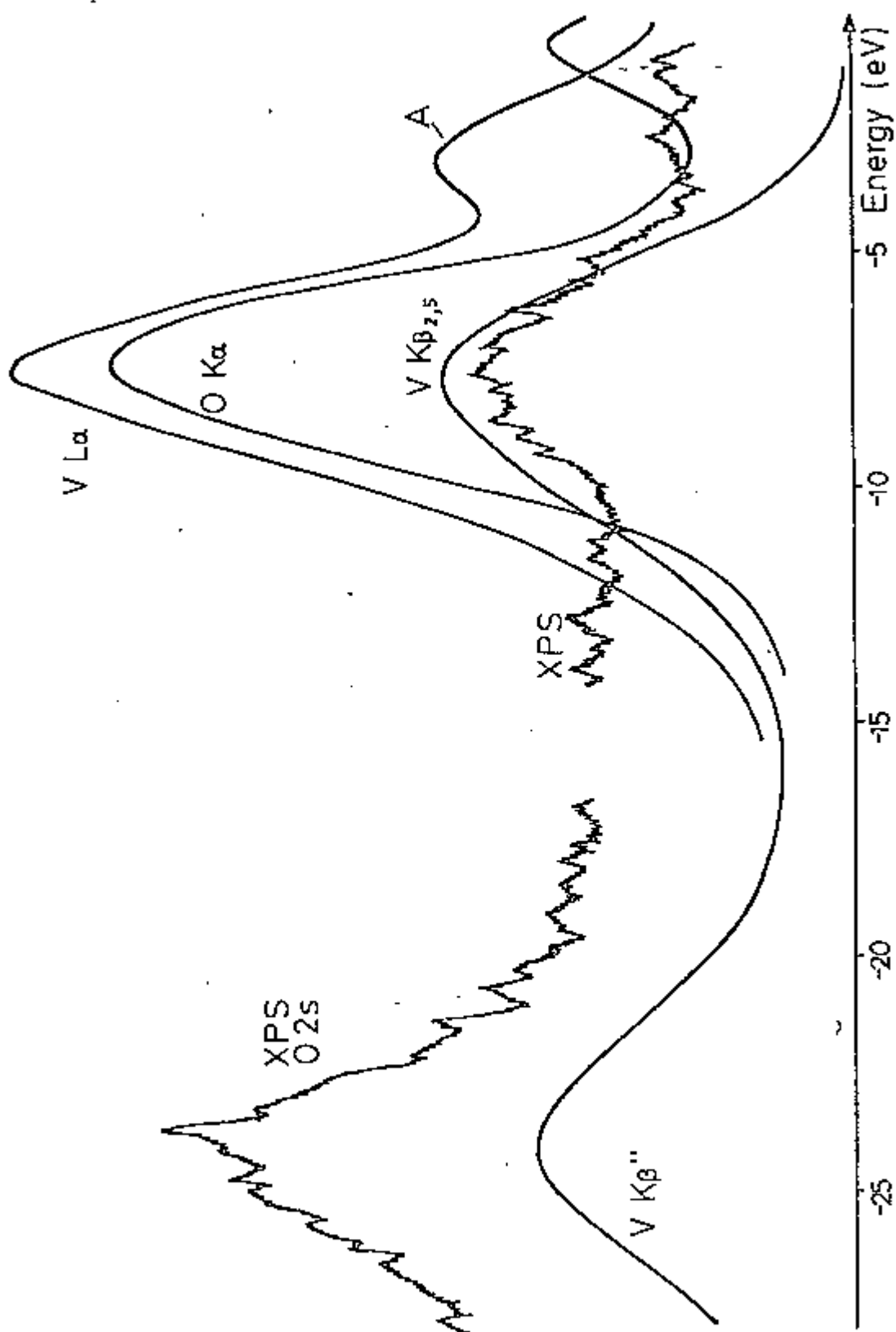


Figure V.23

X-ray emission data for  $\text{NH}_4\text{VO}_3$

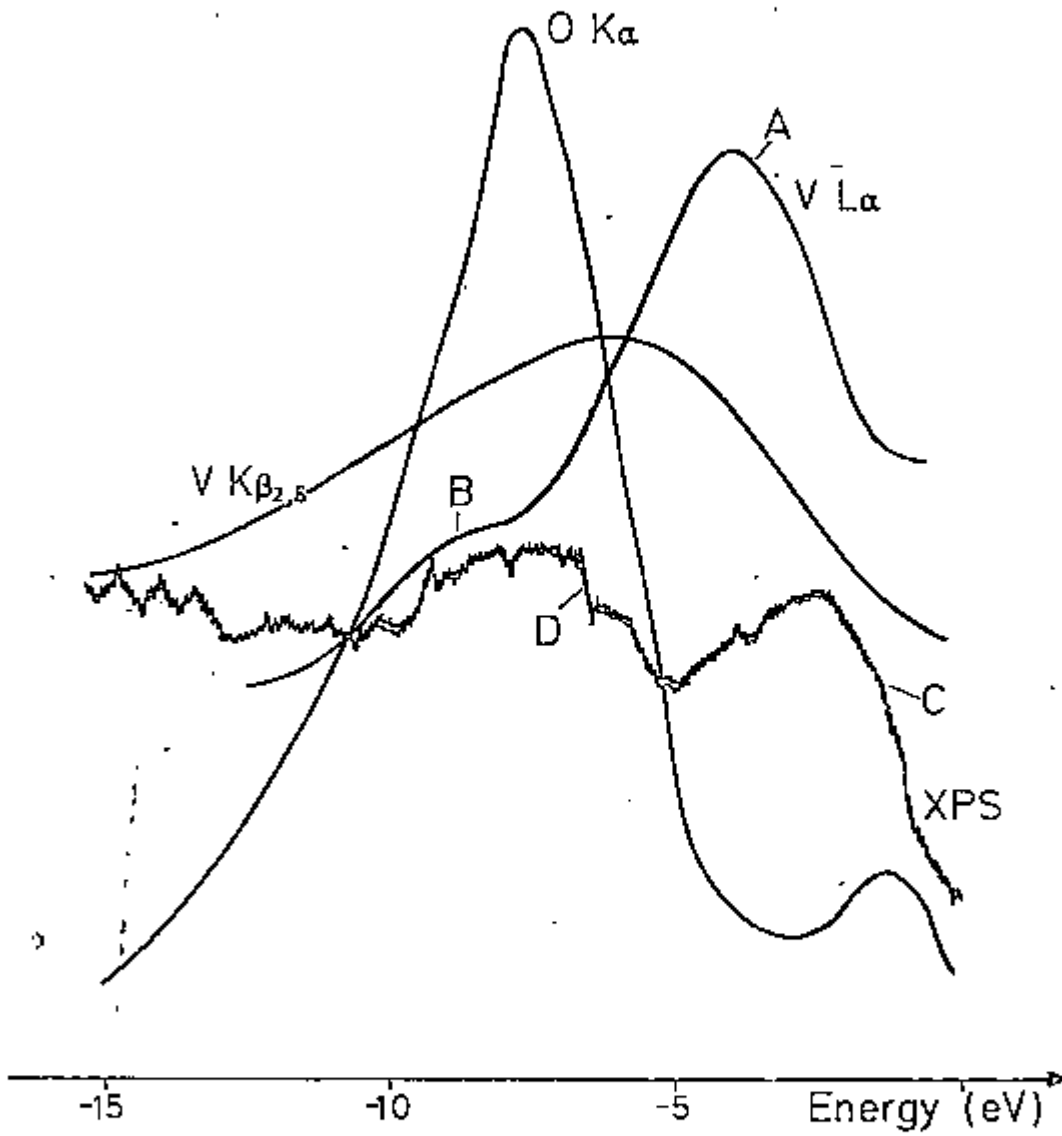


Figure V.24

X-ray emission data for acetylacetonatovanadium (III)

Fischer (1969) assigned the main peak and the short-wave sub-band of the V L spectrum to transitions from the same molecular orbital, but to different core levels - V  $2p_{3/2}$  and V  $2p_{1/2}$ , respectively. In other words, he assigned the main emission to the L $\alpha$  transition and the short-wave sub-band to the L $\beta$  transition. It should be pointed out, however, that the energy separation between the two sub-bands in the V L $\alpha$  spectrum ( $\sim 4.5$  eV) is much smaller than the energy difference between the V  $2p_{1/2}$  and V  $2p_{3/2}$  levels obtained by ESCA measurements ( $\sim 7.5$  eV). We therefore conclude that the L $\beta$  transition cannot be taken into account to explain the origin of the short-wave sub-band. Kurmaev et al (1979), on the other hand, attributed the origin of this sub-emission to the transition between the vacant  $2t_{2g}$  molecular orbital and the V  $2p_{3/2}$  level. This second assignment, showing a participation of excited states in the generation of X-ray L emission spectra, seems to us more reasonable than Fischer's. In fact, it accounts for the presence of L $\alpha$  short-wave sub-band, even when we do not have any corresponding emission in the XPS valence band or O K $\alpha$  spectrum. Clearly, this is not the only possible interpretation for the origin of this short-wave emission. Other possible explanations were already discussed in section V.3.1.1 in connection with the chromate ion.

In the acetylacetonate vanadium (III) compound, the central atom is surrounded by an octahedral arrangement of ligand atoms. The main V L $\alpha$  emission (peak A in Figure 5.24) lines up with the XPS valence band peak C, presumably corresponding to the  $2t_{2g}$  orbital, which is mainly V  $3d^2$  in



character. The O K $\alpha$  spectrum and the V K $\beta_{2,5}$  are aligned with the XPS valence band peak D and the low-energy sub-band of the V L $\alpha$  spectrum. In this region the main bonding orbitals, which have some O 2p, V 4p and 3d character admixed together, are found. The acetylacetonate coordinates to the central atom as the enolate ion through its two oxygen atoms to form a six-membered ring. Some delocalization of the  $\pi$  electrons may occur within this ring, extending over at least the five atoms of the ligand. The metal will also participate in the  $\pi$ -system of the chelate ring by using its d-orbitals of appropriate symmetry (that is, the  $t_{2g}$  symmetry, namely  $3d_{xy,yz,xz}$ ). This involvement is believed to make a significant contribution to the stability of the chelate ring. The oxygen non-bonding molecular orbitals from the three ligands will therefore interact in two different ways. The XPS valence band peak D experimentally obtained (Figure V.24) shows some structure at about -5.5 eV, which may correspond to these two different interactions.

#### V.4.6 Vanadium Fluoride

The vanadium trifluoride is an halogen-bridged polymer involving six-coordinated metal atoms. The structure is the same already described for the titanium fluoride, the M - F distance being, in this case, 1.95 Å (Jack et al, 1951). The results obtained for the VF $_3$  are depicted in Figure V.25. As both titanium and vanadium are octahedrally coordinated to the same ligand atom, we should expect very similar X-ray emission spectra, except for the L $\alpha$  line, which reflects primarily the metal 3d character (Figures V.21 and V.25).

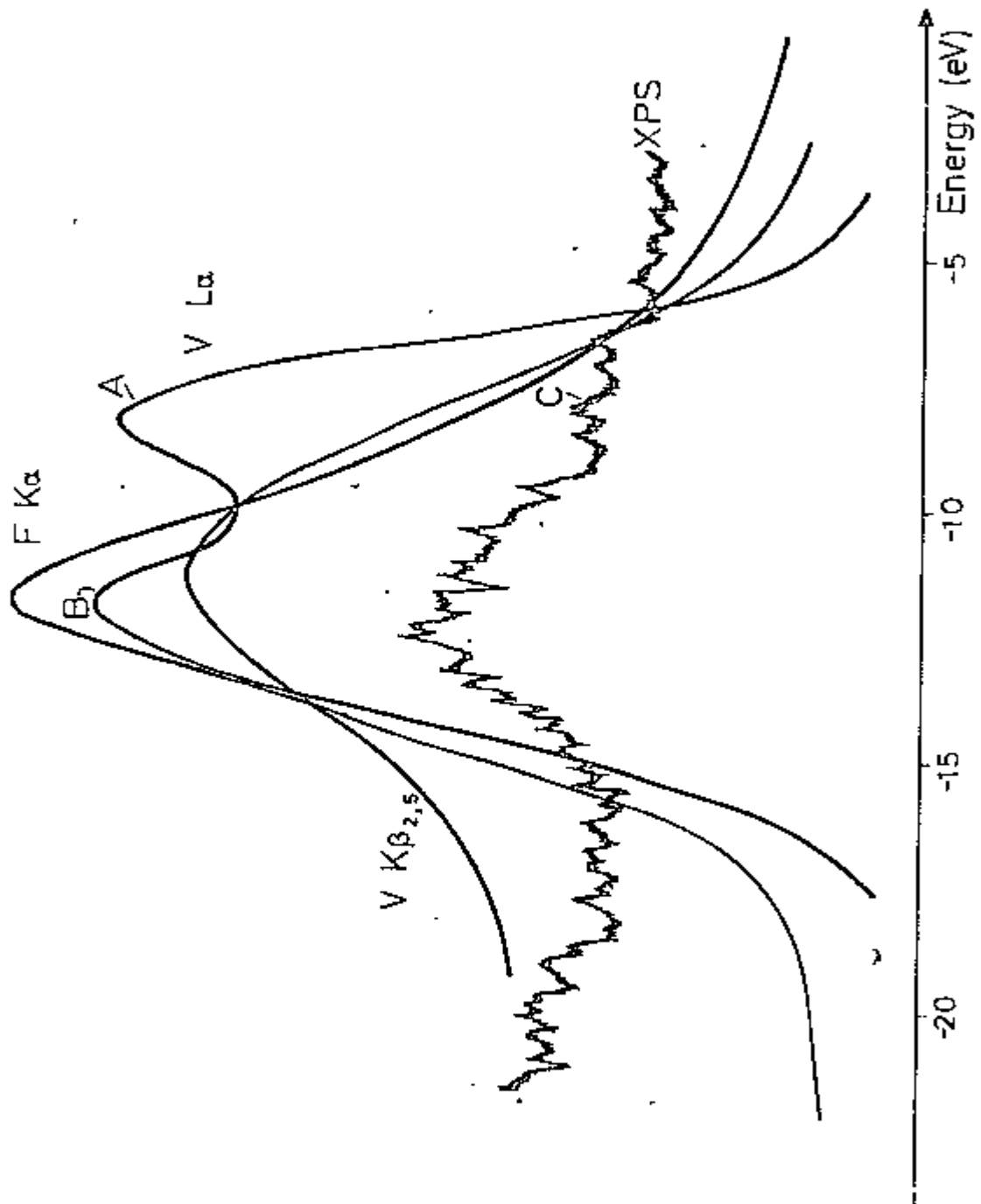


Figure V.25

X-ray emission data for  $VP_3$

Peak C of the XPS valence band spectra should also reflect the metal 3d character, as it is aligned to the main L $\alpha$  peak. Unfortunately, it is difficult to do a meaningful comparison between the relative intensities of such peaks for the simple reason they are not well resolved. Even so, it seems odd that the XPS valence band VF<sub>3</sub> (whose configuration is d<sup>2</sup>) gives only a very weak peak when the corresponding XPS valence band Cr<sub>2</sub>O<sub>3</sub> (d<sup>3</sup> configuration) gives a very intense 2t<sub>2g</sub> peak (see Figure V.11). It seems very likely that the VF<sub>3</sub> had suffered a considerable oxidation, which is indeed confirmed by the very intense oxygen peak obtained for the same compound.

In VF<sub>3</sub> the L $\alpha$  X-ray line comprises two peaks (A and B), whose intensities are roughly the same. Here, again, the high relative intensity of peak B (compared with the same peak obtained experimentally from another vanadium (III) compound - see Figure V.24) seems to indicate a reduction in the number of 3d electrons available.

#### V.5 Influence of the Auger Transition in the Soft X-ray Spectra. Suggestions for Further Work

The L $\alpha$  and L $\beta$  lines arise from the relaxation of initial states with a hole in either the L<sub>11</sub> or L<sub>111</sub> subshells. However, the inner-shell ionized atom may rearrange without radiation by the emission of an electron (Auger effect), which can sometimes affect the X-ray spectrum. All Auger decay processes of the general type KL<sub>p</sub>X<sub>q</sub>, where p and q are subshell indices and X is one

electronic shell, will result in doubly ionized species, at least one hole being in the L shell. In particular, when  $L = X$ , a Coster-Kronig (1935) type electronic transition, between levels of the same principal quantum number, takes place. Coster-Kronig transitions play an important rôle in the L-line X-ray emission spectrum.

Apart from the possibility of self-absorption, the  $L\alpha/L\beta$  ratio will be determined by the relative population of  $L_{II}$  and  $L_{III}$  holes. An interesting situation arises in the transition metal series of elements, where the energy differences between the  $L_{II}$  and  $L_{III}$  hole states is nearly equal to the 3d ionization energy. This means that the  $L_{II}L_{III}M_{IV,V}$  Auger process might occur with the rapid loss of  $L_{II}$  holes and consequent reduction in  $L\beta$  intensity. If  $E_2 > E_1$  (see Figure V.26), the  $2p_{3/2} \rightarrow 2p_{1/2}$  Auger transition will prevail.

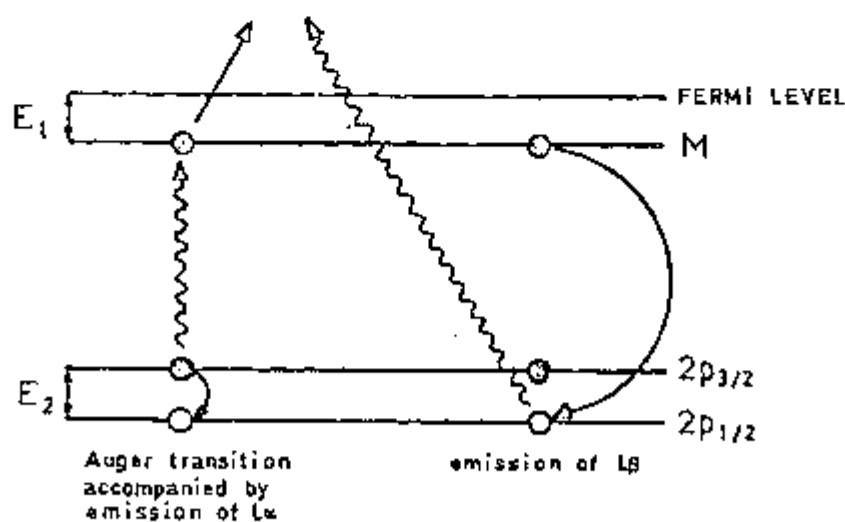


Figure V.26

$L_{II}L_{III}M_{IV,V}$  transition

The final result, in this case, will be a large number of holes in the  $2p_{3/2}$  subshell of a doubly-ionized atom and, therefore, a lot of emission in the L $\alpha$  region, with hardly any L $\beta$  emission. The final configuration  $L_{III}^{-1}M_{IV,V}^{-1}$  will also imply in a decrease of the number of 3d electrons available and, consequently, changes in the valence state spectrum. On the contrary, if  $E_2 < E_1$ , there will not be any Auger emission, the hole will stay in the subshell  $2p_{1/2}$  and we shall see a lot of L $\beta_1$ . The L $\alpha$  - L $\beta$  energy separation ( $E_2$ ) for chromium in the metallic sample is approximately 10 eV. We can therefore assume that  $E_2 > E_1$  for the metal, since it is very unlikely that  $E_1$  (energy separation between the conduction band and the Fermi level) is of the same order of magnitude as  $E_2$ . We can also assume that the number of  $2p_{1/2}$  holes available will be less than statistically expected. We conclude that if the Auger effect is to be relevant in the chromium compounds studied, we should expect an increase in the L $\alpha$ /L $\beta$  ratio for the chromium metal. In addition, for the chromates, this ratio should be approximately equal to 2 : 1, which is the statistically expected ratio.

It is difficult, however, to get any meaningful conclusion about the relative population of the L $_{II}$  and L $_{III}$  holes from the Cr L $\alpha$ /L $\beta$  experimental ratio. In fact, the intensity of both L $\alpha$  and L $\beta$  will be seriously affected by the L $_{III}$  absorption edge (due to a  $2p \rightarrow 3d$  promotion), since its energy is very close to the L $\alpha$  emission, and has a lower energy than the L $\beta$  emission. The absorption edge effect should therefore be greater for the Cr (VI) compounds, whose electronic configuration is  $d^0$ , with

consequent weakening of  $L\beta$  and increase of the  $L\alpha/L\beta$  ratio over 2.

In Table V.6, the Cr  $L\alpha/L\beta$  experimental ratio for different compounds are depicted. It is seen that the intensity of the  $L\beta$  line is relatively stronger in the metal than in the compounds of the same element. We can therefore conclude that the absorption edge effect is the predominant one for the chromium compounds studied.

COMPOUND	$L\alpha/L\beta$ INTENSITY RATIO
Cr metal	3.9
$Cr_2O_3$	4.1
$CrO_3$	7.5
$Na_2CrO_4$	7.5

Table V.6

Chromium  $L\alpha/L\beta$  intensity ratio

The initial state in the production of  $L\alpha$  and  $L\beta$  photons, a hole in the  $L_{II,III}$  subshell, is exactly the same as that for the  $L_I$  ( $3s \rightarrow 2p_{3/2}$ ) and  $L_{II}$  ( $3s \rightarrow 2p_{1/2}$ ) emissions. A detailed study of the  $L_I$  and  $L_{II}$  lines, which result from transitions between electronic levels which are nominally regarded as core levels, would obviously be of much value in the identification of that part of the spectra related to complications in the initial  $2p^+$  state. It is therefore believed that a further study of the  $L_I$ ,  $L_{II}$  lines would complement the work done in this thesis.

— APPENDIX

A FORTRAN PROGRAM FOR ITERATIVE DECONVOLUTION

```

PROGRAM ITER
DIMENSION DATA1(500),H(500),ERROR(500),G(150),
1DATA2(500),FOLD(500),RESID(500)
DIMENSION SMOO(40),SMDAT(500)
CHECK=0.0
READ(5,*)NSMOO,NASM,NBSM,RNORM
READ(5,*)(SMOO(I),I=1,NSMOO)
READ(5,*)BACK
READ(5,*)LIM1,LIM2,NA,NB,ENUF
READ(5,*)(G(J),J=1,LIM2)
DO 10 J=1,LIM1
10 READ(5,*)ISTEP,DATA1(J)
C COMPUTE ERROR BARS FOR ORIGINAL DATA
DO 104 I=1,LIM1
DATA2(I)=DATA1(I)-BACK
IF(DATA2(I).LT.0.0000)DATA2(I)=0.0000
104 CONTINUE
DO 110 I=1,LIM1
110 ERROR(I)=SQRT(DATA1(I)+BACK)
LIK=LIM1-NSMOO+1
DO 407 K=1,LIK
SUM=0.0
MORE=K
DO 408 I=1,NSMOO
SUM=DATA2(MORE)*SMOO(I)+SUM
408 MORE=MORE+1
SMDAT(NBSM+K)=SUM/RNORM
407 CONTINUE
DO 409 I=1,NBSM
409 SMDAT(I)=DATA2(I)
IKJ=LIM1-NA+1
DO 410 I=IKJ,LIM1
410 SMDAT(I)=DATA2(I)
DO 411 I=1,LIM1
IF(SMDAT(I).LT.0.0000)SMDAT(I)=0.0000
411 DATA1(I)=SMDAT(I)
C PRINT ORIGINAL SMOOTHED DATA
WRITE(6,105)
105 FORMAT(1H1,5H DATA)
WRITE(6,106)
106 FORMAT(1H ,23H ORIGINAL SMOOTHED DATA)
WRITE(6,107)(DATA1(J),J=1,LIM1)
107 FORMAT(10F10.1)
C WRITE DATA AFTER REMOVAL OF BACKGROUND
WRITE(6,108)
108 FORMAT(1H ,19H ORIG DATA MINUS BG)
WRITE(6,109)(DATA2(I),I=1,LIM1)
109 FORMAT(10F10.1)
C PRINT ERROR VALUES
WRITE(6,111)
111 FORMAT(1H ,22H ERROR VALUES FOR DATA)
WRITE(6,112)(ERROR(I),I=1,LIM1)
112 FORMAT(10F10.1)
C STORE TREATED DATA IN MATRIX H
DO 113 I=1,LIM1
113 H(I)=DATA1(I)
C WORK OUT RMS FOR ORIGINAL DATA
SUM=0.0
DO 114 I=1,LIM1

```



```

RMS1=DATA1(I)+SUM
114 SUM=RMS1
    RLIM1=LIM1
    RMS=SQRT(RMS1/RLIM1)
C   PRINT RMS FOR ORIGINAL DATA
    WRITE(6,115)
115 FORMAT(1H ,24H R.M.S. OF ORIGINAL DATA)
    WRITE(6,116)RMS
116 FORMAT(F10.1)
    LIK=LIM1-LIM2+1
150 DO 301 K=1,LIK
    SUM=0.0
    NUMB=K
    MORE=K
    DO 302 I=1,LIM2
    SUM=DATA1(MORE)*G(I)+SUM
302 MORE=MORE+1
    FOLD(NB+NUMB)=SUM
301 CONTINUE
    DO 303 I=1,NB
303 FOLD(I)=DATA1(I)
    IKJ=LIM1-NA+1
    DO 304 I=IKJ,LIM1
304 FOLD(I)=DATA1(I)
    WRITE(6,305) (FOLD(I),I=1,LIM1)
305 FORMAT(10F12.2)
C   SUBTRACT FOLD FROM DATA
    DO 122 I=1,LIM1
122 RESID(I)=H(I)-FOLD(I)
C   PRINT RESIDUALS
    WRITE(6,123)
123 FORMAT(1H , 'RESIDUALS')
    WRITE(6,124) (RESID(I),I=1,LIM1)
124 FORMAT(10F12.2)
C   COMPUTE RMS OF UNFOLD
    CONS=0.0
    DO 151 I=1,LIM1
    RMS2=(RESID(I)*RESID(I))+CONS
151 CONS=RMS2
    RMSFN=SQRT(RMS2/RLIM1)
    WRITE(6,152)
152 FORMAT(1H ,31H COMPARISON RMS OF ABOVE UNFOLD)
    WRITE(6,153)RMSFN
153 FORMAT(F10.3)
C   GENERATE NEW FUNCTION
    DO 125 I=1,LIM1
    DATA1(I)=DATA1(I)+RESID(I)
    IF (DATA1(I).LT.0.0000) DATA1(I)=0.0000
125 CONTINUE
C   PRINT NEW FOLD
    WRITE(6,126)
126 FORMAT(1H ,18H UNFOLDED FUNCTION)
    WRITE(6,127) (DATA1(I),I=1,LIM1)
127 FORMAT(10F10.2)
    CHECK=CHECK+1.0
    IF (CHECK.EQ.ENUF) STOP
    GO TO 150
    END

```

BIBLIOGRAPHY

Aarons L.J. & Guest M.F. & Hall M.B. & Hillier I.H. (1973)  
J. Chem. Soc. Faraday Trans. II, 69 , 563

Adler D. & Brooks H. (1967a)  
Phys. Rev., 155 , 826

Adler D. & Feinleib J. & Brooks H. & Paul W. (1967b)  
Phys. Rev., 155 , 851

Allison & Armstrong (1925)  
Phys. Rev., 26 , 701

Asaad W.N. (1959)  
Proc. Roy. Soc., A249 , 555

Ashkenazi J. & Weger M. (1973)  
Adv. Phys., 22 , 207

Ashkenazi J. & Chuchem T. (1975)  
Phil. Mag., 32 , 763

Auger P. (1925)  
J. Phys. Radium, 6 , 205

Auger P. (1926)  
Ann. Phys., 6 , 183

Babushkin F.A. (1964)

Acta Physiol. Polon., 25 , 749

Barkla C.G. (1911)

Phil. Mag., 22 , 396

Beatham N. & Orchard A.F. (1976)

J. Electron Spectrosc. Relat. Phenom., 9 , 129

Beckman O. (1933)

Ark. Fys., 9 , 495

Bergengren J. (1920)

Phys. Zeits., 3 , 247

Best P.E. (1962)

Proc. Phys. Soc. Lond., 79 , 133

Best P.E., (1965)

Bull. Am. Phys. Soc., 10 , 29

Best P.E. (1966)

J. Chem. Phys., 44 , 3248

Best P.E. (1968)

J. Chem. Phys., 49 , 2797

Bohr N. (1913)

Phil. Mag., 6 (1), 476 and 857

Bragg W.L. (1912)

Proc. Camb. Phil. Soc., 17 , 43

Briggs D. & Gibson V.A. (1974)

Chem. Phys. Lett., 25 , 493

Brisk M. & Baker A.D. (1975)

J. Electron Spectrosc. Relat. Phenom., 7 , 81

Burek A.J. (1975)

Los Alamos Scientific Laboratory, UCLA

LA-UR-75-1593

Burger H.C. & van Cittert P.H. (1932a)

Phys. Zeits., 79 , 722

Burger H.C. & van Cittert P.H. (1932b)

Phys. Zeits., 81 , 428

Carlson T.A. (1967)

Phys. Rev., 156 , 142

Carlson T.A. (1975)

Photoelectron and Auger Spectroscopy

Plenum Press

Carver J.C. & Schweitzer G.K. & Carlson T.A. (1972)

J. Chem. Phys., 57 , 973

## Bibliography

Clack D.W. (1972)

J. Chem. Soc., Faraday Transactions II, 10 , 1672

Conklin Jr. J.B. & Silversmith D.J. (1968)

Internat. J. Quantum Chem. (Suppl), 25 , 243

Coster D. & Kronig R. de L. (1935)

Physica, 2 , 13

Cotton F.A. & Wilkinson G. (1966)

Advanced Inorganic Chemistry

Interscience

Coulthard M.A. (1967)

Proc. Phys. Soc., 91 , 44

de Broglie L. (1924)

Thesis, Paris

Phil. Mag., 47 , 446

Demekhin V.F. & Lemeshko G.F. & Shuvaev A.T. (1974) ?

Izv. Akad. Nauk. SSSR, Ser. Fiz., 38 (3), 587

Deodhar G.B. (1931)

Proc. Roy. Soc., A131 , 647

Dirac P.A.M. (1964)

Nature, 203 , 115

## Bibliography

Dodd C.G. & Glen G.L. (1968)

J. Appl. Phys., 39 , 5377

Dolenko G.N. & Sadovskii A.P. & Mazalov L.N.

& Gluskin E.S. & Kochubei V.A. (1974)

Bull. Akad. Sci. SSSR Phys. Series, 38 , 603

Duane & Stenström (1920)

Proc. Nat. Acad. Sci., 6 , 477

Einstein A. (1905)

Ann. Phys., 17 , 132

Ekstig B. & Kallne E. & Noreland E. & Manne R. (1970)

Physica Scripta, 2 , 38

Ellis D.E. & Freeman A.J. & Ros P. (1968)

Phys. Rev., 176 , 688

Ergun S. (1968)

J. Appl. Crystallogr., 1 , 19

Ern V. & Switendick A.C. (1965)

Phys. Rev., A137 , 1927

Ernst R.R. (1966)

Adv. Magn. Reson., 2 , 18

## Bibliography

Eyring H. & Walter J. & Kimball G.E. (1967)

Quantum Chemistry

John Wiley

Fadley C.S. & Shirley D.A. & Freeman A.J. & Bagus P.S.

& Mallow J.V. (1969)

Phys. Rev. Lett., 23 , 1397

Fadley C.S. & Shirley D.A. (1970)

Phys. Rev., A2 , 1109

Fischer D.W. (1969)

J. Appl. Phys., 40 , 4151

Fischer D.W. (1970a)

Adv. X-ray Anal., 13 , 182

Fischer D.W. (1970b)

J. Appl. Phys., 41 , 3561

Fischer D.W. (1971)

J. Chem. Sol., 32 , 2455

Fischer D.W. (1972)

Phys. Rev. Sol. St., 5B , 4219

Fischer D.W. & Baun W.L. (1965)

J. Appl. Phys., 36 , 534

## Bibliography

- Fischer D.W. & Baun W.L. (1968)  
J. Appl. Phys., 39 , 4757
- Freeman A.J. & Ellis D.E. (1970)  
Phys. Rev. Lett., 24 , 516
- Friedman H. (1949)  
Proc. I.R.E., 37 , 791
- Friedrich W. & Knipping P. & Laue M. (1912)  
Ber. Bayer. Akad. Wiss., 303
- Frost D.C. & Ishitani A. & McDowell C.A. (1972)  
Mol. Phys., 24 , 861
- Gohshi Y. & Ohtsuka A. (1973)  
Spectrochim. Acta, 28B , 179
- Grant F.A. (1959)  
Rev. Mod. Phys., 31 , 646
- Haga H. & Wind (1899)  
Wied. Ann., 68 , 884
- Hagström S. & Nordling C. & Siegbahn K. (1964)  
Phys. Zeits., 178 , 439
- Hansen J.S. & Freund H.U. & Fink R.W. (1970)  
Nucl. Phys., A142 , 604



## Bibliography

Haycock D.E. (1978)

PhD Thesis, University of London

Haycock D.E. & Urch D.S. (1978)

X-ray Spectrometry, 7 (4), 206

Hedin L. & Johansson A. (1969)

J. Phys. (Atom. Molec. Phys.), 2B (2), 1336

Herzberg G. (1944)

Atomic Spectra and Atomic Structure

Dover Publications

Hillier I.H. & Saunders V.R. (1971)

Chem. Phys. Lett., 9 , 219

Huheey J.E. (1978)

Inorganic Chemistry - Principles of Structure and Reactiv

Harper and Row Publishers

Idei S. (1929)

Nature, 123 , 643

Jack K.H. & Gutmann V. (1951)

Acta Cryst., 4 , 246

Jenkins R. (1974)

An Introduction to X-ray Spectrometry

Heyden & Son

## Bibliography

- Johansson L.Y. & Larsson R. & Blomquist J. & Cederstrom C  
Grapengiesser S. & Helgeson U. & Moberg L.C. &  
Sundbom M. (1974)  
Chem. Phys. Lett., 24 , 508
- Jones A.F. & Misell D.L. (1967)  
Brit. J. Appl. Phys., 18 , 1479
- Jørgensen C.K. & Berthou H. (1972)  
Chem. Phys. Lett., 13 , 187
- Kauzmann W. (1957)  
Quantum Chemistry  
Academic Press
- Koopmans T. (1933)  
Physica, 1 , 104
- Koster A.S. & Mendel H. (1970)  
J. Phys. Chem. Sol., 31 , 2511
- Krause M.O. & Carlson T.A. & Dismukes R.D. (1968)  
Phys. Rev., 170 , 37
- Krause M.O. & Wuilleumier F. (1972)  
J. Phys., 5B , L143
- Kurmaev E.Z. & Cherkashenko V.M. & Gubanov V.A. (1979)  
J. Electron Spectrosc. Relat. Phenom., 16 , 455

Lasker W. (1955)

J. Phys. Radium, 16 , 644

Laüger K. (1971)

J. Phys. Chem. Sol., 32 , 609

Lazzarini E. & Lazzarini Fantola A.L.

& Mandelli Betoni M. (1978)

Radiochimica Acta, 25 , 81

Lukirskii A.P. & Brytov I.A. (1964)

Sov. Phys. Sol. St., 5 , 33

Lundquist O. (1930)

Phys. Zeits., 60 , 642

Manne R. (1970)

J. Chem. Phys., 52 , 5733

Massey H.S.W. & Burhop E.H.S. (1935)

Proc. Camb. Phil. Soc., 32 , 461

Mazalov L.N. (1977)

Zh. Strukt. Khim., 18 , 607

Meitner L. (1922)

Phys. Zeits., 9 , 131

Meyer H.T. (1929)

Wissenschaftliche Veröffentlichungen

Aus. Dem. Siemens-Konzern, 7 , 108

Moore C.R. (1949)

Tables of Atomic Energy Levels

National Bureau of Standards, circular n. 467

Morin F.J. (1961) -

J. Appl. Phys., 32 , 2195

Moseley H.G.J. (1914)

Phil. Mag., 27 , 703

Moskowitz J.W. & Hollister C. & Hornback C.J.

& Basch H. (1970)

J. Chem. Phys., 53 , 2570

Nefedov V.I. (1966)

J. Struct. Chem., 7 , 672

Nelson G.C. & Saunders B.G. & Salem S.I. (1970)

At. Data, 1 , 377

Newnham R.E. & Dehaan Y.M. (1962)

Z. Kristallogr., 117 , 235

O'Brien C.H.M. & Skinner H.W.B. (1940)

Proc. Roy. Soc., A176 , 229

- Oleari L. & De Michelis G. & Di Sipio L. (1965)  
Mol. Phys., 10 , 111
- Pačić G. & Pečar V. (1976)  
Phys. Rev., A14 , 2190
- Paterson M.S. (1950)  
Proc. Phys. Soc. Lond., A63 , 477
- Payne W.B. & Levinger J.S. (1956)  
Phys. Rev., 101 , 1020
- Pines D. (1956)  
Rev. Mod. Phys., 28 , 184
- Planck M. (1900)  
Verhandl. Deut. Ges. Phys., 2 , 237
- Politzer P. & Daiker K.C. (1973)  
Chem. Phys. Lett., 20 , 309
- Porteus J.O. (1962)  
J. Appl. Phys., 33 , 700
- Prins R. & Novakov T. (1972)  
Chem. Phys. Lett., 16 , 86
- Robinson H. (1923)  
Proc. Roy. Soc., 104 , 455

Roentgen W.C. (1898)

Ann. Phys. Chem., 54 , 1

Rooke G.A. (1963)

Phys. Lett., 3 , 234

Ruddlesden S.N. & Popper P. (1957)

Acta Cryst., 10 , 538

Sadovskii A.P. & Kravtsova E.A. & Mazalov L.N. (1975)

Izv. Sib. Otd. Akad. Nauk. SSSR, Ser. Khim. Nauk., 4 , 62

Salem S.I. & Johnson J.P. (1969)

Phys. Lett., 30A , 163

Salem S.I. & Falconer J.H. & Winchell R.W. (1972)

Phys. Rev., A6 , 2147

Sauder W.C. (1966)

J. Appl. Phys., 37 , 1495

Savitsky A. & Golay M.J.E. (1964)

Anal. Chem., 36 (8), 1627

Scofield J.H. (1969)

Phys. Rev., 179 , 9

Scofield J.H. (1976)

J. Electron Spectrosc. Relat. Phenom., 8 , 129

Seka W. & Hanson H.P. (1969)

J. Chem. Phys., 50 , 344

Sevier K.D. (1972)

Low-energy Electron Spectroscopy

John Wiley

Siegbahn K. & Nordling C. & Fahlman A. & Nordberg R.

& Hamrin K. & Hedman J. & Johansson G. & Bergmark T.

& Karlsson S. & Lindgren I. & Lindberg B. (1967)

Nova Acta Reg. Soc. Sci. Upsaliensis, 20 (IV), 230

Siegbahn M. & Žáček A. (1923)

Ann. Physik, 71 , 187

Siegel S. (1956)

Acta Cryst., 9 , 684

Skinner H.W.B. (1940)

Phil. Trans. Roy. Soc., A239 , 95

Slater J.C. (1960)

Quantum Theory of Atomic Structure

McGraw Hill

Slater R.A. & Urch D.S. (1972)

J. Chem. Soc. Chem. Commun., 9 , 564

- Slater R.A. & Urch D.S. (1973)  
Band Structure Spectroscopy of Metals and Alloys  
Fabian D.J. & Watson L.M. (ed.)  
Academic Press
- Slivinsky V.W. & Ebert P.J. (1969)  
Phys. Lett., 29A , 463
- Slivinsky V.W. & Ebert P.J. (1972)  
Phys. Rev., A5 ,1581
- Soller W. (1924)  
Phys. Rev., 24 , 158
- Sommerfeld A. (1900)  
Phys. Zeits., 2 , 59
- Sommerfeld A. (1912)  
Ann. Phys., 38 , 473
- Spencer R.C. (1939)  
Phys. Rev., 55 , 239
- Spencer R.C. (1949)  
J. Appl. Phys., 20 , 413
- Stokes A.R. (1948)  
Proc. Phys. Soc. Lond., A61 , 382



Tamaki Y. & Omori T. & Shiokawa T. (1975)  
Radiochem. Radioanal. Lett., 20 , 255

Tamaki Y. & Omori T. & Shiokawa T. (1978)  
Japan J. Appl. Phys., 17 (suppl.2), 425

Tamaki Y. & Omori T. & Shiokawa T. (1979)  
Radiochem. Radioanal. Lett., 37 (1,2), 39

Taylor G.R. & Payne W.B. (1960)  
Phys. Rev., 118 , 1549

Tossell J.A. & Vaughan D.J. & Johnson K.H. (1974)  
Amer. Mineral., 59 , 319

Tsutsumi K. (1959)  
J. Phys. Soc. Japan, 14 , 1696

Tsutsumi K. & Nakamori H. (1968)  
J. Phys. Soc. Japan, 25 , 1418

Urch D.S. (1970)  
J. Phys. (Sol. St. Phys.), 3C , 1275

Urch D.S. (1971)  
Quart. Rev., 25 , 343

Urch D.S. (1975)  
Proc. 7th. Int. Hot-atom Conf., Julich

van Cittert P.H. (1931)

Phys. Zeits., 69 , 298

Viste A. & Gray H.B. (1964)

Inorg. Chem., 3 , 1113

Walter B. & Pohl R. (1909)

Ann. Phys., 29 , 331

Wapstra A.H. & Nijgh G.J. & van Lieshout R. (1959)

Nuclear Spectroscopy Table

North-Holland

Wells A.F. (1975)

Structural Inorganic Chemistry

Oxford

Wertheim G.K. (1975)

J. Electron Spectrosc. Relat. Phenom., 6 , 239

Wertheim G.K. & Cohen R.L. & Rosenzweig A.

& Guggenheim H.J. (1972)

Electron Spectroscopy, ed. by Shirley D.A.

North-Holland

Wertheim G.K. & Guggenheim H.J. & Huener S. (1973)

Phys. Rev. Lett., 30 , 1050

White E.W. & Gibbs G.V. (1967)

Amer. Mineral., 52 , 985

White E.W. & Johnson Jr. G.G. (1978)

X-ray and Absorption Wavelengths and Two-theta Tables  
American Society for Testing and Materials

Williams J.H. (1933)

Phys. Rev., 44 , 146

Willson P.D. & Edwards T.H. (1976)

Appl. Spectrosc. Rev., 12 (1), 1

Woo Y.H. (1926)

Phys. Rev., 28 , 427